RUPRECHT-KARLS-UNIVERSITÄT HEIDELBERG

Stefan Lausberg

Development of a Metallic Magnetic Calorimeter for High Resolution β-Spectroscopy

Diploma Thesis

HD-KIP 08-17

KIRCHHOFF-INSTITUT FÜR PHYSIK

Faculty of Physics and Astronomy
University of Heidelberg

Diploma Thesis
in Physics

submitted by
Stefan Lausberg
born in Schwelm

2008

Development of a Metallic Magnetic Calorimeter for High Resolution β-Spectroscopy

This diploma thesis has been carried out by Stefan Lausberg
at the Kirchhoff Institute for Physics
under the supervision of
Professor Christian Enss

This thesis describes the development of a metallic magnetic microcalorimeter (MMC) for the high-resolution β-spectroscopy. The performance of the developed MMC is tested by the β-emitter ^{63}Ni which has an endpoint energy of 67 keV. The detector consists of a paramagnetic temperature sensor that is in tight thermal contact to an absorber and is additionally positioned in a weak magnetic field. A temperature change due to an incident particle to the absorber results in a change of magnetization of the sensor. This can be detected with high precision as a change of magnetic flux by a low noise high bandwidth dc-SQUID magnetometer. In order to achieve a high quantum efficiency a 4π-absorber, that fully encases the β-source, is used. The absorber as well as the sensor and the meander shaped pick-up coil are fabricated by means of microstructuring. For this purpose a process for the electroplating of gold absorbers using a sulfite-based electrolyte was developed within this work.

The performance of the detector is discussed by temperature dependend magnetization and heat capacity measurements as well as an analysis of the signal shape and noise measurements. A measured β-spectrum of ^{63}Ni with an energy resolution of $\Delta E_{\mathrm{FWHM}} = 1.2\,\mathrm{keV}$ is shown and compared to theoretical data.

Entwicklung eines metallischen, magnetischen Kalorimeters für die hochauflösende β-Spektroskopie

Die vorliegende Diplomarbeit beschreibt die Entwicklung eines metallischen, magnetischen Mikrokalorimeters (MMC) für die hochauflösende β-Spektroskopie. Das entwickelte Mikrokalorimeter wird mit dem β-Strahler ^{63}Ni mit einer Endpunktsenergie von 67 keV getestet. Der Detektor besteht aus einem sich in einem schwachen Magnetfeld befindenden paramagnetischen Temperatursensor, der in gutem thermischen Kontakt zu einem Absorber ist. Eine durch ein absorbiertes Teilchen hervorgerufene Temperaturänderung äußert sich in einer Magnetisierungsänderung des Sensors. Diese kann durch ein rauscharmes dc-SQUID-Magnetometer mit einer hohen Bandbreite als eine magnetische Flussänderung mit hoher Genauigkeit gemessen werden. Um eine hohe Quanteneffizienz zu erreichen, wurde ein 4π-Absorber benutzt, der den β-Strahler vollständig umschließt. Der Sensor, der Absorber und die mänderförmige Aufnahmespule werden durch Mikrostrukturierung hergestellt. Zu diesem Zweck wurde ein Prozess für das Galvanisieren der Goldabsorber mit einem sulfitischen Goldelektrolyten entwickelt.

Die Eigenschaften des Detektors werden mit Hilfe von Magnetisierungsmessungen und Messungen der Wärmekapazität, sowie einer Analyse des Detektorsignals und Rauschmessungen diskutiert. Ein gemessenes β-Spektrum von ^{63}Ni mit einer Energieauflösung von $\Delta E_{\mathrm{FWHM}} = 1{,}2\,\mathrm{keV}$ wird gezeigt und mit theoretischen Daten verglichen.

Contents

1 Introduction **1**

2 Theoretical Background **3**

2.1 β-Decay . . . 3

2.1.1 Introduction . . . 3

2.1.2 Shape of the β-Spectrum . . . 4

2.1.3 β-Decay of ^{63}Ni . . . 7

2.2 Detection Principle of Metallic Magnetic Calorimeters . . . 8

2.3 Sensor material . . . 9

2.3.1 General Properties of Au:Er . . . 9

2.3.2 Magnetization and Heat Capacity of Au:Er . . . 10

2.3.3 Detector Signal . . . 13

2.3.4 The Nuclear Magnetic Moment of ^{167}Er . . . 14

2.4 Energy Resolution of Magnetic Calorimeters . . . 15

2.4.1 Thermodynamical Fluctuations . . . 16

2.4.2 Magnetic Johnson Noise . . . 18

2.5 Detection Geometry . . . 19

2.5.1 Meander Shaped Pick-Up Coil . . . 20

2.5.2 Magnetic Field Distribution . . . 21

2.5.3 Calculation of the Signal Size . . . 22

2.5.4 Flux Change inside the SQUID-Magnetometer . . . 23

2.5.5 Optimization of the Detection Geometry . . . 24

3 Experimental Methods and Detector Fabrication **27**

3.1 Experimental Conditions . . . 27

3.2 dc-SQUID Magnetometers . . . 27

3.2.1 General Features of dc-SQUIDs . . . 28

3.2.2 Single-Stage SQUID Readout . . . 29

3.2.3 Two-Stage SQUID Readout . . . 30
3.3 Detector Chip . . . 33
3.3.1 Injection of the Persistent Current . . . 33
3.3.2 Description of the Detector Chip . . . 35
3.4 Microfabrication of Metallic Magnetic Microcalorimeters . . . 37
3.5 Experimental Setup . . . 39
3.5.1 Detector Setup . . . 39
3.5.2 Data Acquisition and Analysis . . . 40
3.5.3 Internal Source and Calibration Source . . . 41

4 Progress of Metallic Magnetic Microcalorimeters 43
4.1 Properties of Sputtered Niobium Films . . . 43
4.2 Persistent Current Switch . . . 44
4.3 Electroplating of Gold Absorbers . . . 46
4.3.1 Motivation . . . 47
4.3.2 Electroplating of Gold . . . 47
4.3.3 Properties of Electroplated Gold . . . 48
4.3.4 Absorber Deposition . . . 49
4.3.5 Source Deposition . . . 51

5 Experimental Results 53
5.1 Quantum Efficiency of the Detector . . . 53
5.2 Magnetization of the Sensor . . . 54
5.3 Analysis of the Detector Signal . . . 56
5.3.1 Signal Shape Analysis . . . 56
5.3.2 Signal Height Analysis . . . 60
5.4 Measured β-Spectrum of ^{63}Ni . . . 61
5.4.1 Comparison with Theoretical Calculations . . . 61
5.4.2 Kurie Plot and Endpoint Energy . . . 63
5.5 Noise Analysis . . . 63
5.5.1 Detector Noise at 4.2 K . . . 64
5.5.2 Detector Noise at Low Temperatures . . . 66

6 Summary and Outlook **69**

Bibliography **71**

Acknowledgments **77**

1. Introduction

Since the discovery that β-radiation consists of electrons that show a continuous energy distribution, almost hundred years have passed by. Soon the identification as a nuclear decay, that changes the atomic number of the decaying nucleus by one, was found, but the explanation for the non-discrete energy spectrum of the supposed two-body decay could not be given for a long time. In order to conserve energy, Pauli postulated a third particle, the neutrino, which should carry the missing energy of the nuclear β-decay. This particle was experimentally observed for the first time by Reines and Cowan [REI56]. Fermi theoretically described the shape of the spectrum, already including the important influence of the coulomb potential of the nucleus. Soon one noticed that at low energies even more influences like screening effects become important. In addition to these basic problems the calculation becomes much more difficult if we consider β-transitions with electrons and neutrinos that carry orbital angular momentum. These so-called forbidden transitions exhibit altered spectra which are theoretically not fully understood so far and have to be verified experimentally.
The theoretical description and the experimental measurement of β-spectra has various applications. Besides the physical ambition to measure the neutrino mass, the nuclear medicine community as well as nuclear safety departments require exact data of β-isotopes. Nuclear safety departments have to distinguish various sources by evaluating recorded spectra. Therefore the individual spectra have to be well known. In developed countries the rate of nuclear medicine diagnosis is 1.9 % of the population per year, and the rate of therapy with radioisotopes is about one tenth of this amount. In Europe alone there are about 10 million nuclear medicine procedures per year [WNA08]. β-sources provide the majority of the applied radioisotopes and are used to examine diseased organs or tumors as well as to locally destroy malfunctioning cells. Since radio-pharmaceuticals are injected into the body, the accuracy of the deposited dose is of great importance. The calculation of the dose is based on the energy distribution of β-spectra. Therefore its accuracy relies on the validity of the existing experimental data. However, nuclear data tables often contain inconsistent values. Hence experimental methods have to be improved in order to obtain more reliable information.
Conventional techniques to determine the activity of β-emitters are liquid scintillator detectors and ionization chambers. Both methods exhibit an energy dependent quantum efficiency. So one needs the knowledge of the shape factor of the measured isotopes to determine the real spectrum.

Metallic magnetic microcalorimeters (MMC) provide an interesting alternative to measure β-spectra. This rather new detector type is a low temperature detector which is based on a paramagnetic sensor that is situated in a weak magnetic field and is thermally well connected to an absorber for the particles to be detected. A temperature change due to an incident particle changes the magnetization of the

sensor which is read out as a change of magnetic flux by a SQUID magnetometer. MMCs can be designed to fulfill the requirements of β-spectroscopy, i.e. a high linearity over a large energy range, an energy independent quantum efficiency and a good energy resolution [ROT07]. They also have a low energy threshold compared to other spectrometers. Therefore metallic magnetic calorimeters are well-suited to reduce uncertainties on activity standards determined by liquid scintillation and ionization chambers.

Within this work a MMC was developed for high resolution spectroscopy of β-emitters with an endpoint energy up to 1 MeV with a high quantum efficiency. The performance of the developed detector was tested with the isotope ^{63}Ni which has an endpoint energy of 67 keV. ^{63}Ni exhibits a 100 % allowed β-decay with a theoretically well understood spectral shape. Therefore it is a very good test source for new β-spectroscopy methods. In order to obtain a high quantum efficiency, a 4π-absorber with a high stopping power was used. To ensure a good thermal contact between sensor and absorber, processes for both electroplating of gold absorbers by using a sulfite-based electrolyte and enclosing of a β-source were developed.

This thesis is divided into four parts. Chapter 2 discusses the β^--decay, its theoretical shape as well as the particularities of the decay of ^{63}Ni. The detection principle of metallic magnetic calorimeters is described and the thermodynamical properties of the used sensor material Au:Er are pointed out. The energy resolution of MMCs, the detection geometry of the developed detector and its optimization are discussed.

Chapter 3 gives an overview of the experimental methods, the design and the fabrication processes of the detector. The cryostat that is used to generate the necessary low temperatures is briefly descibed. The readout scheme of the detector using a two-stage SQUID magnetometer is discussed in detail. Finally the experimetal setup and the data acquisition are described.

Chapter 4 points out the progress that was done in the development of magnetic microcalorimeters and discusses the electroplating of gold absorbers that was developed within this thesis.

In chapter 5 the experimental results obtained by the developed detector are discussed. A Monte Carlo simulation is used to determine the quantum efficiency of the detector. The measured magnetization and heat capacity of the Au:Er sensor are compared to theoretical data. Furthermore the shape of the signal is discussed in detail. In order to demonstrate the performance of the detector, a measured β-spectrum of ^{63}Ni is shown and compared to a theoretically calculated spectrum. We conclude with an analysis of the detector noise.

2. Theoretical Background

In this chapter the theoretical background for the performed experiment is discussed, starting with the description of the nuclear β-decay. The detection principle of metallic magnetic calorimeters is explained as well as the properties of the used sensor material and the energy resolution achievable with these detectors.

2.1 β-Decay

In the beginning of the twentieth century the phenomenon of β-radiation was found to be a nuclear process in which electrons are emitted and the atomic number is increased by one unit. In 1914 Chadwick was the first one to show that β-radiation has a continuous energy spectrum. This fact generated discussion in the physicists community since the β-decay was considered to be a two body decay and therefore a discrete spectrum was expected. In order to conserve energy, Pauli in 1931 postulated the existance of a third particle which is very difficult to detect. The name Pauli gave to this particle was neutrino since it carries no charge and has a very small mass. In 1956 this hypothesis was confirmed by an experiment which for the first time detected these weakly interacting particles.

2.1.1 Introduction

Under the name of β-decay different processes are summarized, but here we focus on the β^--decay. Here a neutron inside the nucleus decays into a proton. Together with the electron, an antineutrino is emitted. For lepton number and flavor conservation only antineutrinos of electronic flavor occur. There are cases in which nuclei decay into an excited state of the daughter nucleus. Then a subsequent γ-ray is emitted. The β-decay of a nucleus is schematically shown in figure 2.1.

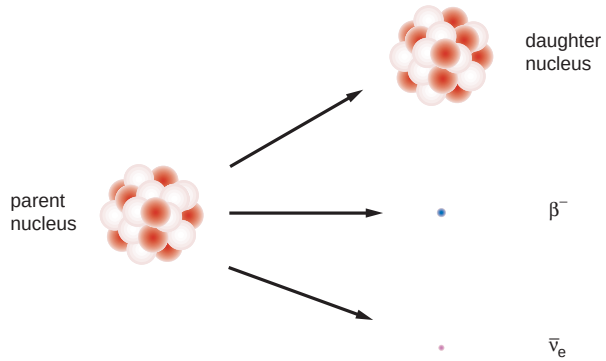

Figure 2.1 The nuclear β^--decay. Besides a daughter nucleus, an electron and an antineutrino are emitted.

The decay of a parent nucleus P to a daughter nucleus D can be written as

$$ {}^{A}_{Z}P \rightarrow {}^{A}_{Z+1}D + e^- + \overline{\nu_e}, \tag{2.1} $$

where Z is the atomic number of the parent nucleus and A its atomic mass.

The prerequisite for a β^--decay is that the mass of the parent atom exceeds the mass of the daughter atom,

$$m(A, Z) > m(A, Z + 1). \tag{2.2}$$

The mass defect provides the kinetic energy of the decaying particles. The plot of the masses of different isotopes with the same atomic mass against the atomic number has a parabolic shape that can be understood from Weizsäcker's formula for atomic masses [POV06]. In figure 2.2 the mass parabola for isotopes with the mass number $A = 63$ is shown. The arrow displays the β^--decay of ^{63}Ni to ^{63}Cu, which was investigated in this thesis.

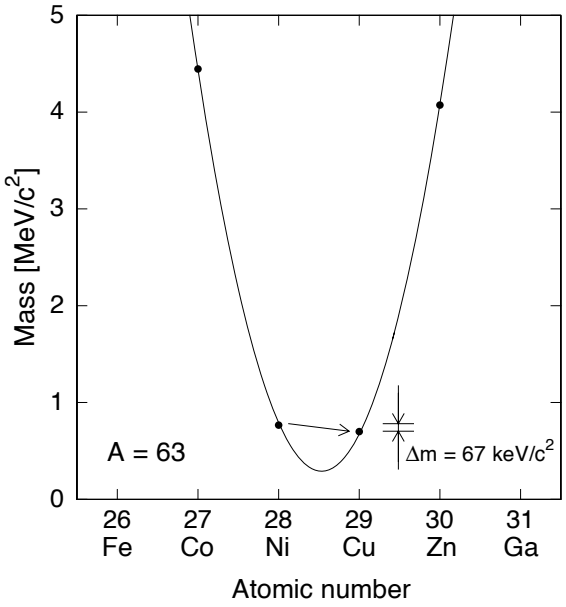

Figure 2.2 Mass parabola for isobar isotopes with a mass number of $A = 63$. The mass difference between ^{63}Ni and the stable isotope ^{63}Cu is barely visible, but equals to an energy of 67 keV. Mass data are taken from [LBN02]. An arbitrary offset was substracted from the mass data.

2.1.2 Shape of the β-Spectrum

As mentioned above the β-decay is a three-body-decay with a continuous spectrum. The calculation of the spectral shape was first done by Fermi. A detailed derivation can be found in [KRA87] or [MAY84].

Fermi's Golden Rule describes the transition rate between two quasi-stationary states:

$$\lambda = \frac{2\pi}{\hbar} |V_{\mathrm{fi}}|^2 \rho(E_{\mathrm{f}}), \tag{2.3}$$

where V_{fi} is the matrix element of the pertubation V that causes the transition from the initital state $|i\rangle$ to the final state $|f\rangle$. The factor $\rho(E_{\mathrm{f}})$ is the density of the final states with the energy E_{f} and $\hbar = h/2\pi = 6.626 \times 10^{-34}$ Js is Planck's constant.

The matrix element contains the wave functions of the parent and daughter nucleus as well as the wave functions of electron and neutrino. The wave function of a free electron is given by

$$\psi_{\mathrm{e}}(\boldsymbol{r}) = \psi_0 e^{i\boldsymbol{p}_{\mathrm{e}}\cdot\boldsymbol{r}/\hbar} = \psi_0 \left(1 + \frac{i\boldsymbol{p}_{\mathrm{e}}\cdot\boldsymbol{r}}{\hbar} + ...\right), \tag{2.4}$$

where $\boldsymbol{p}_{\mathrm{e}}$ denotes the momentum of the electron. The wave function of the neutrino can be written analogously. Within the so-called *allowed* approximation one keeps only the first term of equation (2.4) and therefore the spectral shape is exclusively determined by the density of final states.
The partial decay rate $\mathrm{d}\lambda$ for final state electrons and neutrinos within a momentum range from p_{e} to $p_{\mathrm{e}} + \mathrm{d}p_{\mathrm{e}}$ and from p_ν to $p_\nu + \mathrm{d}p_\nu$ is calculated to

$$\mathrm{d}\lambda = \frac{2\pi}{\hbar} g^2 \left|M_{\mathrm{fi}}\right|^2 (4\pi)^2 \frac{p_{\mathrm{e}}^2\,\mathrm{d}p_{\mathrm{e}}\,p_\nu^2}{h^6}\frac{\mathrm{d}p_\nu}{\mathrm{d}E_{\mathrm{f}}}, \tag{2.5}$$

where M_{fi} is the nuclear matrix element. The constant g determines the strength of the interaction. Within the *allowed* approximation, the β-spectrum is finally calculated to [KRA87]

$$N'(E) = \frac{C}{c^5}\sqrt{E^2 + 2Em_{\mathrm{e}}c^2}\,(E_0 - E)^2(E + m_{\mathrm{e}}c^2). \tag{2.6}$$

Here E_0 denotes the endpoint energy of the decay and E is the kinetic energy of the emitted electron. The factor C is a constant including the nuclear matrix element for allowed transitions and c is the speed of light. The spectrum $N'(E)$ is depicted in figure 2.3 (left).

In order to achieve a better agreement with experimentally determined spectra, one has to include the Coulomb interaction between the emitted electron and the daughter atom. The electronic wave function is influenced by the Coulomb potential and a quantum mechanical calculation introduces a correction factor, the so-called Fermi function

$$F(Z', E) = \frac{\left|\psi(0)_{\mathrm{Coulomb}}\right|^2}{\left|\psi(0)_{\text{free electron}}\right|^2}, \tag{2.7}$$

that modifies the shape of the β-spectrum. Z' denotes the atomic number of the daughter nucleus. The Fermi function can be calculated numerically and was tabled in [BEH69]. Figure 2.3 (left) shows the Fermi function as calculated by H. Rotzinger [ROT08]. The used numerical algorithm was discussed in [ROT07] and is based on an algorithm described in [BÜH63]. It includes the screening effects of the electron shell. As no screening data for the electron shells of copper and nickel were available, the screening of zinc [BYA56] was used.

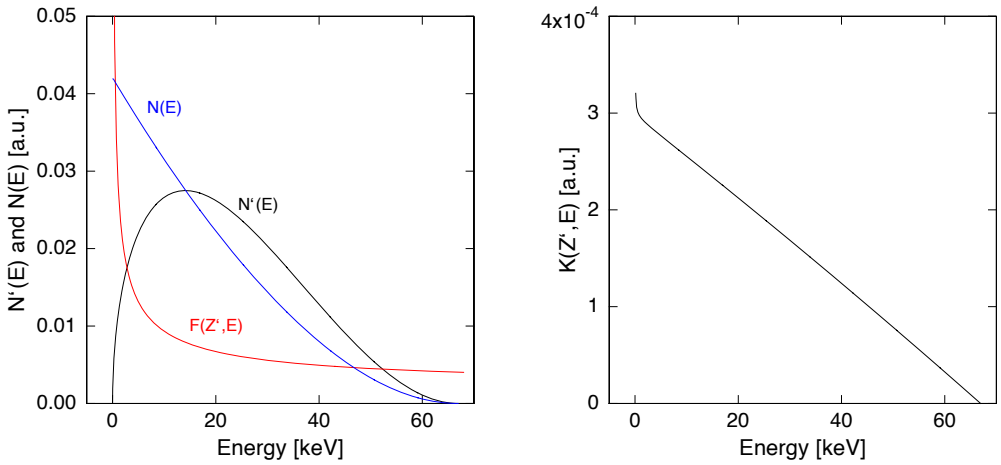

Figure 2.3 **Left:** $N'(E)$ is the uncorrected β-spectrum, as described by equation (2.6). $F(Z', E)$ denotes the calculated Fermi function scaled down by a factor of 1000. $N(E)$, as the product of both curves, is the Coulomb-corrected β-spectrum. The curves are determined by the endpoint energy of ^{63}Ni and the atomic number of the daughter nucleus. **Right:** Kurie plot of the calculated β-spectrum $N(E)$ of ^{63}Ni.

The general shape of the Fermi function can be understood by looking at the non-relativistic approximation which is given by the equation from Mott and Massey [VEN85]

$$F(Z', E) = \frac{2\pi\eta(Z', E)}{1 - e^{-2\pi\eta(Z', E)}}, \tag{2.8}$$

with $\eta(Z', E) = Z'\alpha/2E$ and $\alpha = 1/137$ being the fine structure constant. In the case of a large endpoint energy and high electron energies this curve deviates strongly from the correct relativistic Fermi function. Including the Fermi function results in an increase of intensity at low energies. This increase is particularly high for ^{63}Ni as it has a low endpoint energy and a relatively high atomic number.

If we include the Fermi function into the β-spectrum we obtain the Coulomb corrected spectrum $N(E)$ that is depicted in figure 2.3 (left) and which fits better to experimental data [NEA40]. One can understand the shift to lower energies by considering a semi-classical model in which the electron is attracted by the positively charged daughter nucleus.
The so obtained spectrum can also be expressed by the Kurie plot [KUR36]

$$K(Z', E) = C' \sqrt{\frac{N(E)}{\sqrt{E^2 + 2Em_e c^2}(E + m_e c^2) F(Z', E)}} \propto (E_0 - E), \tag{2.9}$$

where C' is another constant. If one plots $K(Z', E)$ against E one obtains a linear curve like in figure 2.3 (right) as long as the assumption holds, that M_{fi} does not

influence the shape of the spectrum. In many cases of nuclear β-decay this condition is fulfilled.

However, there are still a lot of β-decays in which M_{fi} is not just a constant. This is the case for the so-called forbidden decays. The Kurie plot for forbidden decays is not a straight line, but has a certain curvature which makes it to an appropriate tool to find out the nature of a decay.

Table 2.1 lists allowed and forbidden decays. The change of the orbital angular momentum of the nucleus is denoted by l, which determines the degree of forbidden decays. The value of $ft_{1/2}$ is called the ft-value or comparitive half-life and is given by [KRA87]

$$ft_{1/2} = 0.693 \frac{2\pi^2\hbar^7}{g^2 m_{\mathrm{e}}^5 c^4 \left|M_{\mathrm{fi}}\right|^2}. \tag{2.10}$$

The factor $f = f(Z', E_0)$ denotes the integrated Fermi function that can be found in tabular form [FEE50]. The logarithm of $ft_{1/2}$ is a rough measure for the nature of a decay.

Kind of decay	l	$\log(ft_{1/2})$
allowed	0	3.5-7.5
first forbidden	1	6.0-9.0
second forbidden	2	10-13

Table 2.1 Logarithm of comparitive half-lives for allowed and forbidden decays. By using the value of $\log(ft_{1/2})$ one can roughly classify the nature of a decay.

For the sake of completeness it has to be noted that not all β-decays have a definite order of forbiddeness. For example, there are β-isotopes which have a mixture of the allowed and the first forbidden decay. Some isotopes do not only emit one kind of β-particle, but both electrons and positrons.

2.1.3 β-Decay of ^{63}Ni

In this thesis the β-decay of ^{63}Ni was investigated. ^{63}Ni decays into the ground state of ^{63}Cu and it is a 100 % allowed β-decay. In [HET87] its endpoint energy was determined by using a $\pi\sqrt{2}$ spectrometer with a multistrip source and a detector array of 22 proportional counters. A fit to the data from 50 keV to the endpoint of the β-spectrum resulted in an endpoint energy of (66.946 ± 0.020) keV.

The half-life of ^{63}Ni is (101.1 ± 1.4) years, as was determined in [COL96]. For this, three independant measurements, such as microcalorimetry and liquid scintillation, that were conducted over 27 years, were evaluated. As ^{63}Ni has a long half-life and a low endpoint energy, it is an appropriate mean for the low energy calibration. For example, it was used for the international comparison of liquid scintillation spectroscopy (LSC) techniques [CAS98].

In [GAI96] a cryogenic detector that consists of series of superconducting tunnel junc-

tions (SASTJs) which were operated at 50 mK was used to measure the β-spectrum of ^{63}Ni. Here two semi-conductor completely enclose the source.

A Kurie plot of the ^{63}Ni-spectrum measured with a cryogenic microcalorimeter can be found in [LOW93]. The core of this calorimeter consists of a superconducting tin absorber encapsulating the source. A neutron-transmutation-doped germanium thermistor was used to measure the thermal transient caused by the β-particles.

^{63}Ni as a neutron activated product of stable nickel can, for example, be found in nuclear power plants. In [STR03] ^{63}Ni was detected that was produced from ^{63}Cu by the reaction with fast neutrons during the atomic bomb explosion in Hiroshima. The material samples consisted of rain gutters, copper roofs and lightning conductors.

2.2 Detection Principle of Metallic Magnetic Calorimeters

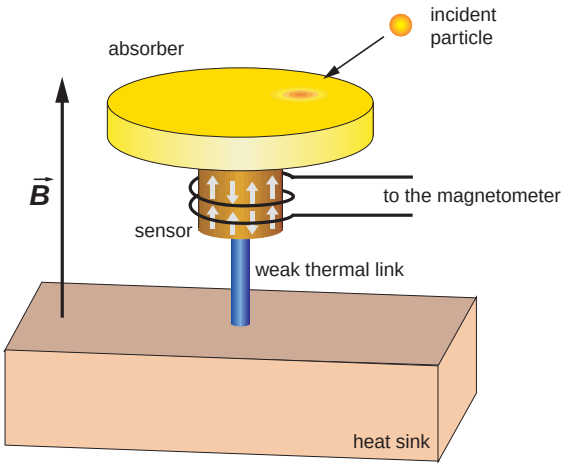

Figure 2.4 Detection principle of a metallic magnetic calorimeter

A metallic magnetic calorimeter (MMC) consists of an absorber that is in good thermal contact with a paramagnetic sensor. The sensor usually consists of a metallic host doped with paramagnetic ions. The sensor is thermally weak connected to a thermal bath that has a temperature in the millikelvin regime. A weak magnetic field partially aligns the spins inside the sensor. The schematic setup of a MMC is depicted in figure 2.4. If an incident particle hits the absorber, it deposits its energy δE leading to an increase of temperature of the absorber and the sensor. The temperature change δT of the detector is proportional to the energy of the incident particle:

$$\delta T = \frac{\delta E}{C_{\mathrm{tot}}}, \tag{2.11}$$

where C_{tot} denotes the total heat capacity of sensor and absorber.
The magnetization change δM of the paramagnetic sensor due to the energy input

is given by

$$\delta M = \frac{\partial M}{\partial T}\delta T = \frac{\partial M}{\partial T}\frac{\delta E}{C_{\mathrm{tot}}}. \tag{2.12}$$

This change of magnetization is read out by low-noise high bandwidth dc-SQUID magnetometers.

The fact that the working temperature of a MMC is in the millikelvin regime is essential. From equation 2.11 one recognizes that a small heat capacity C_{tot} is essential for a MMC in order to allow for a large temperature change which is necessary for a large magnetization change. Equation (2.12) gives the relation of the temperature dependence of the magnetization. For paramagnetic sensor materials this is particularly high at low temperatures as we will see in section 2.3.2. The third important point is the influence of the thermal noise which should be much smaller than the detector signal. This is given in the millikelvin regime where the thermal noise has a rather small value.

2.3 Sensor material

The detector developed and discussed in this work makes use of a dilute alloy of gold and the rare earth metal erbium as paramagnetic sensor material. This material class has been proven to allow for a reasonable compromise between specific heat, magnetization and relaxation times [BAN93], [ENS00].

2.3.1 General Properties of Au:Er

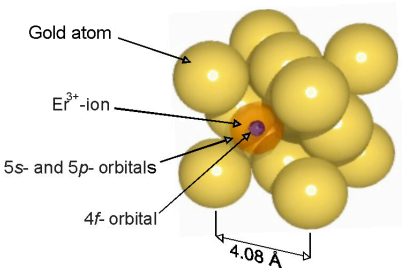

Figure 2.5 Schematic of a fcc gold lattice unit cell containing one erbium ion which replaces a gold atom on a regular lattice site.

Gold is a diamagnetic metal with fcc lattice structure and a cubic lattice constant of 4.08 Å. If small concentrations of erbium are diluted in gold, Er^{3+}-ions replace gold atoms on regular lattice sites, as sketched in figure 2.5. The paramagnetic behaviour of erbium ions arises from the partially filled $4f$ shell. This shell has a radius of only 0.3 Å and is therefore shielded from the crystal field by the $5s$ and $5p$ shell which have a radius of about 1 Å.

For the calculation of the magnetization of Au:Er alloys at temperatures above 100 K the influence of the crystal field can be neglected [WIL69]. The orbital angular momentum L, the spin S and the total angular momentum J can be derived by Hund's rules and one obtains the values $L = 6$, $S = 3/2$, $J = 15/2$. From these values

the corresponding Landé factor is calculated to $g_J = 6/5$. Now one can calculate the magnetic moment by $\boldsymbol{\mu} = -g_J \mu_B \boldsymbol{J}$, where $\mu_B = 9.27 \times 10^{-24}\,\mathrm{J/T}$ denotes Bohr's magneton.
At lower temperatures the crystal field is no longer negligible. It splits the sixteen fold degeneracy of the Er^{3+} ground state into a series of multiplets.

The energy splitting between the ground state doublet (Γ_7 Kramers doublet) and the first excited multiplett (Γ_8 Kramers quartet) was measured by different research groups in different ways [WIL69], [DAV73], [SJÖ75]. Up to now, the propably most precise measurement was done by neutron scattering and resulted in a value of $\Delta E/k_B = (17 \pm 0.5)\,\mathrm{K}$ [HAH92]. At temperatures below 1 K only the ground state doublet is thermally occupied. Therefore at low temperatures the system can be considered as a two level system that can be described by an effective spin $\widetilde{S} = 1/2$ and an effective isotrope Landé factor of $\widetilde{g} = 34/5$.

2.3.2 Magnetization and Heat Capacity of Au:Er

The performance of a metallic magnetic calorimeter strongly depends on the heat capacity and the magnetization of the Au:Er sensor. As the calorimeter is operated at temperatures below 100 mK we consider the Au:Er to be an effective two level system, as discussed in section 2.3.1.
The heat capacity of a system of N non-interacting magnetic moments, which can occupy two states with energy splitting $E = \widetilde{g}\mu_B B$ is given by

$$C_Z = N k_B \left(\frac{E}{k_B T}\right)^2 \frac{e^{E/k_B T}}{(e^{E/k_B T} + 1)^2} \tag{2.13}$$

The heat capacity C_Z is depicted in figure 2.6 (left). It shows a maximum, the so-called Schottky anomaly, at a temperature where the thermal energy is about half of the energy splitting $k_B T = 0.42\,E$.
The magnetization of Au:Er can as well be calculated by assuming non-interacting magnetic moments with $\widetilde{S} = 1/2$ and we find

$$M = \frac{1}{2}\frac{N}{V}\widetilde{g}\mu_B \tanh(h) \tag{2.14}$$

with the argument

$$h = \frac{\widetilde{g}\mu_B B}{2 k_B T}. \tag{2.15}$$

For high temperatures, i. e. $h \ll 1$, the magnetization varies like $1/T$ as expected from the Curie law (see figure 2.6). For low temperatures, i. e. $h \gg 1$, the magnetization saturates which results from the fact that for $T \to 0$ all magnetic spins are aligned with the magnetic field.

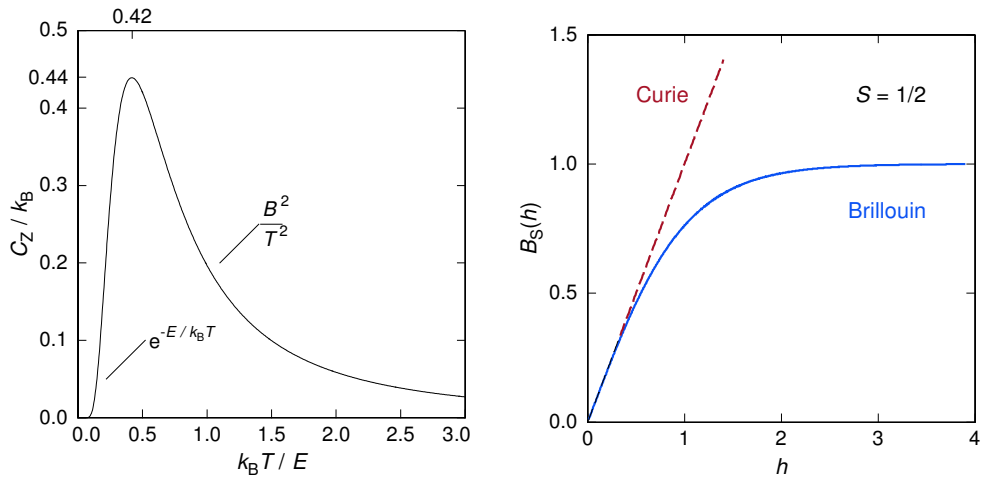

Figure 2.6 **Left:** Specific heat of a two level system with energy splitting $\Delta E = \widetilde{g}\mu_B B$. The maximum is denoted as Schottky anomaly which appears at a temperature $T = 0.42\,E/k_B$. **Right:** Brillouin function $B_{1/2}(h) = \tanh(h)$ for spin 1/2 magnetic moments versus $h = E/2k_BT$. For high temperatures, i. e. for a small h, the Brillouin function behaves like the Curie law.

Interacting Spins

The magnetization and heat capacity of Au:Er show qualitatively the behavior of a system of non-interacting magnetic moments. However, in order to obtain quantitative agreement with the experimental data, interaction mechanisms need to be included in the description. Possible interaction mechanisms are the dipole-dipole interaction and the so-called RKKY[1]-interaction.
The magnetic dipole-dipole interaction hamiltonian of two Er^{3+} ions with the effective spins $\tilde{\boldsymbol{S}}_i$ and $\tilde{\boldsymbol{S}}_j$ can be calculated to

$$H_{ij}^{\text{dipole}} = \underbrace{\frac{\mu_0}{4\pi}(g\mu_B)^2(2k_F)^3}_{\Gamma_{\text{dipole}}=0.0343\,\text{eV}}(\tilde{\boldsymbol{S}}_i \cdot \tilde{\boldsymbol{S}}_j)\frac{1-3(\tilde{\boldsymbol{S}}_i \cdot \tilde{\boldsymbol{r}}_{ij})(\tilde{\boldsymbol{S}}_j \cdot \tilde{\boldsymbol{r}}_{ij})/\tilde{\boldsymbol{S}}_i \cdot \tilde{\boldsymbol{S}}_j}{(2k_F r_{ij})^3} \tag{2.16}$$

Here k_F denotes the Fermi wave vector. It is artificially introduced in this equation for a later comparison with the RKKY-interaction.
The RKKY interaction is a indirect exchange interaction between localized magnetic moments mediated by the conduction band electrons. The interaction hamiltonian of two Er^{3+}-ions that are located at the positions $\boldsymbol{r}_i$ and $\boldsymbol{r}_j$ can be written as [FLE03]

$$H_{ij}^{\text{RKKY}} = \underbrace{\mathcal{J}_{\text{sf}}^2 \frac{g^2(g_J-1)^2}{g_J^2}\frac{4V_p^2 m_e^* k_F^4}{\hbar^2(2\pi)^3}}_{\Gamma_{\text{RKKY}}}(\tilde{\boldsymbol{S}}_i \cdot \tilde{\boldsymbol{S}}_j)F(2k_F r_{ij}), \tag{2.17}$$

[1]Named after Ruderman, Kittel, Kasuya and Yosida, [RUD54], [KAS56], [YOS57].

where F denotes the Kittel function

$$F(\rho) = \frac{\cos(\rho) - \frac{1}{\rho}\sin(\rho)}{\rho^3}. \tag{2.18}$$

The factor V_p denotes the volume of the primitive unit cell, m_e^* the effective mass of the conduction band electrons and $\mathcal{J}_\mathrm{sf}$ is a measure for the exchange energy between the localized $4f$ electrons and the s-like conduction electrons.

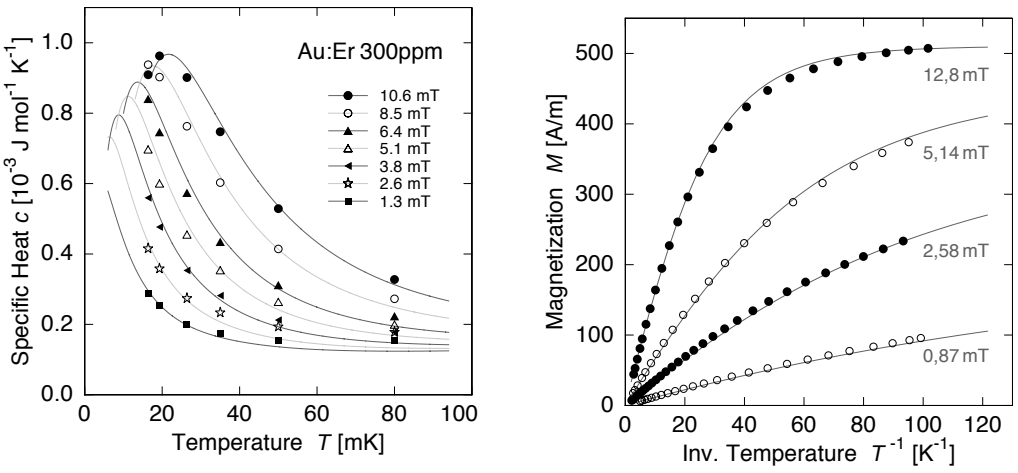

Figure 2.7 Specific heat and magnetization of bulk Au:Er with 300 ppm of erbium at different magnetic fields. Squares, circles, etc. denote measured values. The solid lines were calculated numerically with an interaction parameter $\alpha = 5$ [FLE03].

Because of the $1/r^3$-dependence in equation (2.16) and equation (2.17), one can compare the strength of the RKKY-interaction with the strength of the dipole-dipole interaction by introducing the dimensionless parameter

$$\alpha \equiv \frac{\Gamma_\mathrm{RKKY}}{\Gamma_\mathrm{Dipole}}. \tag{2.19}$$

Figure 2.7 shows the measured heat capacity and the measured magnetization of a Au:Er-sample with an erbium concentration of 300 ppm as well as the results of numerical calculations of thermodynamical properties, assuming an interaction parameter $\alpha = 5$ [FLE03]. Compared to the case of non-interacting spins the magnetization curves of interacting spins have saturation values that are about 10 % smaller than the ones of non-interacting spins. The specific heat shows the expected Schottky anomaly, but the maximum is roughly twice as broad as the one in the non-interacting case. However, the numerically calculated curves fit the experimental data very well showing that the thermodynamical properties of Au:Er can be calculated with confidence. This is of major importance for the numerical optimization calculations discussed below.

2.3.3 Detector Signal

The deposition of an energy δE into the absorber of a magnetic microcalorimeter results in a change of magnetization δM of the sensor as we saw in equation (2.12). Here we determine the change of the magnetic moment δm of the sensor which is given by

$$\delta m = V \delta M, \tag{2.20}$$

where V is the volume of the sensor. In a system of non-interacting spins the energy input of δE leads to the flipping of δN spins. Each spin flip needs the energy of the Zeeman splitting $E = \widetilde{g}\mu_{\mathrm{B}} B$. Therefore the total change in magnetic moment is calculated by

$$\delta m = \frac{\delta N\, E}{B} = \frac{\delta E}{B}. \tag{2.21}$$

This means that in a system which exclusively consists of non-interacting spins the change of the magnetic moment increases as the magnetic field decreases. At a constant energy input more spins can flip with a decreasing Zeeman splitting.
In reality, the detector does not consist of a single thermodynamical system as implicitily assumed in equation 2.21. The detector consists of multiple systems with different heat capacities. The most important ones are, besides the Zeeman system with heat capacity C_Z, the system of the conduction electrons and the system of the phonons with the heat capacities C_{el} and C_{ph}, respectively. The molar heat capacity c_{ph} of the phonons rises with temperature via $c_{\mathrm{ph}}(T) = \beta T^3$ where $\beta = 4.0 \times 10^{-4}$ J/(mol K^4) [ASH07] for gold. Because of the T^3-dependence the contribution of the phonons is negligible at temperatures below 100 mK. The molar heat capacity c_{el} of the electrons rises with temperature via $c_{\mathrm{el}}(T) = \gamma T$ where $\gamma = 6.9 \times 10^{-4}$ J/(mol K^2) [ASH07] for gold. The additional electronic heat capacity leads to a smaller energy amount

$$\delta E_Z = \frac{C_{\mathrm{Z}}}{C_{\mathrm{Z}} + C_{\mathrm{el}}} \delta E \tag{2.22}$$

which enters the Zeeman system leading to a reduced signal size compared to the one of equation (2.21).

Figure 2.8 shows the calculated change of magnetic moment δm of a Au:Er-sensor with an erbium concentration of 775 ppm upon the absorption of a 5.9 keV photon as a function of the magnetic field. For small magnetic fields δm rises linearily because δE_{Z} rises with $C_{\mathrm{Z}} \propto B^2$ and $\delta m = \delta E_Z / B$. At higher magnetic fields, the heat capacity of the Zeeman system becomes comparable with the heat capacity of the conduction electrons and the detector signal reaches a maximum. In the limit of high magnetic fields the major part of the deposited energy enters the Zeeman system and the magnetic moment decreases with $1/B$ as in equation 2.21.

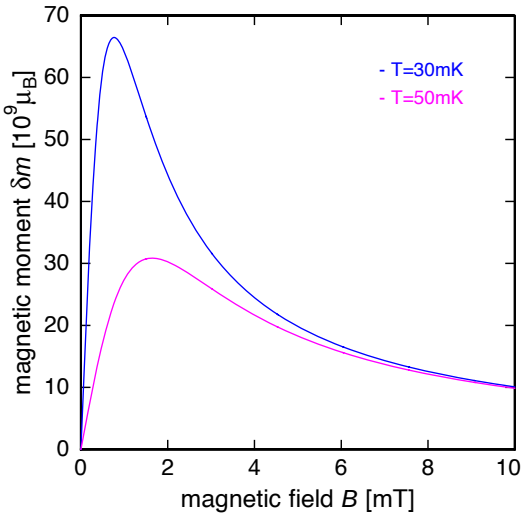

Figure 2.8 Calculated change of magnetic moment δm of a Au:Er-sensor with an erbium concentration of 775 ppm as a function of the magnetic field at the absorption of a 5.9 keV photon. The plot shows curves at two different temperatures.

2.3.4 The Nuclear Magnetic Moment of ^{167}Er

In the above discussion we described the paramagnetic behaviour of Au:Er at low temperatures by effective two-level systems, as the Er^{3+}-ions occupy only the Γ_7 Kramers ground state doublet. This holds as long as erbium has no nuclear magnetic moment.
There are a number of stable isotopes of erbium. Only the isotope ^{167}Er has a nuclear magnetic moment and it contributes by 22.9 % to the natural isotopic mixture of erbium. The nuclear magnetic moment of ^{167}Er has a value of $I = 7/2$ and it interacts with the $4f$-electrons which causes a hyperfine splitting within the Γ_7 Kramers doublet.

This level splitting is shown in figure 2.9 (left) as a function of the magnetic field. The energy splitting between the group with total angular momentum $F = 3$ and the group with $F = 4$ at a zero magnetic field has a value of $\Delta E/k_B = 140\,\mathrm{mK}$. In finite magnetic fields the two groups split into $2F + 1$ energy levels.
The deposition of energy in the system of ^{167}Er-ions results in a redistribution of occupied energy states towards states of higher energies. In small magnetic fields excitations within one of the groups $F = 3$ or $F = 4$ result in a change of magnetization and lead to a signal change in the SQUID magnetometer. But if excitations take place from states of $F = 3$ to states of $F = 4$, the magnetization does not necessarily change and therefore the excitations do not contribute to the detector signal. This comes along with an enhancement of the heat capacity which is depicted in figure 2.9 (right). This plot shows the heat capacity of a Au:Er sample that contains erbium of the natural isotope mixture with a concentration of 480 ppm at different magnetic fields. At low magnetic fields one recognizes two maxima. The maximum at low temperatures is due to excitations within $F = 4$ multiplett of ^{167}Er, which cause magnetization changes. On the other hand the maximum around 50 mK is due to the discussed excitations from $F = 4$ to $F = 3$. At low magnetic fields and tem-

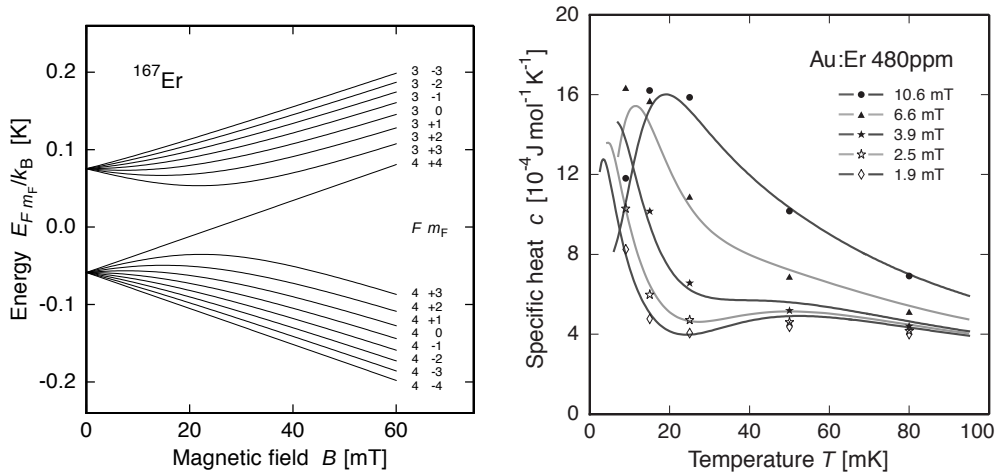

Figure 2.9 **Left:** Level scheme of the hyperfine splitting of the Γ_7 Kramers doublet of ^{167}Er ions inside a gold host. The energy splitting at zero magnetic field has a value of $\Delta E/k_B \cong 140\,\mathrm{mK}$. **Right:** Measured heat capacity of a Au:Er sample that contains an erbium concentration of 480 ppm. The utilized erbium has the natural isotope mixture with a ^{167}Er contribution of 22.9 %. The solid lines represent the calculated specific heat using a mean-field approximation [ENS00].

peratures of about 50 mK this maximum is the dominant contribution to the heat capacity. In this temperature range the influence of the nuclear magnetic moment of ^{167}Er reduces significantly the signal size of a MMC.
In this thesis a sensor with the natural isotope mixture of erbium was used. The influence of the nuclear magnetic moment of ^{167}Er will be taken into account in the analysis of the measured data.

2.4 Energy Resolution of Magnetic Calorimeters

One of the most important parameters that characterize a particle detector is its energy resolution. As we will see in the following section, the energy resolution of magnetic microcalorimeters does not depend on the energy of the incident particle like in the case of ionization chambers or HPGe counters. While external influences like mechanical vibrations or temperature variations can be suppressed by experimental preparations, there are three rather intrinsic limitations to the achievable energy resolution of a MMC:

- Thermodynamical fluctuations of energy between the subsystems of the detector
- Magnetic Johnson noise of metallic detector components
- Magnetic flux noise of the SQUID magnetometer

In this this section the thermodynamical fluctuations of energy and the magnetic Johnson noise will be discussed. We return to the SQUID noise in section 3.2.

2.4.1 Thermodynamical Fluctuations

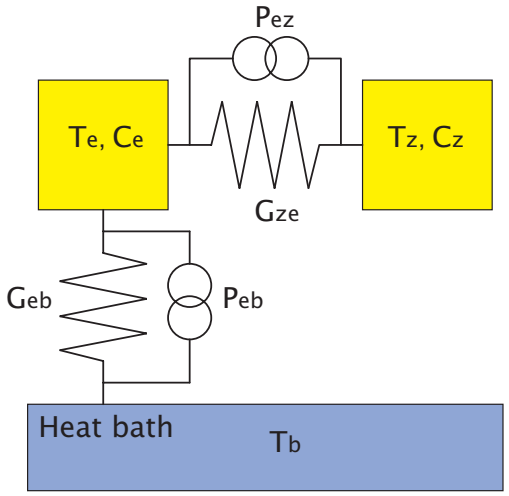

Figure 2.10 A magnetic microcalorimeter as a canonical ensemble with two sub-systems. The Zeeman system is characterized by the heat capacity C_Z and the temperature T_Z. The system of the electrons is characterized by C_e and T_e. Both systems are coneted via a thermal coupling G_{ez}. The electronic system is connected to the heat bath via a thermal link G_{eb}. Energy fluctuations between the systems can be described by the noise sources P_{ez} and P_{eb} as depicted.

The effect of thermodynamical fluctuations of energy within a MMC on its energy resolution can be investigated using models of different complexity. The easiest model treats the MMC as a canonical ensemble consisting of only one subsystem that is weakly coupled to a thermal bath. As discussed in [FLE03] within a model of this kind, the energy resolution is not limited. A more realistic thermodynamical model is depicted in figure 2.10. It describes the detector as a canonical ensemble with two sub-systems. One represents the Zeeman system of the spins in the sensor and the other represents the electronic system of sensor and absorber. The Zeeman system has a heat capacity of C_Z and a temperature T_Z while the electronic system has a heat capacity of C_e and a temperature T_e. Both systems are connected via a thermal conductivity G_{ez} and the electronic system is connected to the heat bath via a thermal conductivity G_{eb}. The energy fluctuations between the systems can be described by the noise power sources P_{ez} and P_{eb} which are connected in parallel to the couplings.

The energy content $E_Z(t)$ of the Zeeman system can be measured very precisely, because it is proportional to the magnetic flux inside the SQUID-magnetometer: $E_Z(t) = m(t)B \propto \Phi(t)$. The heat flow between the sub-systems can be described by two coupled differential equations, which were e.g. solved in [FLE03]. The spectral power density of the energy fluctuations of the Zeeman-system is found to be

$$S_{E_Z}(f) = k_B C_Z T^2 \left(\alpha_0 \frac{4\tau_0}{1+(2\pi\tau_0 f)^2} + \alpha_1 \frac{4\tau_1}{1+(2\pi\tau_1 f)^2} \right) \tag{2.23}$$

where τ_0 and τ_1 denote characteristic time constants of the system. The coefficients α_0 and α_1 are dimensionless, rather cumbersome functions of C_e, C_Z, τ_0 and τ_1. The physical situation in this work ($C_e \approx C_Z$, $\tau_0 \ll \tau_1$) permits the approximations

$\alpha_0 \approx 1-\beta$ and $\alpha_1 \approx \beta$ with β being the relative contribution of the Zeeman system to the total heat capacity of the detector,

$$\beta = \frac{C_\mathrm{Z}}{C_\mathrm{e} + C_\mathrm{Z}}. \tag{2.24}$$

In this model the impact of a particle is described by an instantaneous energy rise inside the electronic system. The electrons transfer their energy to the spins of the Zeeman system until a quasi equilibrium state is reached. Subsequently the electrons and the magnetic moments loose their energy through the thermal conductivity G_eb to the bath and therefore the magnetization of the sensor recovers to the initial value. The energy development inside the Zeeman systems within this modell is described by

$$E_\mathrm{Z}(t) = E_\gamma p(t) = E_\gamma \beta (e^{-t/\tau_1} - e^{-t/\tau_0}). \tag{2.25}$$

The function $p(t)$ is a dimensionless function that describes the so-called responsivity of the detector. It is depicted in figure 2.11 (left).

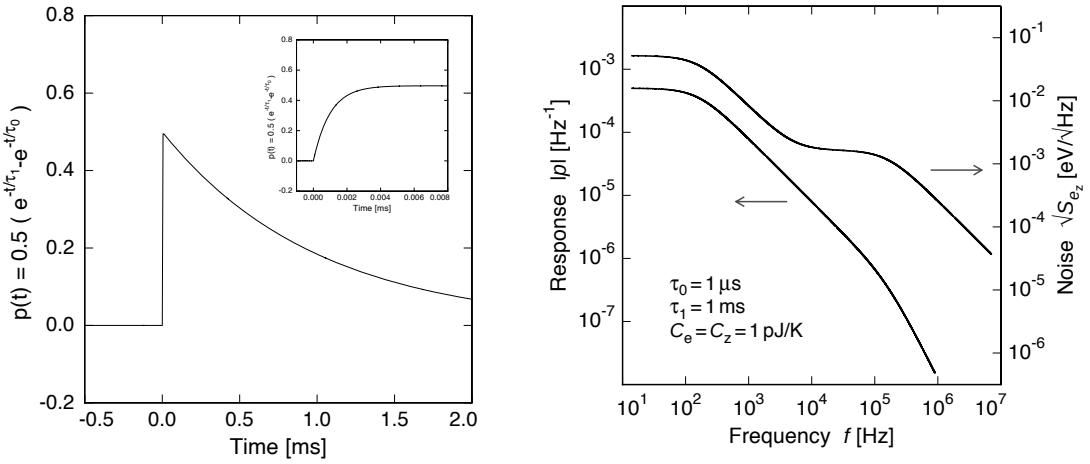

Figure 2.11 **Left:** Resulting pulse shape in the model of a canonical ensemble with two sub-systems. For this plot we choose $\tau_0 = 1\,\mu$s, $\tau_1 = 1\,$ms and $C_\mathrm{e} = C_\mathrm{z} = 1\,$pJ/K. The inset shows an extended view of the pulse rise. **Right:** The power spectrum of the thermodynamical fluctuations of energy of the Zeeman system (right vertical axis) and a pulse in frequency space (left vertical axis)

To compare the signal with the thermodynamical fluctuations it is appropriate to transform the responsivity $p(t)$ to frequency space. The result can be approximated by

$$|\widetilde{p}(f)| \approx \frac{2\tau_1\beta}{\sqrt{1+(2\pi f\tau_0)^2}\sqrt{1+(2\pi f\tau_1)^2}}. \tag{2.26}$$

The power spectrum of the thermodynamical fluctuations of energy of the Zeeman system and the responsivity $\widetilde{p}$ are shown in figure 2.11 (right).
From the equations (2.23) and (2.26) we can derive the signal-to-noise ratio as function of frequency, and assuming pulse height analysis based on a matched filter we can calculate an approximation for the energy resolution [FLE05]:

$$\Delta E_{\mathrm{FWHM}} \approx 2.35\sqrt{4k_{\mathrm{B}}C_{\mathrm{el}}T^2}\left(\frac{1}{\beta(1-\beta)}\frac{\tau_0}{\tau_1}\right)^{1/4} \tag{2.27}$$

From this equation one can see that the energy resolution is limited by the finite rise time τ_0 of the pulse. The rise time at a given temperature T can be identified by the spin-electron relaxation time τ_{K} which is given by the Korringa relation $\tau_{\mathrm{K}} = \kappa/T$ with κ being the Korringa constant. The Korringa constant for the sensor material Au:Er has been determined by ESR measurements at 1 K to be $\kappa = 7 \times 10^{-9}$ Ks [SJÖ75]. At a temperature of $T = 50$ mK this results in a relaxation time $\tau_{\mathrm{K}} = 0.14\,\mu$s.
In order to achieve best energy resolution the decay time should be chosen as long as possible. However, it cannot be arbitrarily long as one needs a finite count rate to obtain sufficient statistics with the calorimeter.
The factor $\beta(1-\beta)$ has a maximum for $C_{\mathrm{Z}} = C_{\mathrm{e}}$, i.e. the energy resolution is the smallest if the heat capacity of the Zeeman system is the same as the heat capacity of the electronic system.

2.4.2 Magnetic Johnson Noise

As the name suggests, metallic magnetic microcalorimeters partially consist of metallic components. Besides the sensor and absorber of the detector various parts of its environment, like the experimental holder, are made of metals to provide, for example, a good thermal conductivity. Thermal motions of electrons inside these components generate fluctuating magnetic fields. This effect is often called magnetic Johnson noise. MMCs are used to measure magnetization changes of the paramagnetic sensor by measuring the magnetic flux change inside a pick-up coil. Because of that, MMCs are susceptible to the magnetic Johnson noise. The contribution of this noise source can be calculated by using the reciprocity theorem as pointed out in [HAR68]. In this approach one assumes an alternating current with frequency ω running through the pick-up coil generating eddy currents in nearby conductors. The resulting losses can be described by a resistance $R(\omega)$ of the pick-up coil. By using the fluctuation dissipation theorem one can calculate the corresponding voltage noise $S_{\mathrm{U}} = 4k_{\mathrm{B}}TR(\omega)$ and subsequently the magnetic flux noise $S_{\Phi} = S_{\mathrm{U}}/\omega^2$ by using Faraday's law of induction.
A rough estimation of the influence of a sensor with volume V and conductivity σ is given by [FLE05]

$$\sqrt{S_{\Phi,\mathrm{J}}} = \mu_0\sqrt{C_{\mathrm{m}}\sigma k_{\mathrm{B}}TV}, \tag{2.28}$$

where $\mu_0 = 4\pi \times 10^{-7}$ Vs/Am is the magnetic permeability of free space and T

denotes the temperature of the sensor. C_m is a constant that can be calculated numerically and that depends on the geometry of the pick-up coil and the sensor. A rough estimation for the geometry used in this work leads to $\sqrt{C_\mathrm{m,sens}} \approx 0.73$. As an example, we calculate the Johnson noise contribution of a sensor as it was used in this thesis. The sensor has a volume of $1000\,\mu\mathrm{m} \times 1000\,\mu\mathrm{m} \times 3\,\mu\mathrm{m}$ and an erbium concentration of 775 ppm. The resistivity of bulk Au:Er alloys at temperatures below 4.2 K is given by the relation $\rho = x\ 6.7 \times 10^{-6}\,\Omega\mathrm{m}$ [ARA66], where x denotes the concentration of erbium. We obtain a Johnson noise of $\sqrt{S_{\Phi,\mathrm{J}}} = 1.72\,\mu\Phi_0/\sqrt{\mathrm{Hz}}$ at a temperature of $T = 50\,\mathrm{mK}$.
The Johnson noise of the absorber can as well be calculated by equation (2.28) by using the values for its volume and electrical conductivity. But this time one has to use a different geometry factor because the height of the absorber and its distance to the pick-up coil must be taken into account. For the absorber used in this work, an estimation of this factor resulted in $\sqrt{C_\mathrm{m,abs}} \approx 0.023$. The electrical conductivity of bulk gold, which was used as absorber material in this thesis, is $\sigma_\mathrm{abs} = 4.55 \times 10^7\,(\Omega\mathrm{m})^{-1}$ [KIT99] at room temperature. The residual resistivity ratio (RRR) of bulk gold deviates over a large range, depending on the number of lattice defects, impurities, etc. Values in the range of RRR= 50...5000 for bulk gold are imaginable.

2.5 Detection Geometry

As pointed out in section 2.2, the temperature change of the sensor/absorber-system of a magnetic calorimeter causes a magnetization change of the sensor leading to a change of magnetic flux in a dc-SQUID magnetometer which is the quantity to be measured. In contrast to the change of magnetic moment δm, which was discussed in section 2.3.3, the magnetic flux change $\delta\Phi$ strongly depends on the detection geometry.

An often used geometry is a cylindrical Au:Er-sensor that is situated inside the circular loop of a SQUID magnetometer[2] and exposed to an external homogenous magnetic field [LIN07]. The change of the magnetic moment δm corresponds to a change of magnetic flux $\delta\Phi_\mathrm{S}$ inside the SQUID loop that can be expressed by

$$\delta\Phi_\mathrm{S} = \mu_0 \frac{G}{r} \delta m, \tag{2.29}$$

where r is the radius of the SQUID loop and $\mu_0 = 4\pi \times 10^{-7}\mathrm{Vs/Am}$ is the magnetic permeability of free space. The so-called geometry factor G represents the coupling of the magnetic moment of the sensor to the SQUID loop. In the case that the diameter of the sensor is much smaller than the diameter of the loop, this factor can be calculated analytically leading to a value of $G = 1/2$ [BAN93].

[2] A description of this device will be given in chapter 3.2.

2.5.1 Meander Shaped Pick-Up Coil

If one moves to larger detection areas, the radius r of the sensor in equation (2.29) rises and so the flux change decreases. In [BUR04] it was shown that MMCs with meander[3] shaped pick-up coils are advantageous in the case of large detection areas.

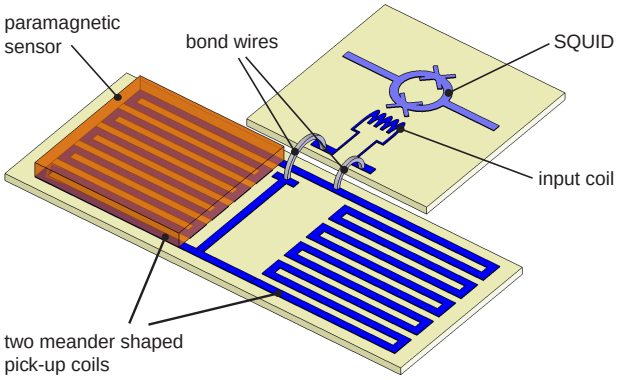

Figure 2.12 Schematic of a magnetic microcalorimeter with a meander shaped pick-up coil. A persistent current inside the meanders creates a magnetic field inside the sensor whose magnetization change results in an additional shielding current inside the meander stripes. A part of this additional current flows through the input coil of the SQUID and transformer-couples the magnetic flux into the SQUID loop.

Figure 2.12 shows the bird's eye view of a magnetic microcalorimeter with a meander shaped pick-up coil similar to the one used within this work. The coil consists of two symmetric meander areas that are connected in parallel to the input coil of a current-sensor SQUID magnetometer. An arrangement of this kind is often called transformer coupling. In contrast to the cylindrical geometry mentioned above, no external magnetic field is needed. By injecting a persistent current into the superconducting circuit formed by the two meanders the meander shaped pick-up coil itself generates the magnetic field. The procedure of injecting a persistent current will be described in chapter 3.3.1. We anticipate that in this setup no large current flows through the input coil of the SQUID as long as no particle is absorbed. Another advantage of this setup is that the detection areas can be moved far away from the power dissipating SQUID. With the usage of only one sensor one can measure the magnetization of the sensor as a function of temperature.

Figure 2.13 depicts a setup which is basically the same as in figure 2.12, but with two sensors and absorbers on top of the meanders. The absorbers are not shown in this figure. The persistent current I_0 generates the magnetic field that is depicted by crosses and dots. If a particle is absorbed in the left absorber the temperature rise generates a magnetization change in the left sensor. An additional shielding current is induced into the pick-up coil and a part of this current enters the input coil of the SQUID and generates a flux signal in the SQUID. This will be discussed quantitatively in section 2.5.4.
In addition, the usage of a second sensor suppresses noise that is generated by varying external magnetic fields or temperature variations of the experimental platform inside

[3]The name meander comes from a river in Greece that reminds of the shape of the utilized pick-up coil.

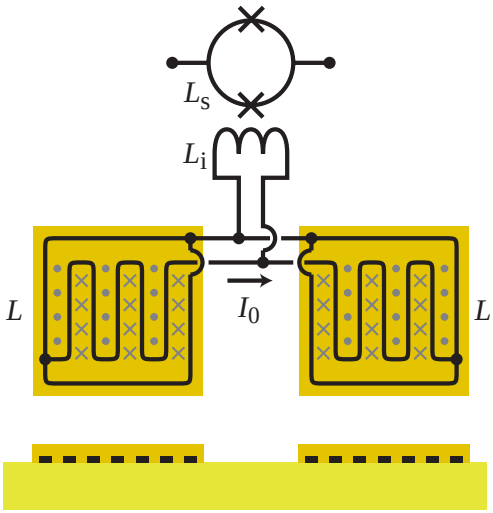

Figure 2.13 Schematic of a meander shaped pick-up coil as a gradiometer. The input coil of the SQUID is connected in parallel to the meanders. Below the sketch a lateral view is depicted.

the cryostat. Temperature variations cause magnetization changes which induce shielding currents into the meanders. If the temperature rises a current is induced in the left meander that has the same amount, but different sign than the current that is induced in the right meander. Therefore, currents due to temperature variations of the heat bath are not seen as a signal. This principle is denoted as gradiometer.

2.5.2 Magnetic Field Distribution

A persistent current that was injected into the meanders produces an inhomogenous magnetic field around the meander shaped pick-up coil. It is not convenient to calculate such a field analytically. Thus we make use of finite element methods by using the computer program FEMM[4] to calculate the field distribution inside the sensor volume above the meander shaped pick-up coil.
For the calculation several simplifications were assumed. The meanders were assumed to be an ideal diamagnet ($\chi_m = 1$) as it is the case for a perfect superconductor. The susceptibility of the paramagnetic sensor was neglected because its magnetic susceptibility is rather small for the utilized erbium concentration and the given temperature regime. The SiO_2-layer, between the meanders and the sensor, with a susceptibility close to zero was taken into account. The length of the meander stripes was supposed to be infinite in order to use translational invariance because FEMM can only solve quasi-two-dimensional problems. In reality the length of a stripe is not infinite, but indeed much larger than its width. The stripes were supposed to carry alternately the currents $+I_0$ and $-I_0$, which flow out of or into the picture plane. The simulation was done for two meander stripes with periodic boundary conditions, neglecting finite size effects at the outermost stripes.

The result of the simulation is shown in figure 2.14 (left) and shows the calculated magnetic field of the meander with a width of $w = 4.25\,\mu$m and a height of 400 nm. The distance between the centers of two neighboring stripes, the so-called pitch, has

[4]Finite Element Method Magnetics (Version 4.0), David Meeker, http://femm.foster-miller.net

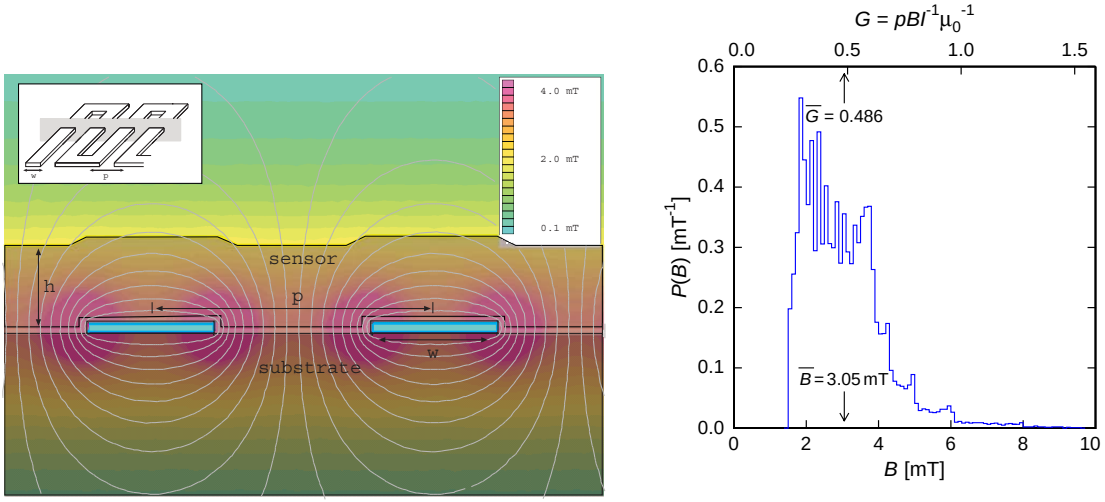

Figure 2.14 **Left:** Magnetic field calculated with FEMM. The width of meander stripes is $w = 4.25\,\mu$m and the height is 400 nm. The pitch is $p = 10\,\mu$m. The persistent current inside the meander is $I_0 = 50\,$mA. The influence of the sensor was neglected. **Right:** Propability distribution $P(B)$ of the magnetic field shown on the left. The sensor in this calculation has a thickness of $3.6\,\mu$m.

a value of $p = 10\,\mu$m. The thickness of the SiO_2-layer and the sensor are 300 nm and $3.6\,\mu$m, respectively. The persistent current inside the meanders is assumed to be $I_0 = 50\,$mA. The average magnetic field in this situation has a value of $\overline{B} = 3.05\,$mT. For other persistent currents it is possible to calculate the magnetic field by scaling. The detector signal can be calculated either by using the magnetic field distribution $B(\boldsymbol{r})$ or the propability distribution $P(B)$ of the magnetic field which is depicted on the right side of figure 2.14. $P(B)dB$ is the propability of occurence of a magnetic field in the interval $[B, B + dB]$ inside the sensor volume.

2.5.3 Calculation of the Signal Size

To calculate the flux change inside the meander upon the deposition of energy in the detector we start from the flux change $d(\delta\Phi_\mathrm{m})$ in the meander, caused by a magnetization change inside an infinitesimal small region d^3r at position $\boldsymbol{r}$ of the sensor:

$$d(\delta\Phi_\mathrm{m}) = \mu_0 \frac{G(\boldsymbol{r}/p)}{p} \delta M(\boldsymbol{r}) d^3r \tag{2.30}$$

This equation is analogous to equation (2.29) for a cylindrical sensor inside a circular SQUID loop with the difference that the geometry factor $G(\boldsymbol{r}/p)$ is not a constant, but a function of position. Here p denotes again the pitch between two neighbouring stripes. In [BUR04] it was shown that the absolute value of the magnetic field $B(\boldsymbol{r})$ when a current I_0 is flowing through the meanders is related to the geometry factor

$G(\boldsymbol{r}/p)$ by

$$B(\boldsymbol{r}) = \mu_0 \frac{G(\boldsymbol{r}/p)}{p} I_0. \tag{2.31}$$

Therefore, for a given magnetic field distribution, we can calculate a distribution of $G(r/p)$.
By combining the equations (2.12), (2.30) and (2.31) and integration over the sensor volume we obtain

$$\delta\Phi_\mathrm{m} = \frac{\delta E}{C_\mathrm{abs} + \int_V c_\mathrm{sen}(r) d^3r} \mu_0 \int\limits_V \frac{G(r/p)}{p} \frac{\partial M(B(\boldsymbol{r}), T)}{\partial T} d^3r \tag{2.32}$$

where C_abs is the total heat capacity of the absorber and c_sen the heat capacity per volume of the sensor. To calculate $\delta\Phi_\mathrm{m}$ from equation (2.32) one needs to know the magnetic field at each position inside the sensor. But as the geometry factor G is proportional to the magnetic field B we can instead integrate over the distribution $P(G)$ which is more convenient. Defining the weighted average $\langle X \rangle_\mathrm{G}$ of a quantity X as

$$\langle X \rangle_\mathrm{G} = \int P(G) X dG \tag{2.33}$$

and dividing by δE, we can rewrite equation (2.32) as the signal size per unit energy

$$\frac{\delta\Phi_\mathrm{m}}{\delta E} = \frac{V}{C_\mathrm{abs} + V \langle c_\mathrm{sen} \rangle_\mathrm{G}} \mu_0 \left\langle \frac{G}{p} \frac{\partial M}{\partial T} \right\rangle_\mathrm{G}. \tag{2.34}$$

2.5.4 Flux Change inside the SQUID-Magnetometer

The measured magnetic flux change $\delta\Phi_\mathrm{S}$ inside the SQUID loop depends on several quantities, the flux change $\delta\Phi_\mathrm{m}$ inside one of the meanders, the inductance L_m of one meander, the inductance of the bonding wires L_w that connect meanders and input coil, the inductance L_in of the input coil and the mutual inductance $M_\mathrm{is} = k\sqrt{L_\mathrm{in} L_\mathrm{S}}$ between input coil and the SQUID. The factor k is a dimensionless parameter which has usual value of 0.9 to 1. L_S is the inductance of the SQUID.
In [BUR04] a linear system of equations described the transformation of a flux change inside one of the meanders to a current change inside the input coil. These equations are derived from the current conservation law in nodal points and the flux conservation in superconducting loops. The resulting current in the input coil is given by

$$\delta I = \frac{1}{L_\mathrm{m} + 2(L_\mathrm{in} + L_\mathrm{w})} \delta\Phi_\mathrm{m} \tag{2.35}$$

The flux change inside the SQUID can be derived by multiplying this current with

the mutual inductance:

$$\delta\Phi_\mathrm{S} = M_\mathrm{is}\delta I = \frac{k\sqrt{L_\mathrm{in}L_\mathrm{S}}}{L_\mathrm{m} + 2(L_\mathrm{in} + L_\mathrm{w})}\delta\Phi_\mathrm{m} \tag{2.36}$$

In [FLE05] it was shown that the inductance of a meander with area A and pitch p can be calculated by

$$L_\mathrm{m} = l\mu_0\frac{A}{p}, \tag{2.37}$$

where l is a dimensionless parameter that depends on the ratio of the stripe width w and the witch p.

This equation neglects finite size effects at the edges of the meander area, i.e. it assumes an infinite length and number of stripes. The meander in this thesis has $w/p = 0.5$. The according l was calculated to be 0.220 [FLE05]. The sensitive area of one meander is $1 \times 1\,\mathrm{mm}^2$ with a pitch of $10\,\mu$m. So the inductance of one meander calculates to $L_\mathrm{m} = 27.6\,$nH. The inductance of the bonding wires is estimated to be $L_\mathrm{w} = 4.5\,$nH. The inductance of the input coil is $L_\mathrm{in} = 24\,$nH and the mutual inductance between input coil and SQUID is $M_\mathrm{is} = 1/(2.1\,\mu\mathrm{A}/\Phi_0) = 0.99\,$nH. With these values we calculate from equation (2.36) that only 1.2 % of the original flux change are transformed to the SQUID. This small value for the flux coupling is due to the small intrinsic inductance of the SQUID (< 1nH) compared to the inductance of one meander. In [FLE05] it was shown that the efficiency has a maximum for $L_\mathrm{m} = 2\,L_\mathrm{in}$. A slightly better efficiency can be achieved by impedance matching, e.g. by using a current sensor SQUID with somewhat smaller inductance.

2.5.5 Optimization of the Detection Geometry

The performance of a MMC depends not only on the signal size, but also on the signal-to-noise ratio. As the flux noise $\sqrt{S_\Phi}$ is proportional to the square root of the inductance $\sqrt{L_\mathrm{m}}$ of the meander [FLE05], we define the quantity $\mathcal{S}$ which is proportional to the signal-to-noise ratio:

$$\mathcal{S} = \frac{\delta\Phi/\delta E}{\sqrt{L_\mathrm{m}}}, \tag{2.38}$$

In order to get the best energy resolution of the detector we have to maximize the value of $\mathcal{S}$.
We introduce the magnetic flux change per unit energy $\delta\Phi_\mathrm{m}/\delta E$ from equation (2.34) and L_m from (2.37) to (2.38) and obtain

$$\mathcal{S} = \sqrt{\frac{\mu_0}{l}}\frac{h\sqrt{A/p}}{C_\mathrm{abs} + Ah\,\langle c_\mathrm{sen}\rangle}\left\langle G\frac{\partial M}{\partial T}\right\rangle. \tag{2.39}$$

The factors h and A are the height and the area of the sensor. Altogether $\mathcal{S}$ depends on 9 parameters:

$$\mathcal{S} = \mathcal{S}(C_{\mathrm{abs}}, g, \alpha, T, x, \overline{B}, A, \xi, w/p). \tag{2.40}$$

The g-factor and the interaction parameter α defined in equation (2.19) are fixed by the choice of the sensor material. The temperature T can be varied in a certain range that is limited by the available cooling techniques.
At a fixed temperature, the heat capacity C_{abs} of the absorber is given by its volume and material which are determined by the experiments to be conducted. In this work the absorber is supposed to stop β-particles up to an energy of 1 MeV using a 4π-geometry with a quantum efficiency close to unity. Therefore the absorber needs certain dimensions which will be determined with the help of a Monte Carlo simulation in chapter 5.1.
The remaining parameters can be varied in order to optimize the signal-to-noise ratio represented by the quantity $\mathcal{S}$. The parameter x denotes the concentration of the erbium ions inside the sensor. The value ξ is defined as the ratio of the sensor height and meander pitch, i.e. $\xi = h/p$. The meander geometry enters with its width w and pitch p. The persistent current I_0 through the meanders determines, at a given geometry, the mean magnetic field $\overline{B}$.
The optimal values of the parameters w/p and ξ were found to be $w/p = 0.425$ and $\xi = 0.36$. The condition on the heat capacity of the sensor was found to be [FLE05]

$$Ah \left\langle c_{\mathrm{sen}} \right\rangle = C_{\mathrm{abs}}. \tag{2.41}$$

For the pitch of the meander structure we choose $p = 10\,\mu$m and we optimize the detector to be operated at a temperature of $T = 50\,$mK. As mentioned above, for the material Au:Er we have $g = 6.8$ and $\alpha = 5$. We assume a cuboid gold absorber with the heat capacity $C_{\mathrm{abs}} = 1.45\,$nJ/K. Using the results of the optimization done in [FLE05], we obtain an erbium concentration of $x = 2000\,$ppm, a meander stripe width of $w = 4.25\,\mu$m, a sensor height of $h = 3.6\,\mu$m, a specific heat of the sensor material of $c_{\mathrm{sen}} = 390\,\mathrm{J/(K\,m^3)}$ as well as an optimal persistent current of $I_0 = 210\,$mA which refers to a mean magnetic field of $\overline{B} = 13\,$mT. If we insert the values of C_{abs}, c_{sen} and h into equation (2.41), we obtain an optimal sensor area of $A = 1\,\mathrm{mm^2}$. Under these optimal conditions the sensitivity of the detector , i.e. the flux change in the meander per unit of deposited energy, is calculated to be $\delta\Phi_{\mathrm{m}}/\delta E = 0.202\,\Phi_0/\mathrm{keV}$.
The actual parameters used in this work deviate from the optimal values listed above. The sputtering process, that was used for the sensor fabrication, create sensors with an erbium concentration of $x = 775\,$ppm. The actually used 4π-absorber has a heat capacity $C_{\mathrm{abs}} = 1.9\,$nJ/K at 50 mK.

3. Experimental Methods and Detector Fabrication

Magnetic microcalorimeters are operated at temperatures below 100 mK. The experiments described in this thesis were performed inside a dilution refrigerator which will be described, together with other experimental techniques, in the first section of this chapter. The MMC was read out by a two-stage SQUID magnetometer that is discussed in the subsequent section, followed by a description of the detector design and the fabrication of the detector and its components. Finally the experimental setup, the wiring arrangement and the data acquisition are presented.

3.1 Experimental Conditions

In the experiments discussed below a ^{3}He/^{4}He dilution refrigerator was used to cool the detector down to a temperature of about 20 mK. A detailed description of the principle of dilution refrigerators can, for example, be found in [ENS05]. The coldest part of a dilution refrigerator is the so-called mixing chamber. The refrigerator was produced by Oxford Instruments and was formerly used for neutron experiments. The mixing chamber and the inner vacuum can are surrounded by two radiation shields. These are thermally well connected to liquid helium and liquid nitrogen baths above the mixing chamber.

The temperature of the experimental platform is measured by a ruthenium-oxide thermometer which was calibrated at the Walther-Meißner-Institut in Munich down to a temperature of 21 mK. The logarithmic slope sensitivity of the thermometer at $T = 25\,\mathrm{mK}$ is $\mathrm{d}\log(R)/\mathrm{d}\log(T) = 1.6$. The thermometer was read out via a 4-wire measurement by a resistance bridge[1] with a relative resolution of $\mathrm{d}R/R = 2 \times 10^{-5}$ at $T = 25\,\mathrm{mK}$. The temperature of the experimental platform was controlled by an analog PID controller[2] with a temperature stability of 11 μK at 21 mK. This is about 1 order of magnitude worse than expected from the sensitivity of the thermometer and the resolution of the resistance measurement bridge. The reasons for this disagreement are not fully understood yet.

3.2 dc-SQUID Magnetometers

Energy input into a magnetic calorimeter results in a small change of magnetization of the sensor. In order to read out this signal it is necessary to use low noise magnetometers. Nowadays SQUIDs[3] are the most sensitive existing magnetometers with a very low noise and high bandwidth. This section discusses the basic principles of

[1] SIM900 mainframe, SIM921 AC resistance bridge, Stanford Research Systems, Inc., 1290-D Reamwood Avenue, Sunnyvale, CA 94089

[2] Model LR 130, Linear Research, San Diego, California

[3] Superconducting QUantum Interference Device

dc-SQUIDs and describes the SQUID configuration that was used within the experiments discussed below. The characteristics of the utilized SQUIDs will be shown and the general noise performance will be discussed.

3.2.1 General Features of dc-SQUIDs

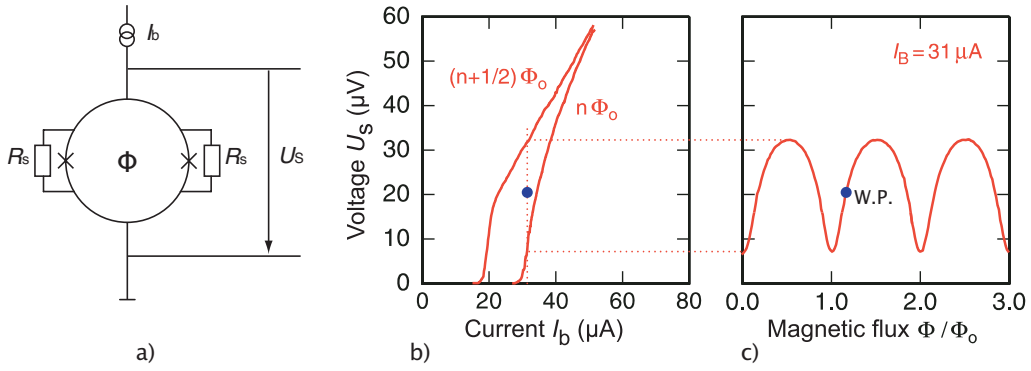

Figure 3.1 a) Schematic of a SQUID magnetometer. b) SQUID voltage against bias current for the case of a magnetic flux $\Phi = n\,\Phi_0$ or $\Phi = (n+1/2)\,\Phi_0$ inside the SQUID. c) $V-\Phi$ curve for the bias current denoted in b). [FLE03]

The working principle of dc-SQUID magnetometers is based on the quantum mechanical phenomenum that Cooper pairs in superconductors can be described by a common macroscopic wave function. The two essential consequences are the flux quantization inside closed superconducting loops and the Josephson effect that describes the coherent tunneling of Cooper pairs through thin normal conducting areas. A detailed description of both effects can be found, for example, in [ENS05].

Figure 3.1a shows the schematic of a dc-SQUID. It consists of a superconducting loop that is interrupted by two Josephson junctions which are depicted by the crosses. Josephson junctions are often realized as metal oxid layers of a few nanometers thickness in between two superconducting metals. Each Josephson junction is shunted by a resistor R_S to eliminate hysteresis on the current-voltage characteristics [CLA96].

A dc-SQUID is operated at a bias current I_b. Up to a critical current I_c the Cooper pairs tunnel coherently through the Josephson junctions without any voltage drop across the SQUID. The value of I_c depends on the geometry of the junctions and on the magnetic flux Φ inside the loop. Above the critical current a finite voltage drop U_S, that depends on the magnetic flux, occurs across the SQUID.

Figure 3.1b shows the current-voltage-curve of the two extreme cases that the SQUID loop is penetrated by a flux $\Phi = (n+1/2)\,\Phi_0$ and $\Phi = n\,\Phi_0$, respectively. The factor $\Phi_0 = h/2e = 2.07 \times 10^{-15}\,\mathrm{Tm}^2$ is the magnetic flux quantum and n is an integer. If we apply a bias current I_b which is bigger than the critical current I_c, the voltage drop across the SQUID depends periodically on the magnetic flux Φ, as depicted in figure 3.1c. Hence, it is possible to measure magnetic flux with a

dc-SQUID.
The dc-SQUIDs that were used in this work are current sensor SQUIDs. This means that the magnetic flux which enters the SQUID loop is generated by a current that flows through an input coil which is situated on the same silicon chip as the SQUID. This setup was already shown in chapter 2.5.1.

3.2.2 Single-Stage SQUID Readout

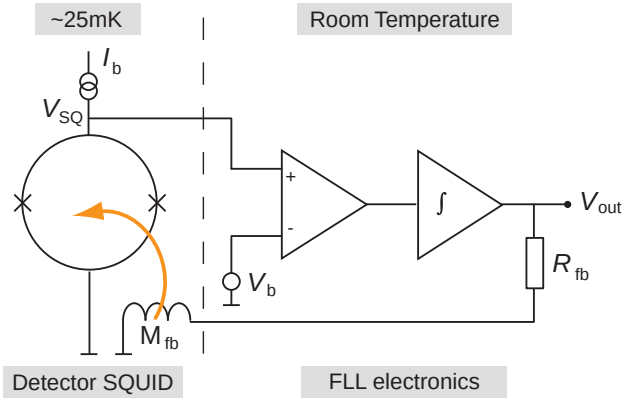

Figure 3.2 A dc-SQUID in single-stage configuration with a succeeding FLL-circuit.

In the last section we looked at the strong non-linear behavior of the $V-\Phi$ characteristics which is not suited to measure large flux changes. However, one can find a small region around the working point that offers a unique relation between voltage and magnetic flux. From the $V-\Phi$ characteristics in figure 3.1c one can see that this region has to be smaller than $\delta\Phi \approx \pm\Phi_0/4$.

In order to extend the measuring range of the SQUID one can add an electronic circuit to linearize the $V-\Phi$ curve. Figure 3.2 shows a schematic of this so-called flux-locked-loop (FLL) circuit. The bias current I_b is set to the SQUID's working point and a magnetic flux causes a voltage drop V_{SQ} according to the $V-\Phi$ curve. The voltage difference $\Delta V = V_{SQ} - V_b$, with V_b being the voltage of the working point, is amplified at room temperature. The output of the amplifier is the input of a succeeding integrator. As long as the input voltage of this integrator is non-zero, it changes its output voltage V_{out}. This output voltage drops across the feedback resistor R_{fb} and the feedback[4] coil. The resulting current generates a magnetic flux inside the SQUID via the mutual inductance M_{fb} and compensates the initial flux to zero.

As mentioned in chapter 2.4, the energy resolution of magnectic microcalorimeters depends, besides other contributions, on the noise of the magnetometer. The intrinsic noise of a SQUID depends on the working temperature T, the inductance L_S of the SQUID, the value R_S of the shunt resistors and the parasitic capacitance of the Josephson junctions. In [TES77] a detailed numerical calculation of the intrinsic

[4] In many SQUID setups the same structure is used as input coil and feedback coil.

flux noise of optimized dc-SQUIDs led to

$$\sqrt{S_{\Phi,\mathrm{S}}} = \frac{1}{\frac{\partial V}{\partial \Phi}|_{\mathrm{W.P.}}}\sqrt{S_{\mathrm{V,S}}} = \sqrt{\frac{16 k_{\mathrm{B}} T L_{\mathrm{S}}^2}{R_{\mathrm{S}}}}. \tag{3.1}$$

$\sqrt{S_{\mathrm{V,S}}}$ and the flux-to-voltage conversion factor $\frac{\partial V}{\partial \Phi}|_{W.P.}$ at the working point can be determined experimentally. With a typical SQUID of $L_{\mathrm{S}} = 100\,\mathrm{pH}$ and $R_{\mathrm{S}} \approx 5\,\Omega$ at a temperature of $T = 4.2\,\mathrm{K}$ we obtain an intrinsic flux noise of $\sqrt{S_{\Phi,\mathrm{S}}} = 0.66\,\mu\Phi_0/\sqrt{\mathrm{Hz}}$. The FLL electronics[5] used within this thesis has an input noise level of $\sqrt{S_{\mathrm{V,el}}} = 0.33\,\mathrm{nV}/\sqrt{\mathrm{Hz}}$. With a typical voltage-to-flux transfer coefficient of $V_\Phi = 200\,\mu\mathrm{V}/\Phi_0$ at the working point this corresponds to a flux noise of $\sqrt{S_{\Phi,\mathrm{el}}} = 1.65\,\mu\Phi_0/\sqrt{\mathrm{Hz}}$.
As the SQUID noise and the electronics noise are independent of each other, the spectral power densities add up incoherently:

$$S_\Phi = S_{\Phi,\mathrm{S}} + \frac{S_{\mathrm{V,el}}}{V_\Phi^2}. \tag{3.2}$$

For the above values one obtains $\sqrt{S_\Phi} = 1.78\,\mu\Phi_0/\sqrt{\mathrm{Hz}}$. The contribution of the electronics noise is already dominating at 4.2 K. At temperatures in the millikelvin regime it becomes even more important because the intrinsic flux noise of the SQUID is strongly reduced.
It has to be said that the intrinsic SQUID noise cannot be reduced to an arbitrarily small value, as equation (3.1) suggests. The reason is that the energy sensitivity $\epsilon = S_{\Phi,\mathrm{S}}/2L_{\mathrm{S}}$ of a SQUID is limited to a minimum value by quantum fluctuations. Within this limit the SQUID noise does not depend on temperature, but it is exclusively determined by its inductance obeying $\sqrt{S_{\Phi,\mathrm{S}}} \propto \sqrt{L_{\mathrm{S}}}$.
In order to reduce the total noise one has to reduce the electronics noise. This could be done by reducing the input noise level by moving the electronics from room temperature to lower temperatures. Another, independent possibility is to increase the value of V_Φ. This can be done by using a two-stage configuration which will be discussed in the next section.

3.2.3 Two-Stage SQUID Readout

Figure 3.3 shows the SQUID setup that was used in this thesis. In the following the left SQUID will be called detector SQUID and the right one will be called amplifier SQUID. In the experiments described below both SQUIDs were mounted on the experimental platform of the mixing chamber of a dilution refrigerator and therefore both were operated at the same temperature. All experiments were done below 500 mK.

The detector SQUID operates at a bias current I_{b1}. If a magnetic flux $\delta\Phi_1$ enters the SQUID through its input coil with inductance L_{i} a voltage drop V_1 occurs across the SQUID according to its $V-\Phi$ characteristics. This voltage results in a current $\delta I_1 = V_1/R_{\mathrm{g}}$ through the gain resistor R_{g} and the input coil of the amplifier SQUID

[5] XXF-1 SQUID electronics, commercially available at Magnicon GbR, Hamburg, Germany

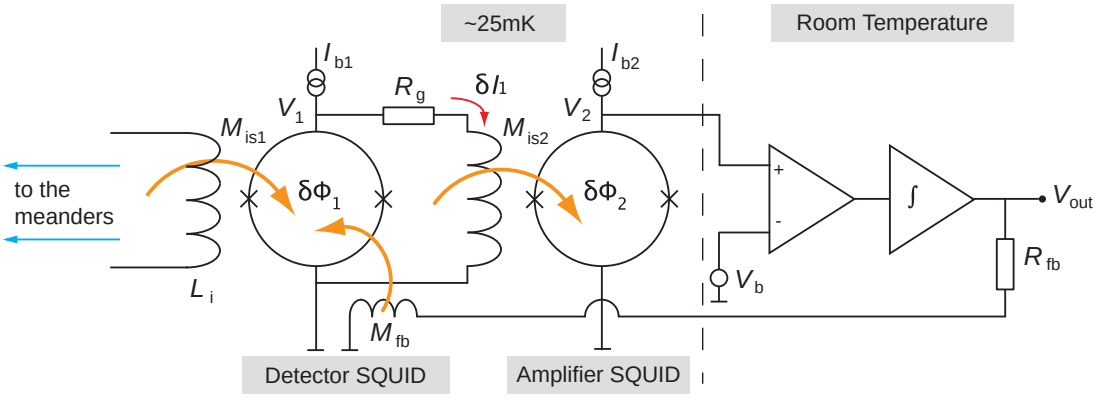

Figure 3.3 Two-stage SQUID configuration with a succeeding FLL-circuit. A magnetic flux from outside the setup enters the detector SQUID and the resulting voltage drop V_1 produces a current inside the input coil of the amplifier SQUID. The resulting flux inside the amplifier SQUID generates a voltage drop V_2 that is amplified by the succeeding electronics. The flux compensation inside the detector SQUID works analogously to the flux compensation in a single SQUID with FLL-electronics.

which is operated at a bias current I_{b2}. The current δI_1 generates a magnetic flux $\delta\Phi_2 = M_{\mathrm{is2}}\delta I_1$ which results in a voltage drop across the amplifier SQUID that is amplified by the FLL-electronics at room temperature. Equally to the single-stage configuration, the output of the succeeding integrator generates a voltage that results in a current through the feedback coil which is located at the detector SQUID. Thus the $V-\Phi$ curve of the two-stage SQUID readout is linearized.

With this setup the magnetic flux inside the detector SQUID is converted into a flux inside the amplifier SQUID. It is important that the resistor R_{g} is chosen such that the overall voltage swing of the detector SQUID changes the flux in the amplifier SQUID by less than one flux quantum. Otherwise the $V-\Phi$ curve of the detector SQUID would convert into a V–Φ curve of the two-stage setup with different working points and different slopes. In order to avoid multiple working points, the flux-to-flux conversion factor $G_\Phi = \delta\Phi_2/\delta\Phi_1$ at the working point of a two-stage SQUID setup is limited by a value of about 3 [FLE03]. This factor can also be expressed by

$$G_\Phi = \frac{V_\Phi}{V_{\Phi_1}}, \tag{3.3}$$

where V_{Φ_1} and V_Φ are the slopes in the working points of the $V-\Phi$ curves of the detector SQUID and the two-stage setup respectively.

The $V-\Phi$ characteristics of the amplifier SQUID[6] and the two-stage setup, that was used in this thesis, are depicted in figure 3.4. The left curve was obtained by inducing an increasing magnetic flux Φ_2 into the amplifier SQUID and measuring

[6]SQUID-array C503E19, designed and fabricated at the Physikalisch-Technische Bundesanstalt in Berlin, Germany.

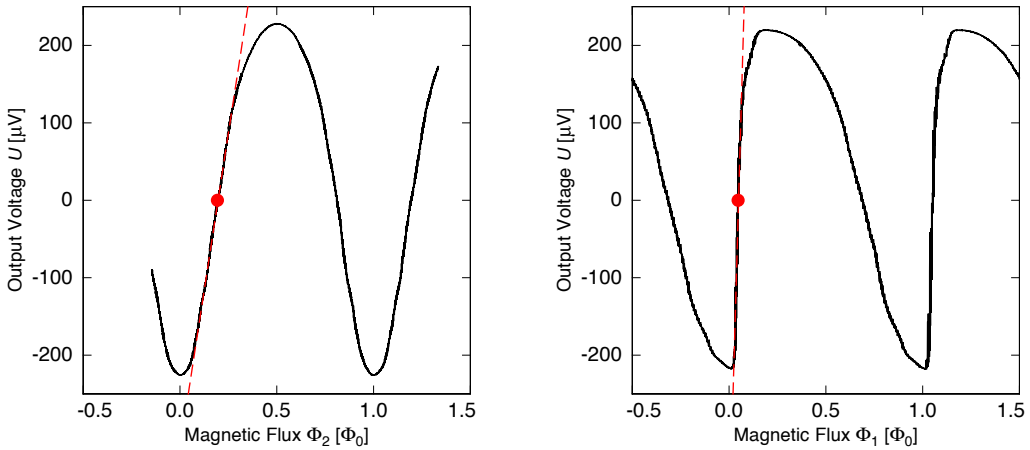

Figure 3.4 **Left:** Characteristic of the amplifier SQUID used in this work at a temperature of 22 mK. The magnetic flux Φ_2 enters the amplifier SQUID and the voltage drop is measured across it. **Right:** Characteristic of the two-stage SQUID-setup at a temperature of 22 mK. The magnetic flux Φ_1 enters the detector SQUID and the voltage drop is measured across the amplifier SQUID. The plot shows the typical behavior for a SQUID with additional positive feedback.

the voltage drop across the amplifier SQUID. The detector SQUID was not present in this setup. The right curve was obtained by inducing a flux Φ_1 into the detector SQUID and measuring the voltage drop across the amplifier SQUID.

The detector SQUID[7] has a special feature which is called additional positive feedback (APF) [DRU04]. In figure 3.5 the schematic circuit of APF is shown. A resistor R_{APF} and a coil with inductance L_{APF} are connected in parallel to the SQUID which is operated at the working point.

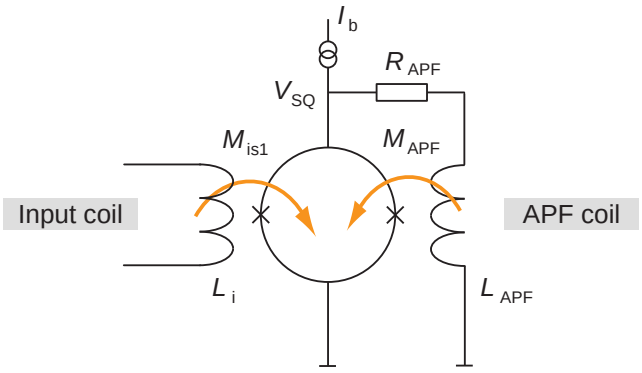

Figure 3.5 A SQUID with additional positive feedback (APF). The current inside the additional coil L_{APF} leads to an asymmetry of the $V-\Phi$ characteristics of the SQUID as shown in figure 3.4 (right).

A magnetic flux, that enters the SQUID via the input coil, causes a voltage drop V_{SQ} across the SQUID and the additional current branch. The resulting current flowing through the APF coil generates an additional flux in the SQUID via the

[7] Type C4XS1, designed and fabricated at the Physikalisch-Technische Bundesanstalt in Berlin, Germany.

mutual inductance M_{APF}. This causes one side of the $V-\Phi$ characteristics, e.g. the side with the positive slope, to get steeper and the other one to get less steep.

This feature leads to an asymmetry of the $V-\Phi$ characteristics of the detector SQUID and accordingly to an asymmetry of the $V-\Phi$ characteristics of the two-stage setup. Therefore there are two flux-to-flux conversion factors, depending on the slope at the working point. From figure 3.4 we obtain $G_{\Phi,\mathrm{p}} = 2.6$ for the positive slope and $G_{\Phi,\mathrm{n}} = 0.6$ for the negative slope. For this measurement both SQUIDs were operated at a temperature of 22 mK.

In the case of the single-stage configuration it was shown that the total noise described by equation (3.2) was dominated by the succeeding electronics. At a given input voltage noise this is due to the voltage-to-flux conversion factor V_Φ. The electronics noise can be reduced by the use of an amplifier SQUID.

The total apparent flux noise of the detector SQUID in a two-stage configuration can be written as the incoherent sum of 4 contributions:

$$S_\Phi = S_{\Phi,1} + \frac{S_{\Phi,2}}{G_\Phi^2} + \frac{S_{\Phi,\mathrm{el}}}{V_\Phi^2} + \frac{M_{\mathrm{is2}}^2}{G_\Phi^2}\frac{4k_\mathrm{B}T}{R_\mathrm{g}}. \tag{3.4}$$

The first term, $S_{\Phi,1}$, is the intrinsic flux noise of the detector SQUID. The second term, $S_{\Phi,2}$, describes the contribution of the intrinsic flux noise of the amplifier SQUID to the apparent flux noise of the detector SQUID. It is reduced by the flux-to-flux amplification G_Φ at the working point. The third contribution in equation (3.4) stands for the apparent noise of the detector SQUID caused by the voltage noise $S_{\mathrm{U,el}}$ of the amplifier at room temperature. Here V_Φ denoted the slope of the $V-\Phi$ characteristics of the two-stage SQUID setup at the working point. The last term describes the contribution of the thermal voltage noise of the resistive elements in the circuit that is connected to the input coil of the amplifier SQUID, assuming that the dynamical resistance R_{dyn} of the detector SQUID is big compared with the gain resistor R_g. Here, M_{is2} is the mutual inductance between the amplifier SQUID and its input coil, as was depicted in figure 3.3. This last contribution can in principle be made almost arbitrarily small by installing these resistive parts at millikelvin temperatures. Altogether the noise of a two-stage SQUID setup is smaller than the one of the single-stage setup because $S_{\mathrm{U,el}}$ of the amplifier at room temperature dominates the latter case. The flux-to-flux amplification G_Φ helps to reduce this contribution in the two-stage setup.

3.3 Detector Chip

3.3.1 Injection of the Persistent Current

In chapter 2.5.1 the meander shaped pick-up coil was discussed. As pointed out, the magnetic field that is necessary to magnetize the sensor is generated by a persistent current inside the meanders. The procedure of injecting a persistent current into the superconducting meanders is discussed in this section by considering figure 3.6.

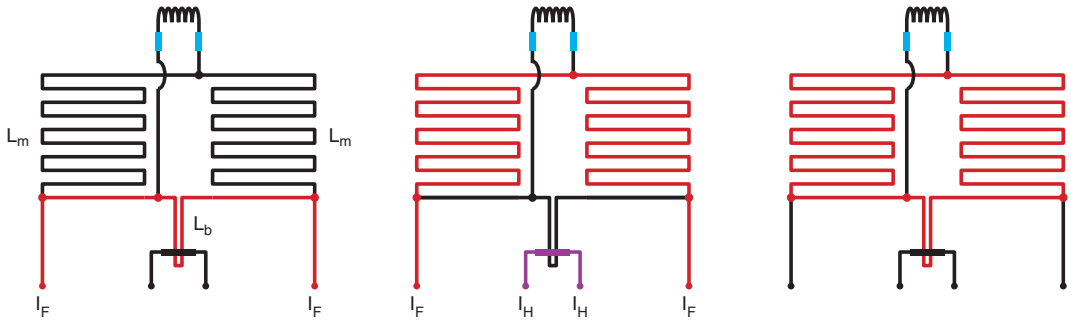

Figure 3.6 Schematic for the procedute of injecting a persistent current.

The left figure sketches the initial situation. The meanders with a total inductance of $2L_\mathrm{m}$ are connected in series with a U-shaped bypass of niobium leads which has the much smaller inductance L_b. An ohmic resistor covers this structure at its very end. A field current I_F is injected through the field current bond pads. This current splits according to the inductances $2L_\mathrm{m}$ and L_b. As the meanders form a superconducting loop in this state, magnetic flux can not enter. Since the inductance $2L_\mathrm{m}$ of the meanders is much higher than the inductance of the U-shaped bypass, most of the current flows through L_b.

In chapter 2.5.1 we depicted the connection of the meanders with the input coil of a detector SQUID. These connections are done by aluminum bond wires. If the input coil of the SQUID had a superconducting connection to the meanders, a part of the current would be injected into the input coil which would decrease the performance of the SQUID. Therefore the procedure must be executed at a temperature T that is higher than the critical temperature of aluminum $T_\mathrm{c,Al} = 1.2\,\mathrm{K}$. At the same time, the niobium of the meanders has to stay superconducting which is fulfilled as long as $T < T_\mathrm{c,Nb} = 9.3\,\mathrm{K}$.

Now we inject a current I_H into the heater as is depicted in the second figure. The resulting temperature rise must be such that the niobium bypass below becomes normalconducting. The full current I_F then flows through the inductance $2L_\mathrm{m}$ and the magnetic flux $\Phi = 2L_\mathrm{m}I_\mathrm{F}$ enters the pick-up coil. After switching off I_H, the niobium bypass becomes superconducting again and the magnetic flux is trapped inside a superconducting loop. The field current I_F is subsequently shut down and, as flux conservation holds, a persitent current I_0 stays inside $2L_\mathrm{m} + L_\mathrm{b}$ as depicted in the third figure. With $2L_\mathrm{m} \gg L_\mathrm{b}$ we get

$$I_0 = \frac{2L_\mathrm{m}}{2L_\mathrm{m} + L_\mathrm{b}} I_\mathrm{F} \approx I_\mathrm{F} \tag{3.5}$$

The value of I_F is limited by the critical current of the sputtered niobium film and will be discussed in chapter 4.1.
The necessary value of I_H to drive the U-shaped meander bypass normal conducting depends on the critical temperature of the sputtered niobium, the heat switch resistance, the thermal Kapitza resistance at the material interfaces.

3.3.2 Description of the Detector Chip

In chapter 2 we discussed the detection principle of metallic magnetic calorimeters and the properties of meander shaped pick-up coils. To practically realize such a detector one can use microfabrication and photolithography techniques which will be discussed in section 3.4. In section 3.2.3 the readout mechanism via a two-stage SQUID setup was discussed. Therefore the detector chip to be constructed needs bond pads as interfaces to the detector SQUID. Furthermore, the meanders on top of the detector chip are supposed to carry a persistent current which can be injected by using a persistent current switch as discussed in section 3.3.1. Subsequently sensors have to be placed on top of the meanders together with the absorber. The following text describes the developed detector chip.

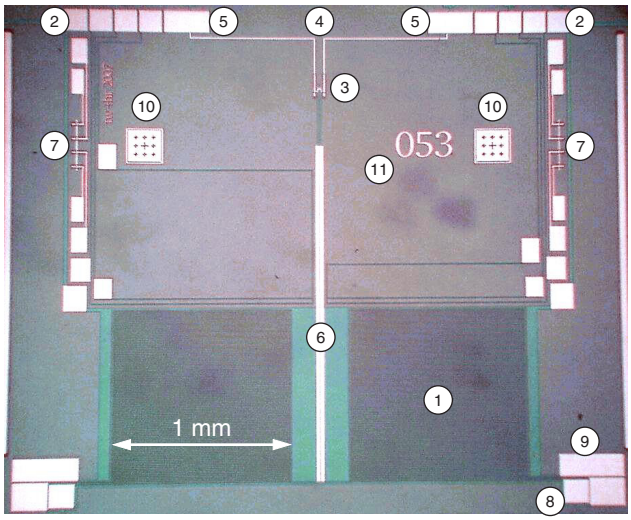

Figure 3.7 (1) Meanders (2) Field current bond pads (3) Persistent current switch (4) Supply lines for the heater of the persistent current switch (5) Heater current bond pads (6) Niobium stripe to reduce the inductance of the meander bypass (7) Testing structures (8) Bond pads to the input coil of the SQUID (9) Bond pad to close the box, see text (10) alignement marks

Figure 3.7 shows a microscope picture of the meander chip type that was designed, fabricated and used within this work to measure the β-spectrum of ^{63}Ni. The substrate is a squared slice of silicon with a thickness of 0.3 mm. It has a 240 nm thick SiO_2-layer on top to isolate the semiconducting silicon electrically. Most structures that can be seen in the picture consist of niobium which was sputtered with a thickness of 400 nm. During the sputtering process the substrate was fixed on a metal holder with a controlled temperature of 200 °C. The meanders (1) as well as the supplying niobium stripes were subsequently anodized[8] and covered by a sputtered SiO_2-layer of 300 nm thickness. During the anodization the niobium is oxidized at the surface in order to avoid electrical contact to the layers above. The SiO_2-layer protects the niobium stripes mechanically and improves the electrical isolation and reduces the sensitivity to electrostatic discharge. The bond pads at the edges of the chip are neither anodized nor covered by SiO_2 because they need to be electrically connected. The bond pads (8) which connect the detector chip and the SQUID are situated next to a bond pad (9) that is used to close a box around the meander. In

[8] For anodization see section 3.4.

[FLE05] it was pointed out that this reduces the magnetic Johnson noise in the pick-up coil. Other parts (7) that can be seen in the picture serve as testing structures. Position number (10) denotes alignment marks needed in this multi layer fabrication process.

The heater of the persistent current switch (3) is sputtered onto the U-shaped end of the niobium bypass which is, together with the meander shaped pick-up coil, part of a superconducting loop. The heater consists of a 10 nm thick layer of copper and a 50 nm thick layer of gold. The copper is used as a sticking layer for the gold which, by itself, does not stick well to SiO_2. The persistent current switch will be discussed in more detail in chapter 4.2. Afterwards a second niobium layer is sputtered above which has a thickness of 400 nm, like the first niobium layer. Contrary to the first layer, the niobium of this layer was sputtered in a different sputtering system and the substrate was placed on top of a metal holder with a temperature of 17 °C. Only two niobium structures on the chip are part of the second niobium layer: the supply lines to the heater (4) and a niobium stripe (6) that lies above the U-shaped meander bypass of the first niobium layer. This stripe reduces the inductance of the bypass due to its diamagnetism.

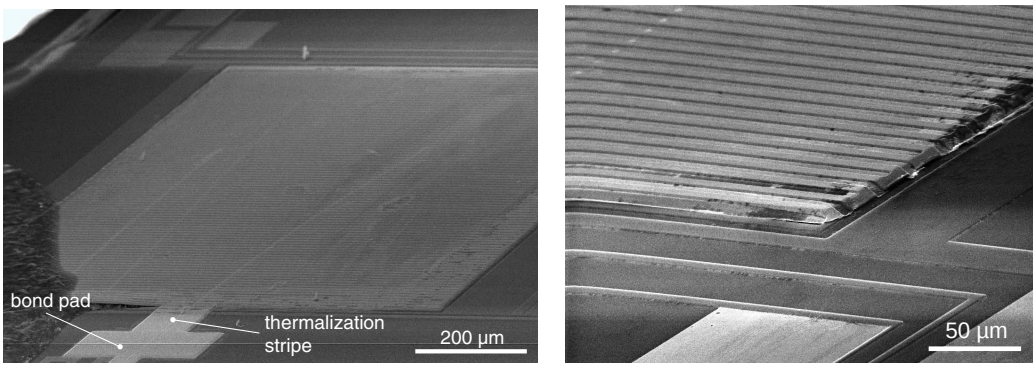

Figure 3.8 **Left:** Sputtered Au:Er-sensor on top of one meander area. The thermalization stripe joins the sensor and a rectangular bond bad. The dark area on the left is conductive silver lacquer that was used within electron microscopy. **Right:** Magnification of a sensor corner. As the sensor was lithographically structured, it is a well defined square that is flush with the meander area. Even though the sensor height is 3 μm, the meander structure emerges from the sensor surface.

Figure 3.8 shows a SEM[9]-picture of the Au:Er-sensor that was used in this work. The usage of only one sensor does not take advantage of the gradiometric principle which was discussed in chapter 2.5.1. The reason for only one sensor is the possibility to measure the magnetization as a function of temperature, which is not possible with a gradiometer consisting of two sensors. The Au:Er-sensor has an erbium concentration of 775 ppm and a thickness of 3 μm. It was sputtered above a 50 nm thick copper sticking layer that was sputtered onto the 300 nm thick SiO_2-layer which covers the niobium meanders.

[9]Scanning Electron Microscope

In order to allow for high activity β-sources, the duration of a pulse and in particular its decay time must kept small. This can be done by additional links to the thermal bath. The thermalization stripe shown at the bottom of the picture can be connected to the thermal bath via gold bond wires. The attached bond pad has an area of 250 μm $\times$100 μm to allow for multiple gold bond wires. The size of the thermalization stripe is 100 μm$\times$100 μm which was estimated to be the necessary geometry for a decay time of 1 ms at a temperature of 30 mK.

Within this work the β-spectrum of ^{63}Ni was measured by using a gold absorber with a 4π-geometry. The positioning of the source into the absorber as well as the connection to the sensor will be discussed in chapter 4.3.5.

3.4 Microfabrication of Metallic Magnetic Microcalorimeters

Magnetic microcalorimeters are produced by using methods of microfabrication. The production of the MMC that was used in this thesis involved dc- and ac-magnetron sputtering, photolithography, chemical etching, lift-off processes and electroplating. Detailed descriptions of these processes can be found, for example, in [MAD02] or [MEN01]. As the electroplating of MMC gold absorbers was developed within this thesis, it will be discussed separately in chapter 4.3. The following text describes the fabrication of the MMC without absorber.

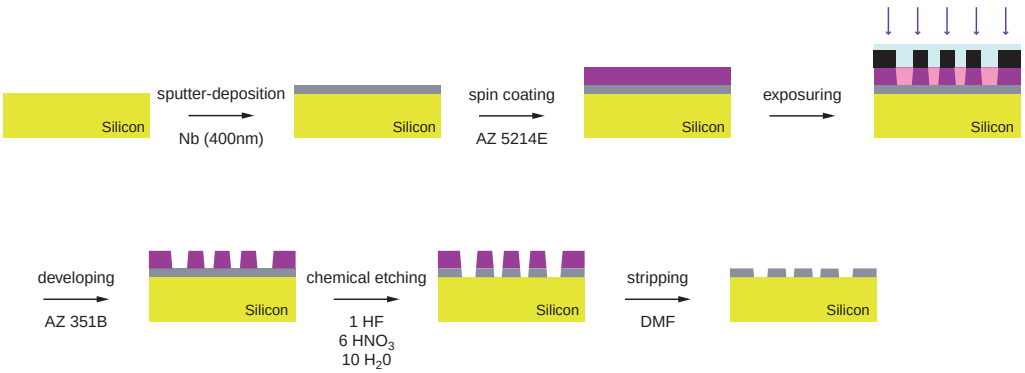

Figure 3.9 Production of niobium meanders. After niobium sputtering and covering the surface with a positive photoresist, the wafer is covered by a mask that permits the exposure of certain parts of the resist by ultraviolet light. The exposured parts become dissolvable and are removed by a special solvant. The succeeding etching step removes the niobium at the exposured parts and the lithographic process is completed after stripping the resist.

The production of niobium meanders is depicted in figure 3.9. The starting point is a 2" silicon wafer[10] with a thickness of 0.3 mm and a SiO_2-covering with a thickness of 240 nm. The plain wafer is moved into the vacuum chamber of a sputtering

[10]Si-Mat Silicon Materials, Malteserstrasse 444a, 86899 Landsberg am Lech, Germany

machine and put on top of a metal holder that has a controlled temperature of 200 °C. Argon is used as sputtering gas at a pressure of 10^{-3} mbar and the wafer is sputtered at a power of 500 W. After the sputtering a positive photoresist[11] is spinned onto the niobium film. Then the wafer is covered by a mask and parts of the photoresist are exposed to ultaviolet light which makes it dissolvable. In a developing step only the niobium for the desired structures remains protected by the photoresist. Afterwards the unprotected niobium is chemically etched and the photoresist is subsequently removed by a solvant.

The next steps are the anodization of the niobium surface and the sputtering of SiO_2, as schematically depicted in figure 3.10. The wafer is again partially covered by the positive photoresist in order to protect the bond pads which need to stay conductive to allow for electrical connections by means of bond wires. For the anodization the wafer is put into a container with an anodization liquid[12] and the niobium structures are connected to the anode of a power supply. An opposing platinized titanium sheet is connected to the cathode. Switching on the power supply a redox reaction starts at the electrodes, and the not covered niobium surfaces transform into niobium oxide which has a large resistance. Without any step in between, the wafer is covered with SiO_2 by ac-sputtering which leads to a uniformly isolating film on top of the wafer. Afterwards the photoresist and the SiO_2 lying above are removed in a so-called lift-off process.

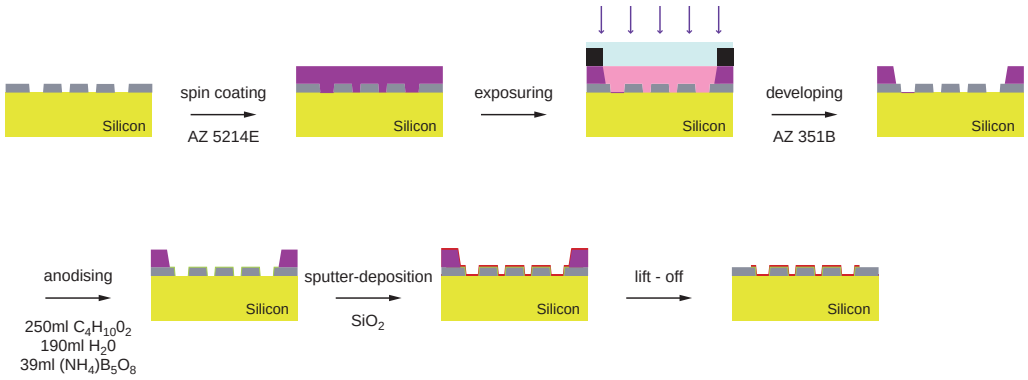

Figure 3.10 Anodization and lift-off process. The exposure and development is analogous to figure 3.9. Only the bond pads are covered. The rest is first anodized and then sputtered by SiO_2. Finally the SiO_2 above the bond pads is removed in an ultrasonic bath.

The next two steps are the fabrication of the Cu/Au-heater of the persistent current switch and the second niobium layer which are both produced in lift-off processes. The production of the second niobium layer cannot be done with a heated substrate like in the case of the first niobium layer because the used photoresist is not stable against high temperatures. Therefore the second niobium layer is sputtered with the wafer fixed on top of a water-cooled holder at a temperature of 17 °C.

[11] AZ 5214E, distributed by MicroChemicals GmbH, Schillerstr. 18, 89077 Ulm, Germany
[12] Mixture of 250 ml of $C_4H_{10}O_2$, 190 ml of H_2O and 39 ml of $(NH_4)B_5O_8$.

The Au:Er-sensor is the last sputtering process. Like the previous layers the sensor is fabricated in a lift-off process, but this time with a negative photoresist[13]. The Au:Er-target has an erbium concentration of 810 ppm, but measurements showed that the resulting sensors have an erbium concentration of only 775 ppm. Presently, tests with the method of co-sputtering are proceeded, in which two targets are used for the sensor fabrication. One is a pure gold target and the other one is a Au:Er-target with an erbium concentration of 1750 ppm. With co-sputtering it is possible to produce sensors with a desired erbium concentration up to this limit [PAB08].

3.5 Experimental Setup

3.5.1 Detector Setup

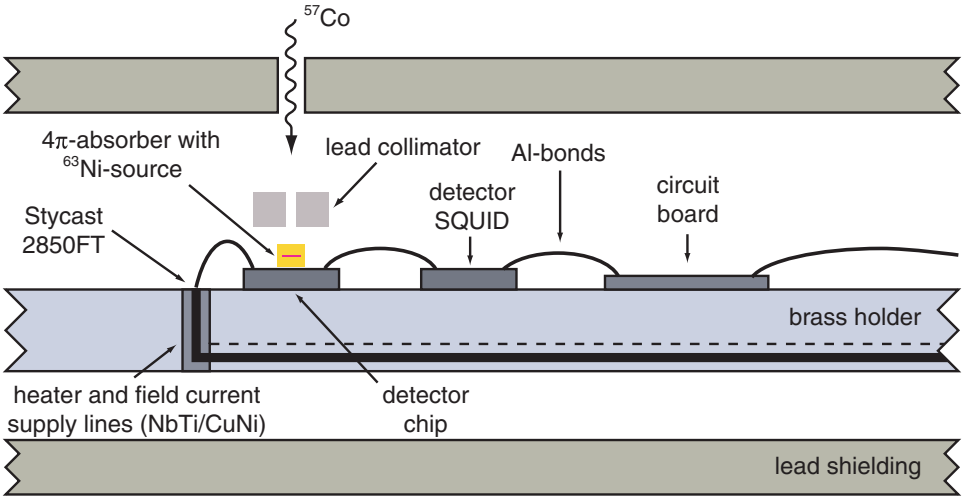

Figure 3.11 Schematic of the experimental setup

Figure 3.11 shows a sketch of the experimental setup used in this thesis. The gold absorber on top of the detector chip completely encases the ^{63}Ni-source. The detector chip is glued with EPO-TEK[14] onto the brass holder while the detector SQUID is glued with GE 7031 Varnish. Both kinds of glue have a rather large thermal conductivity at low temperatures and therefore establish a good thermal contact. A metal holder is needed for a good thermal contact between the experiment and the cold stage of the cryostat, and the material brass is chosen as it has a comparably small electrical conductivity and therefore a rather small magnetic Johnson noise. Two superconducting aluminum bonds with a diameter of 25 μm connect the meanders to the input coil of the detector SQUID. The feedack coil and the bias current bond pads of the detector SQUID are connected to a circuit board that is connected to

[13] AZnLOF 2070, distributed by MicroChemicals GmbH, Schillerstr. 18, 89077 Ulm, Germany

[14] EPO-TEK 301-2FL, Polytec PT GmbH Polymere Technologien, Polytec-Platz 1-7, 76337 Waldbronn, Germany

the amplifier SQUID outside the sketch. On the left side of the detector chip, four superconducting NbTi/CuNi-wires with a diameter of 150 μm stick out of a hole inside the brass holder. The wires are embedded in a matrix of the low temperature glue Stycast 2850FT and are connected to the field and heater current supply lines of the detector chip.

The brass holder is surrounded by a superconducting lead shielding that suppresses the penetration of magnetic fields. A small hole inside the shielding allows γ-rays to enter from an external ^{57}Co calibration source. In order to focus the radiation onto the absorber a lead collimator is used. This collimator has a thickness of 600 μm and a collimation hole with 200 μm diameter. It is fixed above the absorber by an additional brass holder which is not shown in the sketch.

Figure 3.12 shows a picture of the experimental setup without lead shielding and collimator. The picture can be considered as top view of the lateral view of the schematic in figure 3.11.

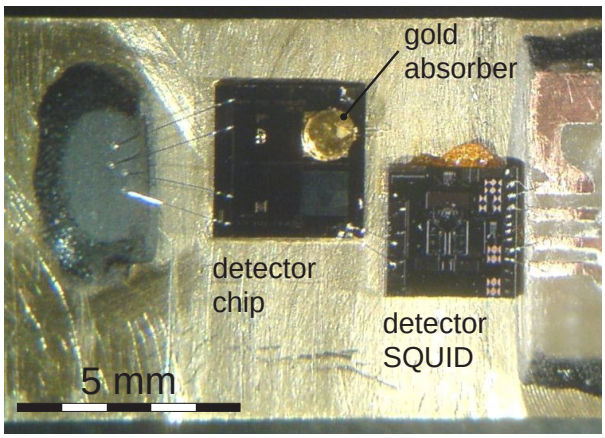

Figure 3.12 The picture of the experimental setup can be considered as top view of the lateral view of figure 3.11. The black bunch on the left is the Stycast 2850FT in which the NbTi/CuNi-wires are embedded. The blob next to the detector SQUID is GE 7031 Varnish that was squeezed out.

The wiring of the experimental setup is depicted in figure 3.13. Multiple copper wires run from room temperature down to the helium bath where they are in good thermal contact with the 4.2 K stage. They are electrically connected to the superconducting NbTi/CuNi-wires, which lead to the detector, and the SQUIDs that are at the mixing chamber temperature. The wires are inside Cu:Nb-capillaries in order to shield them against high frequency fields. Several copper heat sinks thermalize the wires at different temperature stages from 4.2 K down to the mixing chamber region.

3.5.2 Data Acquisition and Analysis

Particles hitting the absorber produce heat pulses inside the sensor that convert into magnetic flux pulses inside the input coil of the detector SQUID as described in chapter 2.5.4. The two-stage SQUID setup, which was discussed in section 3.2.3, converts the magnetic flux pulse into a voltage pulse. The output voltage of the two-stage SQUID setup is split into two channels. One channel is the signal that is stored afterwards and the other channel serves as a trigger signal. Each channel

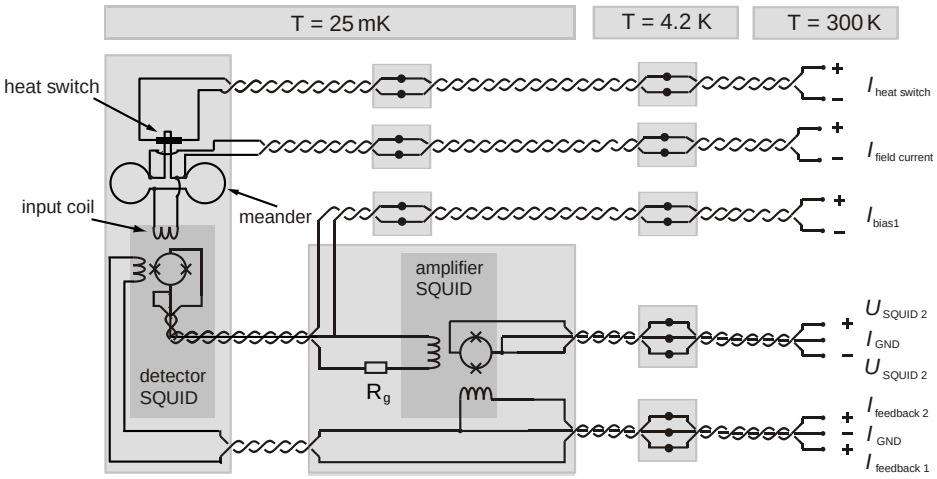

Figure 3.13 Arrangement of the wiring

is preprocessed by a low-noise preamplifier[15]. Both channels are connected to an oscilloscope card[16] where the signal and the trigger are digitized. The utilized computer software for the data acquisition and the controlling of the oscilloscope card is described in [SCH00]. If the trigger pulse exceeds the previously adjusted trigger level, the signal pulse is recorded with a 12 bit resolution. A pulse is recorded within a certain time interval, the time window. Within this time window 1024 to 16384 voltage samples can be acquired. The recording of a pulse starts before the trigger level is exceeded. This time is usually set to one quarter of the time window size. Technically, this is accomplished by a continuously working ring buffer. In addition to pulse events, the so-called baseline was acquired. The baseline tracks correspond to time windows in which no voltage signal exceeded the trigger level. With the help of the baseline one can investigate the energy resolution of the detector.

3.5.3 Internal Source and Calibration Source

During the experiment the gold absorber was exposed to two kinds of particles: electrons from the internal β-source and photons from the external calibration source. The internal source is the β^--emitter ^{63}Ni that was described in chapter 2.1.3. The estimated β-source activity is 25 Bq.

For the calibration of the detector a ^{57}Co-source was used. ^{57}Co is a γ-emitter with three dominant lines at 14.4 keV, 122.1 keV and 136.5 keV [LBN02]. As the utilized source is encapsulated in a thin-walled stainless steel housing, the line at 14.4 keV is strongly suppressed. The distance from the source to the absorber was about 2 cm and as the source activity was about 500 Bq, therefore only a low count rate was expected.

[15] SRS560, Stanford Research Systems
[16] CompuScope SAC-8012A/PCI, Gage, Montreal, Canada.

4. Progress of Metallic Magnetic Microcalorimeters

4.1 Properties of Sputtered Niobium Films

In chapter 2 we saw that the signal size of a metallic magnetic calorimeter depends on the magnetic field distribution inside the sensor and that the magnetic field is proportional to the persistent current inside the pick-up coil. The persistent current is limited by the critical current of the used material. Niobium is a well suited material for the microfabrication of the meander shaped pick-up coil as the sputtered niobium structures, which have a critical temperature of $T_c = 9.3\,\mathrm{K}$, can carry a rather high critical current. The sputtering conditions are of great importantance since they have a susceptible influence on the film properties and in particular on the critical current. Additionally the substrate material and its lattice plane play an important role in defining the film properties. This section points out investigations on sputtered niobium films that were done within this thesis. A characterization of niobium structures, produced by varying different sputtering parameters, is presented. In particluar the residual resistivity ratio[1] (RRR) and the maximum critical current that sputtered niobium films can carry are discussed.

The meander structures are determined by their stripe width, which is $5\,\mu\mathrm{m}$ in the present design, and the niobium thickness, which is usually 400 nm. As already mentioned, the substrate, onto which the niobium is sputtered, influences the properties of the film. Therefore two different substrates, silicon and sapphire, have been used in the development of the meander shaped pick-up coils. Former MMC niobium structures sputtered on sapphire and silicon substrates showed a RRR of 3 to 4 and a maximum critical current of 120 mA. The sputtering conditions were an argon pressure of about $10^{-4}\,\mathrm{mbar}$, a controlled power of 100 W and the substrate was at a temperature of 17 °C.
Within this thesis new process parameters were utilized. The silicon substrate temperature was increased to 200 °C. In the first tests a power of 100W was used for the sputtering. The produced niobium structures showed a RRR of 1.4 and a critical current of 9.0 mA. Succeeding tests were done at a sputtering power of 500 W and showed better results. Different measurements showed the same RRR of 6.3 and critical current values between 180 mA and 255 mA. Corresponding to the meander stripe cross section, a persistent current of 250 mA refers to a current density of $9.3 \times 10^{10}\,\mathrm{A/m^2}$. A persistent current of this magnitude allows us to use the optimized current discussed in chapter 2.5.5.
Another important point achieved during this work was the increased yield of the detector chip production. The percentage of applicable chips rised from about 10 %

[1] The residual resistivity ratio is defined as the ratio of the resistivity at room temperature to the resistivity at 4.2 K.

to more than 50 %.

4.2 Persistent Current Switch

In chapter 3.3.1 the principle of injecting a persistent current was explained. In practice this is accomplished by a resistor that is deposited on top of the niobium meander bypass stripe. A crucial prerequisite is that the power dissipated by the current I_H running through the heater resistor should increase the temperature above $T_{c,Nb} = 9.3\,K$ in a very small region in order to interrupt the superconductivity only in the meander bypass stripe below. The performance of the heater depends on its resistance and on the thermal conductivity between the different chip layers and the substrate. An ideal material to be used for the heater thin film is a gold palladium alloy (AuPd). However, since the AuPd sputtering target was not available during the fabrication of the detector chip, a gold thin film was used. Even though gold has a rather small resistivity, it has the advantage of not being superconducting at low temperatures and it is inert, which means that the properties of the heater remain for a long time. By sputtering in an oxygen/argon atmosphere its specific resistance could be increased sufficiently.

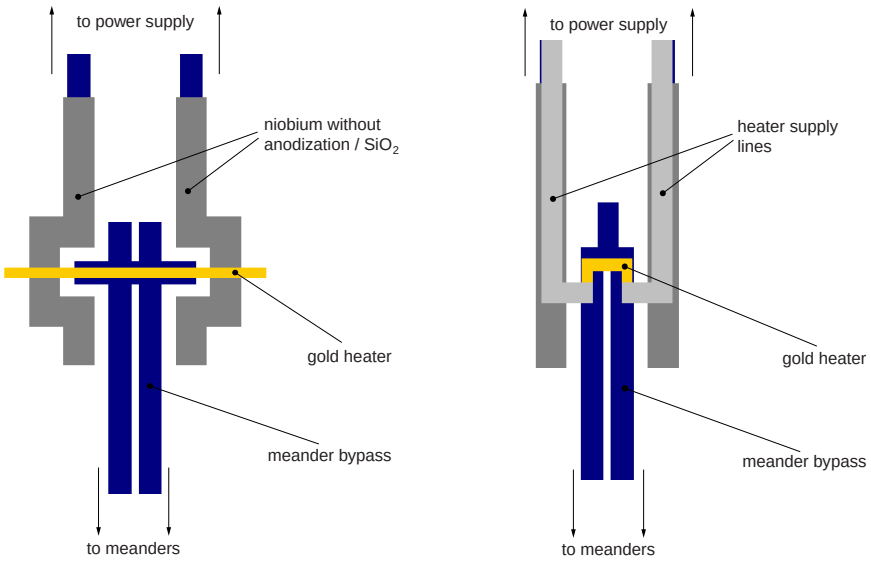

Figure 4.1 Different persistent current switch designs, done by the software program KIC [WHI05] **Left:** Top view of a former design. **Right:** Top view of the persistent current switch design developed during this work.

Figure 4.1 (left) shows a persistent current switch that was used in [KEM07]. The meander bypass stripe as well as the heater supply lines are within the first niobium layer. Both structures are covered by niobium oxide and SiO_2. Only two small areas, indicated by "niobium without anodization / SiO_2", of the heater supply lines do not have an insulating material above in order to have electrical contact with the heater resistor. The heater itself is a straight line lying above the two niobium

leads and the meander bypass stripe. Due to the fact that the heater thin film is sputtered after the meander fabrication, i.e. after the anodized niobium layer and the sputtered SiO_2, it is deposited over surfaces which have different relative heights. Therefore the heater is not a straight line from the side view, but has a rather wiggled shape. Regarding figure 4.1 (left) from left to right, the heater moves from the height of 400 nm of the connection area down to 300 nm of the pure silicon dioxide layer and crawls up to 700 nm of the meander bypass stripe which is covered by silicon dioxide. Therefore the thickness of the heater has to be such that it ensures a perfect connection over its whole length. One can imagine that a heater thin film with a thickness of, say, 50 nm would most likely be broken at the steps of the structures below. For that reason, the setup discussed in [KEM07] used a heater that consisted of 50 nm of copper and 250 nm of gold. In this case the resistance is expected to be 0.43 Ω for a constant cross section and a thickness of 5 μm at low temperatures. The measured resistance of this heater type was about 4 Ω. The explanation of this is the reduced cross section occuring when the heater film "climbs" over the niobium / SiO_2 structure below. Applying a heater current I_H, the highest power dissipation occurs at these regions. With this heater design, a current of more than 10 mA was necessary to interrupt the superconducting structure.

Figure 4.1 (right) shows the design of the persistent current switch that was developed within this work. The new design contains a heater that is exclusively structured on top of the meander bypass stripe and therefore with a constant cross section. With this condition it is principly possible to deposit arbitrary thin heater films. The heater has a U-shape in order to cover a large niobium surface. The connection to the supply lines is established by niobium stripes that are subsequently sputtered within the second niobium layer. From the lateral view one would see a wiggled shape of the new supply lines, but as they have a thickness of 400 nm, their cross section is not drastically reduced across the edges below. The big advantage of this design is that the heater thin film can be structured thinner, i.e. a bigger resistance can be achieved and the power dissipation is spread more locally compared to the former design.

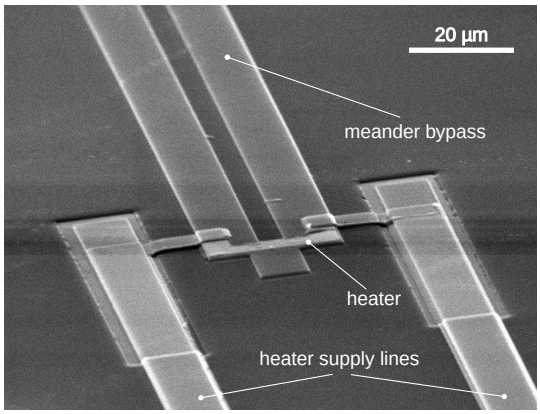

Figure 4.2 SEM-picture of the realization of the present persistent current switch design. The heater is sputtered on top of the meander bypass stripe. The supply lines are structured in the second niobium layer.

Figure 4.2 shows a SEM[2]-picture of the realization of the present persistent current switch design. One can recognize the mentioned wiggles occurring within the supply lines and the steps where they crawl up the meander bypass stripe to contact the heater which is barely visible in this picture. The heater is made of a 10 nm sticking layer of copper and 50 nm of gold. From an estimation the heater resistance is calculated to be 2.5 Ω at 4.2 K assuming bulk resistivities. A measurement of the heater resistance done at 4.2 K resulted in a value of 4.5 Ω. The higher value compared to the predicted one can be explained by considering the fact that sputtered films have more defects compared to bulk material.
The fact that the previous design has a heater resistance of the same resistance range is a coincidence, but this is due to the "bottle neck" effect occuring when the film climbs up a step. However, in that situation it was not possible to have reproducible values for the resistance. The present design allows to tune the resistance in a more reliable way due to the absense of steps. This persistent current switch design was successfully used in the framework of the experiments discussed in chapter 5. The current needed to interrupt the superconductivity in the meander bypass was 3.5 mA. With this persistent current switch currents up to 100 mA were injected into the meanders.

Outlook: New heat switch material

As mentioned above, a more suitable material for the heater thin film is the alloy AuPd (gold-palladium). As well as pure gold, it has a big stability against aging effects. Its advantage over gold is the higher resistivity of AuPd with a RRR close to unity. The resistance was measured with a meander shaped testing structure with a width of 200 μm and a total length of 1 m. It consisted of a sputtered 7.5 nm thick copper sticking layer and a 50 nm thick AuPd layer. The resistance of this structure was measured to be 34.9 kΩ. Scaled down to the size of the heater one obtains a corresponding value of 49 Ω for the heater resistance. AuPd is the new heater material that will be used in future magnetic microcalorimeter designs [PIE08].

4.3 Electroplating of Gold Absorbers

The requirements for an absorber of a metallic magnetic microcalorimeter are a small heat capacity at the working temperature, a good thermal conductivity and a good thermal contact to the sensor. Furthermore the absorber needs to provide a sufficiently high stopping power for the particles to be detected. The concentration of magnetic impurities inside the absorber volume needs to have a very small value in order not to compromise the magnetization signal from the sensor. Gold is an element with a high atomic number ($Z = 79$) and with one of the highest densities among other metals ($\rho_{\mathrm{Au}} = 19.3\,\mathrm{g/cm^3}$ [ASH07]). Generally, it has a good electrical conductivity and therefore a good thermal conductivity. Thus it is a well-suited absorber material for magnetic calorimeters.

[2]Scanning Electron Microscope

This section motivates and points out the method for electroplating thick gold absorbers suitable for the β-spectroscopy. Among the advantages of using this method is the possibility of growing films up to several hundred microns and to have high purity gold absorbers. In particular the high thickness is important to achieve a quantum efficiency close to unity for β-sources with endpoint energies up to 1 MeV.

4.3.1 Motivation

Electroplating offers a new and promising alternative for the absorber fabrication of metallic magnetic microcalorimeters. In [KIL05] the properties of electroplated gold absorbers, with a RRR up to 45, of transition edge sensors (TES) were described. A high RRR for the absorber is an advantage as it means a high thermal conductivity at low temperatures and therefore a fast thermalization.
Electroplating enables the deposition of several hundred microns of high purity gold. The deposition rate is about 600 nm/min, so a layer of 100 μm can be produced in about 3 hours which is fast compared to sputtering where the deposition time would be more than 17 hours. The electroplating process of MMC absorbers has been developed for the first time during this work and will be discussed in detail.

4.3.2 Electroplating of Gold

Electroplating of gold uses the principle of electrolysis which generally takes place inside an electrolyte that contains positively charged cations and negatively charged anions. After switching on the power supply, the electrical field between two electrodes, the positive anode and the negative cathode which are situated inside the electrolyte, forces the anions to move towards the anode and the cations towards the cathode. At the electrodes redox reactions take place. The cations are reduced at the cathode and the anions are oxidized at the anode. Gold ions inside an electrolyte are positively charged and therefore they move towards the cathode where they are deposited. The mass m that is deposited at the cathode is given by Farady's law:

$$m = \frac{ItM}{zF} \tag{4.1}$$

where I is the applied current, t is the electroplating time, $M = 196.97\,\mathrm{g/mol}$ is the molar mass of gold [KIT99], z is the oxidation state of the ions and $F = 96485\,\mathrm{C/mol}$ is the Faraday constant.

Figure 4.3 schematically shows the electroplating of gold. The gold cations are reduced at the cathode which is soon covered by a thin film of gold at all areas that are exposed to the electrolyte. As we are only interested in the electroplating process, anions are not depicted in this figure. For the electrodeposition in this work, a platinized titanium anode was used.

Nowadays there are basically two ways to electroplate gold. One can use cyanide-based electrolytes or sulfite-based electrolytes. In both kinds of solution the gold ions have the oxidation state of $z = +1$. Cyanide-based electrolytes have been already

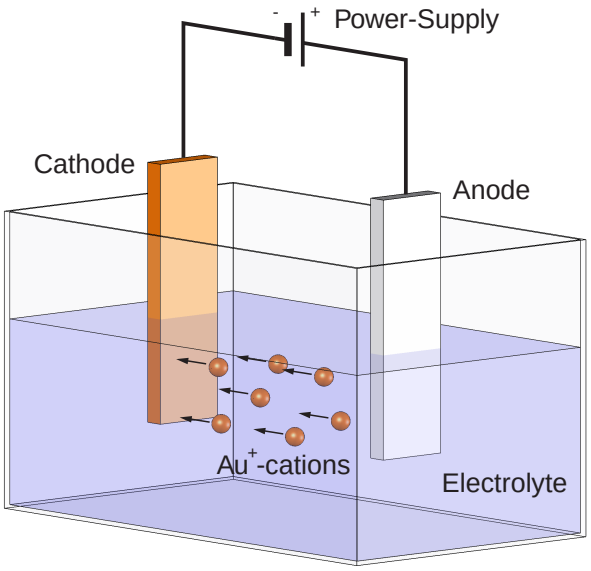

Figure 4.3 The electroplating of gold takes place inside an electrolyte that contains gold cations. Two electrodes are connected to a power supply and the electric field between the electrodes forces the gold cations to move towards the cathode where they are deposited.

available since the middle of the 19th century. With usual cyanide-based electrolytes one can produce gold films of up to 20 μm. Another disadvantage of this electrolyte type is that hydrogen porosities are attached to the gold films which, therefore, do not stick beyond a certain thickness [DAM07]. Sulfite-based electrolytes are, on the other hand, very recent products that have been increasingly used since the 1960s [BER04]. The performance of this gold electrolyte type was improved and nowadays one can use them to deposit several hundred microns of gold at a high purity. The gold electrolyte used in this thesis is a sulfite-based electrolyte[3] which can produce gold layers that have a purity of 4N (= 99.99 %) and a thickness of 300 μm.

4.3.3 Properties of Electroplated Gold

Before using the elctrolyte for the deposition of absorbers its properties were investigated. In particular it is very important that all the components, which need to be inside the electrolyte, are chemically stable against the basic solution. The first important test is to find out which seed layer can be used for the electroplating. For this one needs an appropriate seed layer which serves as a cathode. A testing structure was prepared in the following way. A 30 mm×30 mm×1 mm big glass plate was covered by a positive photoresist[4] and a meander shaped structure with a width of 200 μm and a total length of 1000 mm was structured lithographically. A gold seed layer was sputtered on top and the structure was obtained by a lift-off process.

As a first step seed layers, consisting of a 500 nm thick gold layer and a 50 nm thick copper sticking layer below, were used. Within a couple of minutes inside the gold electrolyte the sticking layer was dissolved by the electrolyte and the remaining gold structure came off the glass. In a second test an improved seed layer consisted

[3] AGC Micro Vision Bad, Wieland Dental Technology, Pforzheim, Germany
[4] AZ 5214E, distributed by MicroChemicals GmbH, Schillerstr. 18, 89077 Ulm, Germany

exclusively of a 500 nm thick gold layer that was sputtered inside an oxygen/argon atmosphere in order to improve the adhesion to glas compared to gold that is sputtered in a pure argon atmosphere. In a third test the seed layer consisted of an evaporated gold film.

Table 4.1 summarizes the results obtained with the different seed layers. The electrolyte temperature of 65 °C was controlled by a PT100 resistor. Within the electroplating tests, several currents were applied and the voltage drop between anode and cathode was measured. By using smaller current densities j we expected to see higher values of RRR, but this was not the case[5]. Also the usage of an evaporated film did not change the RRR very much. All gold films obtained with a direct current had RRR values between 3 and 4. Another possibility to improve the quality of gold films is to use a pulsed current at 1 kHz. With this technique, we could improve the RRR by a factor of 2. A succeeding tempering[6] enhances the RRR in the investigated cases. The calculated heights inside the table were determined by inserting the respective electroplating current and deposition time into equation (4.1).

sample no.	1	2	3	4	5
gold seed layer	sputtered	sputtered	sputtered	evaporated	sputtered
j [mA/mm^2]	0.05	0.05	0.025	0.05	0.025
electroplating current	10 mA, dc	10 mA, dc	5 mA, dc	10 mA, dc	5 mA, 1 kHz
voltage drop [V]	0.452	0.47	0.44	0.51	0.52
deposition time [h]	3	3	6	3	3
calculated height [μm]	50	50	50	25	5
measured height[μm]	-	-	30 - 50	-	0.5 - 12
RRR	3.65	3.25	3.74	2.94	6.23
RRR after 470 °C, 3 h	9.22	-	9.25	-	-

Table 4.1 This table shows parameters, that were used during multiple tests of electroplating, and the corresponding results.

In addition, the sample no. 2 was used to investigate the presence of magnetic impurities of the electroplated gold by using a magnetometer[7]. A measurement showed paramagnetic impurities of less than 1 ppm.

4.3.4 Absorber Deposition

The optimal 4π-absorber geometry for an isotropically emitting radioactive source would be a sphere which is of course not suitable for the case of magnetic micro-

[5] According to a remark of the gold electrolyte distributer, a lower current density should improve the quality of the deposited films.

[6] The method of tempering is inadequate for gold absorbers on top of Au:Er-sensors as the erbium should diffuse through the sensor/absorber-setup at higher temperatures which would decrease the signal size.

[7] Magnetic Property Measurement System MPMS XL, Quantum Design, 6325 Lusk Boulevard, San Diego, CA 92121-3733, USA

calorimeters since, for example, it would be difficult to couple it to the sensor. The chosen geometry is instead a cuboid which can be considered as consisting of two halves that are mechanically connected to each other. Once the first half of the absorber is prepared the very delicate step of positioning the radioactive source follows. This is done by drying a small drop of solution containing the isotope of interest in the center of the absorber surface. The final step is to cover the source with the second absorber half.

An idea to deposit the first gold absorber half is to use the conductive Au:Er-sensor as a cathode. As the detector chips are fabricated on top of 2"-wafers, which host more than 100 of those chips, all of the sensors need to be electrically connected by a grid which is in electrical contact to the negative pole of a power supply. In order to electroplate only the sensors, one has to protect all the other conductive structures by using an insulator. This can be accomplished by a photoresist, which can also be used to determine the shape of the absorber. In order to achieve an absorber thickness of several hundred microns one needs a photoresist which can be used to produce layers of the same thickness.

Another problem is to find a photoresist that is chemically stable against the basic sulfite-based gold electrolyte which has a pH-value of 8.5. The AZ photoresists usually used within the fabrication of MMCs were shown to be unstable against the electrolyte. In this case cyanide-based electrolytes would be more appropriate because the AZ photoresists are stable against their low pH-values. However, cyanide-based electrolytes do not fulfill the absorber demands. The negative photoresist SU-8 was found to be stable against the sulfite-based electrolyte. Furthermore it is capable to produce thick photoresist layers, see for example [NAT08]. The SU-8 used in this work is suited to produce photoresist layers of a thickness of 700 μm with a high aspect ratio[8], which is an advantage for the fabrication of thick absorbers. A more detailed description of the SU-8 relating to the MMC absorber fabrication is given in [PIE08].

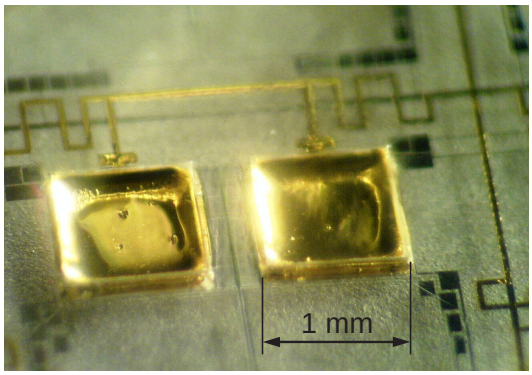

Figure 4.4 This picture shows electroplated gold absorbers on top of niobium meanders that were sputtered on sapphire. The absorbers are surrounded by the transparent SU-8 photoresist.

During this thesis a lithography process was developed to cover the 2"-wafer with SU-8 and to develop squared holes into the resist to provide moulds for the

[8]Several types of SU-8 exist. The used type is SU-8 100 which is comercially available at Micro Resist Technology GmbH, Köpenicker Str. 325, Berlin, Germany

gold absorbers. A wafer holder was constructed to fix the wafer and to contact it to the cathode of a power supply. A result of the electroplating process by using this wafer holder is shown in figure 4.4. The picture shows two electroplated absorbers on top of two connected sensors. They are encased by the transparent SU-8 photoresist. The bond pads of the first niobium layer can be seen as well. The substrate in this picture is a 2"-sapphire-wafer.

Removing the Photoresist

Even though SU-8 is an appropriate photoresist within the electroplating of MMC gold absorbers, it is very difficult to remove from the substrate. Several methods are recommended by the distributor, for example the usage of an additional separating photoresist or piranha etch[9]. This etching solution as well as the removal by chemical solvants or liquid nitrogen were tried within this thesis. The methods that actually remove the SU-8 have the disadvantage of removing the absorbers and other parts of the detector chips as well. Still this is a major problem within the production of thick gold absorbers by electroplating.

Due to a statement of the SU-8 distributor, plasma etching by the use of SF_6 recently showed the most promising result for the removal of SU-8. This method will be investigated for the fabrication of future MMCs.

4.3.5 Source Deposition

We approach the state of encasing a β-source from figure 4.4 where the first half of the absorbers is already electroplated. Contrary to this picture, only one sensor and one absorber were used for the detector discussed in this thesis. The deposition of the source leaves active salt crystals on top of the first absorber half that need to be protected against dissolving inside the electrolyte which can be done by sputtering. A shadow mask with lithographically produced holes inside is placed above the wafer and glued to the SU-8 surface by using GE 7031 Varnish. The aligning of these holes above the absorber areas is done inside a lithographic mask aligner. After the gluing, the wafer is moved into a sputtering machine and a 3 μm thick gold film is sputtered on top. Subsequently the mask is removed from the SU-8 surface and the second half of the absorber is electroplated onto the covered source. Finally the wafer is separated in single chips by using a wafer saw.

The MMC developed in this thesis was produced on top of a 2"-silicon-wafer and the deposition and covering of the sources were done as described above. After the sputtering the SU-8 came off the wafer, propably due to mechanical deformation during the sputtering, and ripped of all absorbers. For that reason we used a gold absorber that was fabricated from bulk material by hand.

The utilized absorber was produced by Martin Loidl and Thierry Branger at the Commissariat à l'Énergie Atomique (CEA) in Saclay, France. In a first step, two cylindrical disks of the same thickness are cut from a 6N-goldwire. To define the

[9] A mixture of varying ratios of H_2SO_4 and H_2O_2.

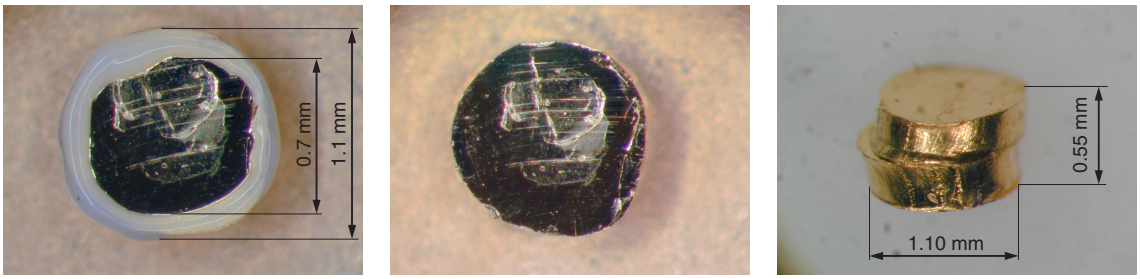

Figure 4.5 **Left:** The base area of one cylindric disk is covered by a ring of polysiloxane. Inside the ring one can see the whitish $^{63}NiCl_2$ crystals. **Middle:** The polysiloxane ring is removed. **Right:** The second cylindric disk is pressed to the first disk encasing the source and both cylinders are diffusion-welded.

β-emitting area, the face of one disk is coated by a ring of polysiloxane[10] which is shown in figure 4.5 (left).

Then a hydrochloric acid solution containing the enriched salt $^{63}NiCl_2$ is deposited into this ring. In order to minimize self-absorption of β-particles inside the source the size of the salt crystals has to be small which is accomplished by freeze-drying. The disk together with the solution drop is put into a vacuum chamber and cooled down to about -80°C to freeze the drop. Then the chamber is pumped down to a pressure of about 10^{-2} mbar and the solidified drop sublimates. Freeze-drying produces much smaller crystals than evaporation from the liquid state. After ripping off the epoxy, the $^{63}NiCl_2$ crystals cover an approximately circular area with a diameter of about 700 μm, as shown in the figure in the middle.

Afterwards the second disk is pressed to this surface and the resulting cylinder is diffusion welded at a temperature of 500 °C for 1 hour. The obtained 4π-absorber is shown in figure 4.5 (right). Subsequently the absorber is glued to the sensor by using EPO-TEK[11].

[10] CAF-4, Rhodia Usine Silicones, 69191 Saint-Fons, France

[11] EPO-TEK 301-2FL, Polytec PT GmbH Polymere Technologien, Polytec-Platz 1-7, 76337 Waldbronn, Germany

5. Experimental Results

5.1 Quantum Efficiency of the Detector

In the preceeding chapters we discussed the fabrication of the gold absorber, having a 4π-geometry, by the use of electroplating or, alternatively, by diffusion-welding and gluing. In this chapter the method to calculate the quantum efficiency for the gold absorber, that was used in the performed experiments, is discussed.

As an example, β-electrons with an energy of 1 MeV are stopped within a few microns inside the gold absorber [ROT07]. On the other hand, secondary particles like X-rays and bremstrahlung photons have a bigger attenuation length up to several millimeters in the energy range between 100 keV and 1 MeV. For this reason they can leave the absorber with high propability. This fact reduces the measured intensity in the high energy range of β-spectra and increases the intensity at lower energies because low energy electrons generate low energy secondary particles with a small attenuation length.

The well-suited software package PENELOPE performs FORTRAN based simulations for electron, positron and photon transport processes over an energy range from 50 eV to 1 GeV [SAL06]. Its subroutine PENCYL treats detector designs with a cylindrical shape that can consist of different materials. For a cuboid absorber geometry the determination of the quantum efficiency is barely modified by the assumption of a cylindrical absorber with the same height and a diameter that equals the side length of the cuboid.

Figure 5.1 (left) shows the geometry studied with the performed simulation. The source is described as a small cylinder positioned on a plane perpendicular to the cylinder axis encased by the two absorber halves. The absorber has a height of 400 μm and a diameter of 1000 μm. The source has a height of 1 μm and a diameter of 600 μm.

Since the detector is designed for the measurement of β-spectra up to 1 MeV, this simulation was performed in order to evaluate the discrepancy between the measured spectrum and the real emitted spectrum. Therefore the distributed source was set to isotropically emit monoenergetic electrons with an energy of 1 MeV. Figure 5.1 (right) shows the result of a PENCYL simulation with 3.4×10^5 primary electrons. The logarithmic plot displays the deposited energy inside the absorber. As mentioned above, 1 MeV electrons are stopped within a few microns of gold, i.e. no electron leaves the considered absorber. The fact that the result shows a continuous spectrum below 1 MeV describes the loss of energy due to escaping secondary particles. The quantum efficiency can be described as the ratio of the area under the 1 MeV-peak and the total integral of the diagram. From this we calculate the quantum efficiency to be 85 %. A quantum efficiency smaller than unity affects the shape of the spectrum. As described in [ROT07], where the quantum efficiency was 93 % for the 710 keV endpoint electrons of the β-isotope ^{36}Cl, it is possible to calculate a correction factor

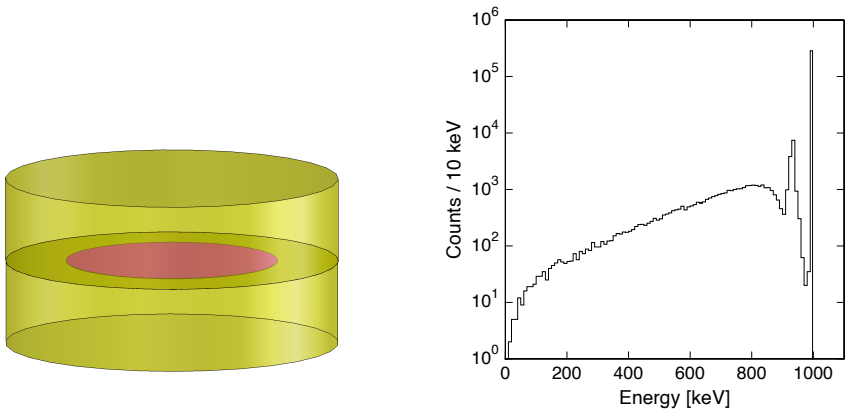

Figure 5.1 **Left:** The simulation uses an idealized absorber with a height of 400 μm and a diameter of 1000 μm. The source is just in the center of this cylinder and has a height of 1 μm and a diameter of 600 μm. **Right:** Result of a PENCYL simulation with 3.4×10^5 primary monoenergetic electrons with an energy of 1 MeV. The quantum efficiency is the ratio between the number of 1 MeV β-electrons and the total number of absorbed electrons.

with the help of the Monte Carlo simulation.

It is intuitively clear, that with the same absorber a higher quantum efficiency is achieved for lower energies. At 500 keV we find an efficiency of 96 % and at 67 keV, i.e. the endpoint energy of ^{63}Ni, we find a quantum efficiency of 99.996 %. This result can be applied to the actual utilized absorber geometry which is a cylinder with a height of 550 μm and a diameter of 1100 μm with a source diameter of approximately 700 μm. Since the dimensions are larger than in the simulated case this leads to a quantum efficiency that is slightly higher.

5.2 Magnetization of the Sensor

A particle hitting the absorber leads to a temperature change inside absorber and sensor. The resulting flux change in the detector SQUID depends on the magnetization change $\partial M/\partial T$ of the sensor. Therefore the measurement of the magnetization M as a function of temperature T is a crucial point to describe the detector performance and will be discussed in the following.

The actual measured quantity is the magnetic flux $\Phi_S(\overline{B},T)$ in the detector SQUID, where $\overline{B}$ is the mean magnetic field in the sensor, which is proportional the persistent current I_F injected into the meander shaped pick-up coil. The measurements were done by slowly decreasing the temperature of the experimental platform from about 300 mK down to 25 mK. The output voltage of the FLL-electronics as well as the temperature of the experimental platform were recorded[1].

Figure 5.2 shows two magnetization curves obtained for two persistent currents

[1] The output voltage of the FLL-electronics was digitized by the use of a Keithley 195A digital multimeter.

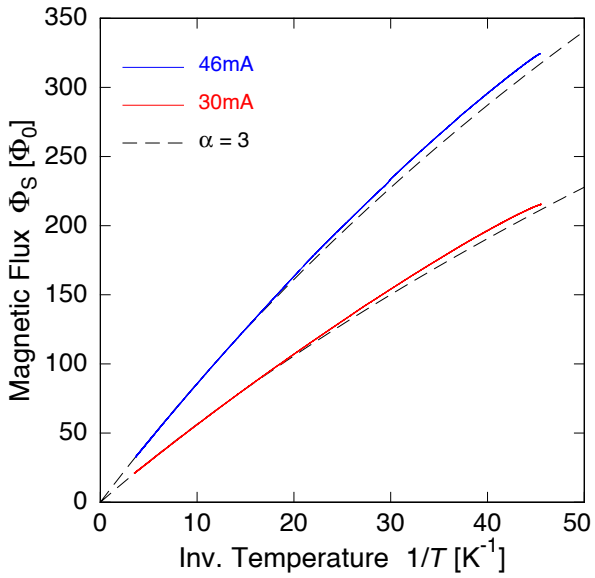

Figure 5.2 This plot shows magnetization curves for persistant currents of $I_F = 30\,mA$ and $I_F = 46\,mA$. The experimental data (solid curves) fit well to the simulated curves for $\alpha = 3$ (dashed curves) down to a temperature of 60 mK.

$I_F = 30\,mA$ and $I_F = 46\,mA$ which correspond to mean magnetic fields of $\overline{B} = 1.7\,mT$ and $\overline{B} = 2.6\,mT$, respectively. The dashed lines are determined by numerical calculations which take into account the detector geometry, the properties of the Au:Er film and the coupling to the SQUID. The erbium concentration of this sensor is assumed to be 775 ppm [KEM07]. The Au:Er sputtering target was produced by the use of natural erbium which contains 22.9 % of the erbium isotope ^{167}Er that has a nuclear magnetic moment of $I = 7/2$. The ^{167}Er ions contribute with an additional hyperfine splitting.

In chapter 2.3.2 it was shown that an interaction parameter $\alpha = 5$ fits well to experimental data for bulk Au:Er, but this is not necessarily true for sputtered Au:Er-films. A sputtered film consists of polycrystalline material with grain boundaries where the erbium ions cannot replace gold atoms on regular lattice sites, like it was considered in chapter 2.3.1. In the present measurements we see that the obtained data fit better to the numerically calculated curves with $\alpha = 3$, which means a smaller RKKY-interaction relating to the dipole-dipole interaction.

One important parameter which cannot be estimated very well is the inductance L_W of the aluminum bond wires between the meanders and the input coil of the detector SQUID. For the simulated curves, we assume the inductance to be $L_W = 4.9\,nH$.

Coming from high temperatures, i.e. low values of T^{-1}, both the measured curve for $I_F = 30\,mA$ and the one for $I_F = 46\,mA$ fit well to the theoretical curves down to a temperature of about 60 mK. The fact that the slope of the measured curves increases towards lower temperatures compared to the theoretical prediction might be due to reduced interactions of the spins caused by structural defects in the sputtered film. The interaction in between the ^{167}Er-ions and their interaction to erbium ions without nuclear spin were neglected for the numerically calculated

curves, which might be another reason for the deviation.

Earlier magnetization measurements of sputtered Au:Er-sensors fitted to the theoretical curves in the temperature range above 45 mK [KEM07]. Below, the measured curves showed a smaller slope which was found to be due to the small thermal conductivity between experimental platform and sensor which therefore stayed warmer. Therefore, a possible deviation from the value of $\alpha = 5$ could not have been observed.

5.3 Analysis of the Detector Signal

5.3.1 Signal Shape Analysis

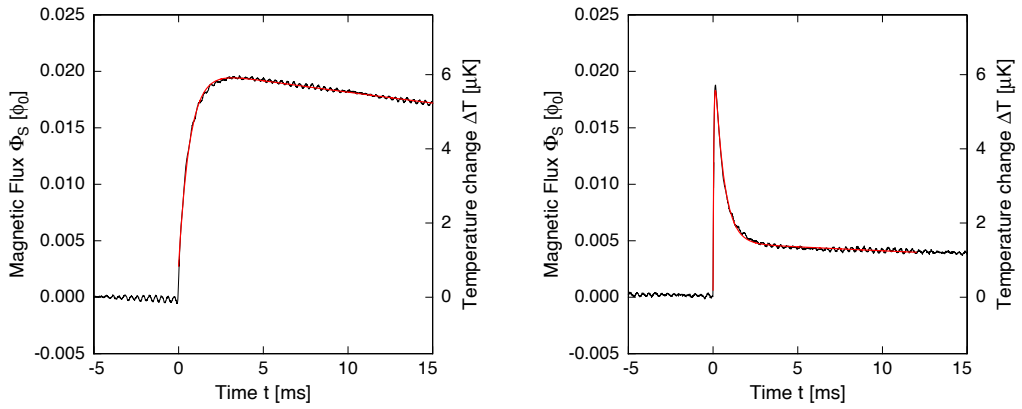

Figure 5.3 This figure shows the two different pulse types that were observed with the detector. The left axis of each plot denotes the magnetic flux change inside the detector SQUID and the right axis denotes the temperature change ΔT of the sensor. **Left:** The slow pulse has a characteristic rise time of 0.67 ms and a decay time of 90 ms. **Right:** The fast pulse type has a rise time of 49 μs, a fast decay time of 0.53 ms and a slow decay time of 61 ms.

Figure 5.3 shows two different signal shapes that were observed within the conducted experiments. These pulses were recorded at a temperature of $T = 46$ mK and a persistent current of $I_F = 46$ mA within a time window size of 20 ms. The data acquisition was done with a low pass filter of 3 kHz, but no high pass filtering. The periodic noise, which is superimposed to both pulses, has a frequency of 2.7 kHz. The presence of this noise might be due to a resonant vibrational mode of the continuously filled 1K-pot of the dilution refrigerator or due to external electromagnetic noise that couples into the experiment through supplying lines.

The signal shown in the left figure was obtained by averaging several pulses with the same amplitude. It is fitted by the sum of two exponentials,

$$\Phi_S(t) = -a_0 e^{-t/\tau_0} + a_1 e^{-t/\tau_1}, \tag{5.1}$$

where a_0 and τ_0 are the parameters describing the rise, and a_1 and τ_1 the decay of

the signal. The resulting time constants are $\tau_0 = 0.67\,\text{ms}$ for the rise and $\tau_1 = 90\,\text{ms}$ for the decay.

The right signal in figure 5.3 has a rise time that is much faster. This signal type will therefore be denoted as "fast pulse" and the one discussed before as "slow pulse". The shape of the fast pulse is fitted using the function

$$\Phi_S(t) = -a_0 e^{-t/\tau_0} + a_1 e^{-t/\tau_1} + a_2 e^{-t/\tau_2}. \tag{5.2}$$

The time constants extracted by the fitting are $\tau_0 = 49\,\mu\text{s}$ for the rise, $\tau_1 = 0.53\,\text{ms}$ for the fast decay and $\tau_2 = 61\,\text{ms}$ for the slow decay. The rise time τ_0 is limited by the low pass filter. The frequency of 3 kHz corresponds to a maximum observable time of $(2\pi \times 3\,\text{kHz})^{-1} = 53\,\mu\text{s}$. This value is consistent with the fitting parameter τ_0.

The underlying data set can be displayed in a diagram of the least squares deviation (χ^2) of the signals, relating to a signal template, versus the signal amplitudes.

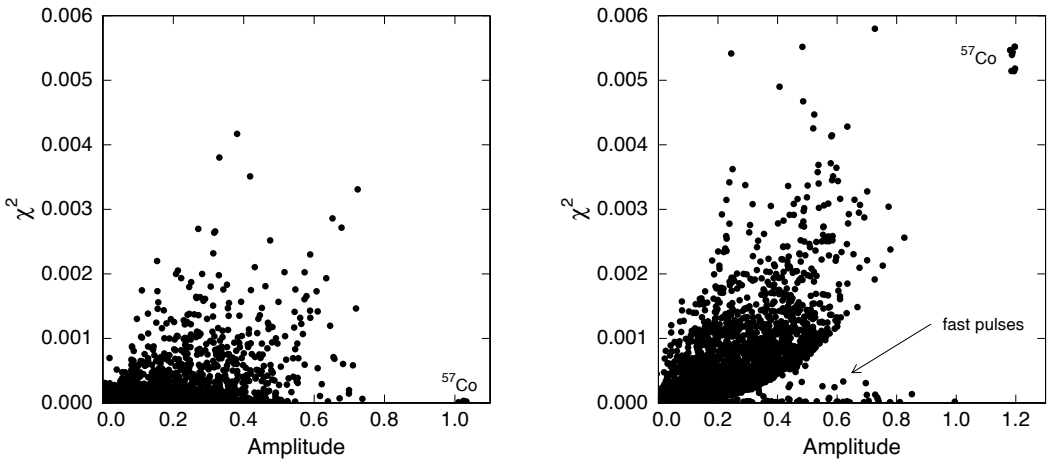

Figure 5.4 The current data set is plotted as diagrams with the χ^2 of the signals versus their amplitudes. **Left:** A slow 122 keV-pulse of ^{57}Co was chosen as template. Therefore the 122 keV-line can be observed at the amplitude 1.0. **Right:** χ^2-plot with a fast pulse as template. The fast pulses are close to the x-axis and the slow pulses bend away parabolically.

The plot from figure 5.4 (left) was obtained by choosing a slow pulse that belongs to the 122 keV-line of ^{57}Co as signal template. Hence, the corresponding pulses are situated at the amplitude 1.0 and have a very small χ^2.

In a second step a fast pulse was used as template and the plot shown in figure 5.4 (right) was obtained. The slow pulses now have a bigger χ^2 and bend away from the x-axis parabolically. The slow 122 keV-pulses of ^{57}Co moved to the right upper corner of the plot. The fast pulses are situated close to the x-axis with a continuous amplitude distribution. No discrete lines are observed and therefore an energy calibration is not possible for this kind of events.

The two different signal shapes can be explained by the following detector model which is similar to the sensor model shown in chapter 2.4. Figure 5.5 describes the

detector as consisting of the two thermal systems of the absorber and the sensor with the respective heat capacities C_a and C_s.

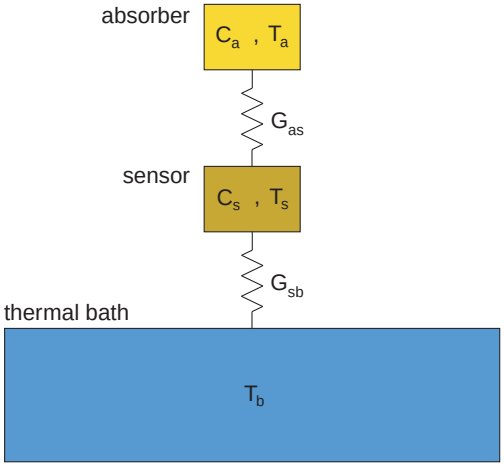

Figure 5.5 Model of the detector. The absorber with heat capacity C_a and temperature T_a is coupled to the sensor via the thermal link G_{as}. The sensor with heat capacity C_s and temperature T_s is coupled to the thermal bath via G_{sb}. The thermal bath is at the temperature T_b.

The absorber is coupled to the sensor via the thermal link G_{as} and the sensor is coupled to the thermal bath via G_{sb}. In chapter 2.4.1 we saw that the thermalization time between the Zeeman system and the electronic system of the Au:Er-sensor is described by the Korringa relation with a resulting relaxation time of 0.14 μs at a temperature of 50 mK. As this characteristic time is two orders of magnitude smaller than the rise times of the signals discussed here, we consider the sensor as a single system. The set of differential equations that describes the present system, can be written as

$$C_a \dot{T_a} = -G_{as}(T_a - T_s) \tag{5.3}$$

and

$$C_s \dot{T_s} = G_{as}(T_a - T_s) - G_{sb}(T_s - T_b), \tag{5.4}$$

where T_a, T_s and T_b are the temperatures of the absorber, sensor and thermal bath, respectively. A solution for the temperature change $\Delta T = T_s - T_b$ of the sensor is given in [STE98]. We consider two different cases of energy deposition into the system. One is the deposition into the absorber and the other one the deposition into the sensor. The temperature change ΔT in the sensor depends on where the energy is deposited in the detector. If a particle hits the absorber, ΔT is given by

$$\Delta T = f \frac{E}{C_a} \left(e^{-t/\tau_a} - e^{-t/\tau_b} \right), \tag{5.5}$$

and, if the sensor is hit, the corresponding relation is

$$\Delta T = \frac{E}{C_s} \left((1-g)\, e^{-t/\tau_a} + g\, e^{-t/\tau_b} \right), \tag{5.6}$$

where τ_a, τ_b, f and g are functions of C_a, C_s, G_as and G_sb which are given by [STE98]

$$\tau_{a,b} = 2\left[\left(\frac{G_\mathrm{as}}{C_\mathrm{a}} + \frac{G_\mathrm{as}+G_\mathrm{sb}}{C_\mathrm{s}}\right) \pm \sqrt{\left(\frac{G_\mathrm{as}}{C_\mathrm{a}} + \frac{G_\mathrm{as}+G_\mathrm{sb}}{C_\mathrm{s}}\right)^2 - 4\frac{G_\mathrm{as}G_\mathrm{sb}}{C_\mathrm{a}C_\mathrm{s}}}\right]^{-1}, \tag{5.7}$$

$$f = \frac{\tau_a\tau_b}{\tau_a-\tau_b}\frac{G_\mathrm{as}}{C_\mathrm{s}}, \tag{5.8}$$

and

$$g = \frac{\tau_a\tau_b}{\tau_a-\tau_b}\left(\frac{1}{\tau_b} - \frac{G_\mathrm{as}}{C_\mathrm{a}}\right). \tag{5.9}$$

Equation (5.5) corresponds to equation (5.1) and the characteristic time τ_b corresponds to the rise time τ_0 as well as τ_a can be identified by the decay time τ_1. Equation (5.6) can be compared to equation (5.2) without considering its fast rise time τ_0 which is physically determined by the Korringa constant mentioned above and technically limited by the 3 kHz low pass filter. In this case τ_b corresponds to the fast decay time τ_1 and τ_a corresponds to the slow decay time τ_2.

Fitting the pulse types once more with the two expressions (5.5) and (5.6), we obtain the parameters given in table 5.1.

	C_a [nJ/K]	C_s [nJ/K]	G_as [nW/K]	G_sb [nW/K]
slow pulse	1.79	0.536	627	25.9
fast pulse	1.70	0.578	750	22.6

Table 5.1 This table shows parameters that were obtained by fitting the pulses with the equations (5.5) and (5.6).

From this table one recognizes that the parameters obtained from the fits of both pulses are consistent. This argues for the validity of the utilized model.

As mentioned in chapter 3.3.2 a thermalization stripe is attached to the sensor. This was dimensioned in order to obtain a pulse decay time in the order of 1 ms. The stripe is connected by three gold bond wires to the thermal bath which should lead to a thermal conductivity G_sb that is about 60 times bigger than the value in the table. During the gold wire connection, the stripe came off the chip, but stayed connected to the sensor. This might have decreased the thermal conductivity to the bath due to a reduced cross section of the thermalization stripe. A consequence of this is the increased the pulse decay time.

Assuming a perfect cylindrical absorber geometry we obtain a heat capacity of $C_\mathrm{a,cyl} = 2.2\,\mathrm{nJ/K}$ at a temperature of 46 mK which is consistent with the value from the table, $C_\mathrm{a} = 1.8\,\mathrm{nJ/K}$, if we allow for the real absorber shape. Since the shape of the sensor is well defined, we expect to find a better consistency to its heat capacity $C_\mathrm{s} = 0.55\,\mathrm{nJ/K}$ which is given in the table. Actually the calculated sensor heat capacity is $C_\mathrm{s,calc} = 0.27\,\mathrm{nJ/K}$. Such a deviation was already observed for the case of

sputtered Au:Er-sensors [KEM07]. As in the discussion of the magnetization curves, this deviation might be due to the neglected interactions of ^{167}Er or to the presence of morphological defects.

We summarize the behavior of the two pulse types in the following descriptive way. A slow pulse is generated by a particle that hits the absorber. The temperature T_a changes and the thermal equilibrium to the sensor is established via the relatively large thermal conductivity G_{as}. The equilibrium to the thermal bath is established via the small thermal conductivity G_{sb}. In the present case of a detector setup with $G_{as} \gg G_{sb}$, the rise time of a slow pulse is determined by G_{as} and its decay time by G_{sb}. For the case of a sensor hit, which generates a fast pulse, the temperature rises inside the sensor according to the Korringa relation. The thermal equilibrium to the absorber is established via G_{as} which causes the fast decay time. The equilibrium to the thermal bath is established via G_{sb} which causes the slow decay time.

For that reason the rise time of the slow pulse corresponds to the fast decay time of the fast pulse and the decay time of the slow pulse corresponds to the slow decay time of the fast pulse. This can as well be seen by the fitting parameters of the equations (5.1) and (5.2) discussed above.

Finally we take a look at the origin of the fast pulse types that are caused by sensor hits. Possible candidates are the internal ^{63}Ni-source or the external ^{57}Co-source. From the distance between ^{57}Co-source and gold absorber, the source activity and the collimator hole diameter we estimate a particle rate of $3\times10^{-3}\,\mathrm{s}^{-1}$ inside the sensor. For the estimation of the sensor particle rate generated by the ^{63}Ni-source, we use the corresponding quantum efficiency and the source activity and obtain a rate of $0.05\times10^{-3}\,\mathrm{s}^{-1}$. Therefore the ^{57}Co-source should be the only origin of the fast pulses.

5.3.2 Signal Height Analysis

As we saw in chapter 2.5.3 the signal size of a metallic magnetic microcalorimeter does not only depend on the magnetization slope $\partial M/\partial T$ of the sensor, but also on the heat capacities of sensor and absorber. In the following we discuss the signal size per unit energy $\delta\Phi_S/\delta E$ with $\delta\Phi_S$ being the flux change in the detector SQUID and δE the energy of the absorbed particle.

Figure 5.6 shows $\delta\Phi_S/\delta E$ as a function of temperature for the two different field currents $I_F = 25\,\mathrm{mA}$ and $I_F = 46\,\mathrm{mA}$. The solid lines are numerically calculated curves for the respective field currents. The calculation contains the temperature dependent heat capacities of sensor and absorber as well as the temperature dependence of the magnetization. Like the magnetization curves in section 5.2, the curves are calculated taking into account the hyperfine splitting of the ^{167}Er-ions. However, the interactions in between those ions as well as their interaction to the other erbium ions without nuclear spin are not considered.

The circles and triangles are measured signal heights $\delta\Phi_S$ normalized to 1 keV. The deviations from the numerically calculated curves vary by factors from 1.8 at higher temperatures to 3.4 at 25 mK. A possible explanation could be the deviation of

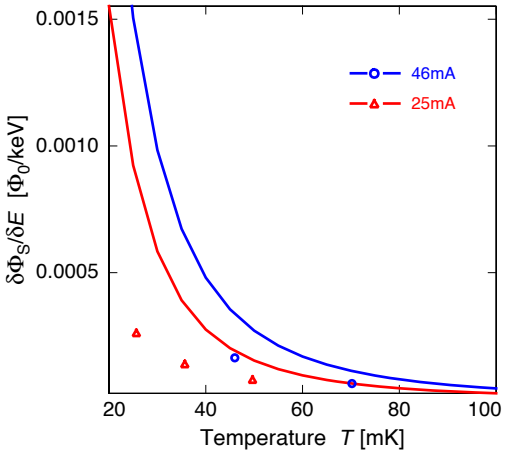

Figure 5.6 The signal size per unit energy $\delta\Phi_S/\delta E$ as a function of temperature for the field currents $I_F = 25\,\mathrm{mA}$ and $I_F = 46\,\mathrm{mA}$.

the sensor heat capacity, determined within the pulse shape analysis in the preceeding section. Deviations from theory were already observed in earlier works [KEM07], but only in the range of 30 %. A part of the present deviation can be explained by the neglected interactions of the ^{167}Er-ions, which enhance the heat capacity of the sensor and therefore reduce the signal size.

5.4 Measured β-Spectrum of ^{63}Ni

5.4.1 Comparison with Theoretical Calculations

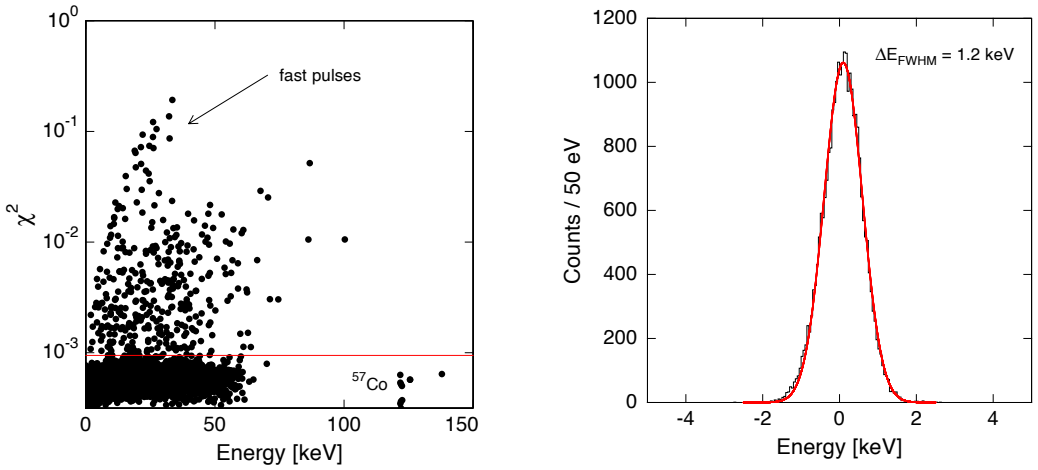

Figure 5.7 **Left:** χ^2-plot of the measured spectrum. In the top left-hand corner of the diagram the fast pulses are located. At 122 keV one can recognize the dominant line of the ^{57}Co calibration source. The horizontal line at $\chi^2_{\mathrm{rej}} = 0.00095$ displays the χ^2-criterium discussed in the text. **Right:** Gaussian fit of the baseline. The full width at half maximum has a value of $\Delta E_{\mathrm{FWHM}} = 1.2\,\mathrm{keV}$.

In the following we discuss a spectrum that was obtained with a field current of $I_F = 25\,\text{mA}$ at a controlled temperature of $T = 25\,\text{mK}$. The spectrum without pulse rejection contains 160,000 counts and was recorded with a low-pass filter of 30 kHz and a high-pass filter of 3 Hz. The energy axis was calibrated by the use of the ^{57}Co-line at 122 keV.

Figure 5.7 (left) shows a logarithmic χ^2-plot of the measured pulses against the corresponding particle energy which was obtained by using the rise time of a slow pulse as a template. This is done in order to discriminate the fast pulses discussed before. Inside the plot, these pulses can be found in the ascending branch of very high values of χ^2.

In order to minimize the influence of pileup events we have to find a χ^2-criterium. Looking at the pulse distribution we chose a χ^2-rejection level of $\chi^2_{\text{rej}} = 0.00095$ which we mark by a horizontal line in the χ^2-plot.

First we take a look at the baseline spectrum obtained by using the above χ^2-criterium. Figure 5.7 (right) shows a gaussian fit to the baseline of the discussed data set. The full width half maximum value of this fit is $\Delta E_{\text{FWHM}} = 1.2\,\text{keV}$. This roughly agrees with the line width of the 122 keV calibration line, which can only be estimated with quite some uncertainty due to the small number of counts in this line. Because of this, the calibration line is not displayed within this discussion. The energy resolution in this spectrum is about 20 times worse than the design value. On the one hand this is due to the field current $I_F = 25\,\text{mA}$ used in the present measurement which is roughly 4 times smaller than the optimum current, leading to a signal size that is reduced by roughly the same factor. On the other hand the high count rate in combination with the long signal decay time causes effectively a very non-steady noisy signal baseline.

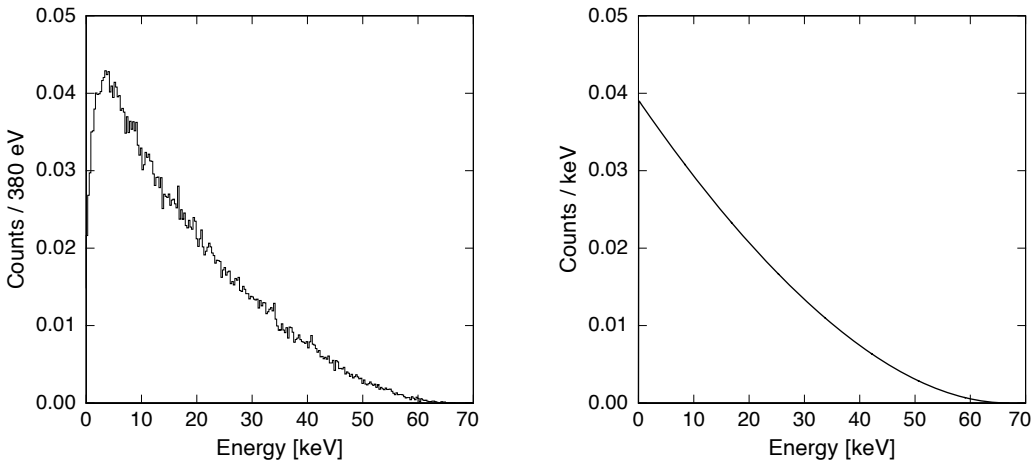

Figure 5.8 **Left:** Measured β-spectrum of ^{63}Ni. The corresponding χ^2-plot and the rejection level were shown in figure 5.7 (left). **Right:** Theoretical β-spectrum of ^{63}Ni like it was described in chapter 2.1. The Fermi function as well as the screening effect are included. The exchange effect is not shown in this diagram.

In a second step we generate a histogram of the pulses which is shown in figure 5.8 (left). The trigger level for this spectrum was set to a corresponding energy of 1.5 keV. For comparison the theoretical curve from figure 2.3 which contains the Coulomb correction and the screening effect is depicted in figure 5.8 (right).

The measured curve has a maximum at an energy of 3.5 keV. Above 20 keV it follows the general shape of theoretical spectrum. The range between 1.5 keV and 20 keV deviates significantly from the theoretical spectrum. The highest deviation can be found at the maximum of the measured curve where the intensity is 20 % higher than in the case of the theoretical curve.

A possible explanation can be found in considering the so-called exchange process. The β-decay of a many-electron atom to a given final atomic state, in which an electron is in a continuum orbital, can be achieved within the *direct process* as well as in the *exchange process*. The *direct process* is the creation of a β-electron in the continuum orbital whereas the *exchange process* is the creation into a bound orbital with an electron simultaneously making a transition to a continuum orbital of the daughter atom. In [HAR92] it was found that the combination of the two processes leads to an enhancement of the spectrum at low energies. In [ANG98] measurements with a cryogenic calorimeter with a 4π-geometry yielded quantitative evidence for the exchange effect in the case of ^{63}Ni. The enhancement of the spectrum was calculated to be about 2 % at 20 keV and 6 % at 6 keV in comparison to the theoretical spectrum which only includes the Coulomb correction. Looking at the 20 %-deviation at 3.5 keV, these percentages can only explain a small part of the deviation.

Most likely the low energy deviation is an artefact of the experimental conditions. Especially the activity of 25 Bq was too high according to the time scale of the pulse formation. This leads to a large amount of pileup events which, together with the dead time of the detector, contribute to the modification of the spectral shape.

5.4.2 Kurie Plot and Endpoint Energy

In order to estimate the endpoint energy of the measured β-spectrum we generate its Kurie plot which is shown in figure 5.9. A line is fitted in the energy range from 40 keV to 67 keV. The intersection of this line with the x-axis including its uncertainty results in a value of (67.0 ± 1.2) keV. This value is consistent with the endpoint energy of (66.946 ± 0.020) keV determined in [HET87].

5.5 Noise Analysis

As pointed out in chapter 2.4, there are basically three noise sources that affect the energy resolution of a metallic magnetic microcalorimeter: the thermodynamical fluctuations of the energy in the detector, the magnetic Johnson noise of metallic components of the detector and the magnetic flux noise of the two-stage SQUID setup. The latter contribution contains the intrinsic noise of detector and amplifier SQUID, the noise of the gain resistor R_g and the noise of the FLL-electronics at

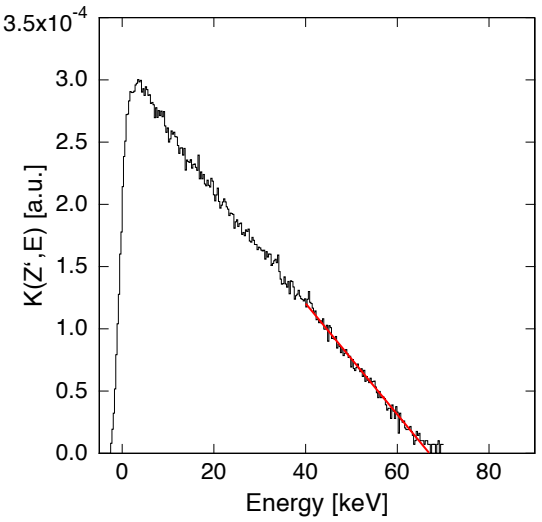

Figure 5.9 Kurie plot of the measured β-spectrum shown in figure 5.8 (left). A linear fit in the energy range from 40 keV to 67 keV leads to an endpoint energy of (67.0 ± 1.2) keV.

room temperature.

The measured noise spectra are obtained by measuring the output voltage of the two-stage SQUID setup in FLL mode with a spectrum analyzer[2] in the frequency range up to 100 kHz.

5.5.1 Detector Noise at 4.2 K

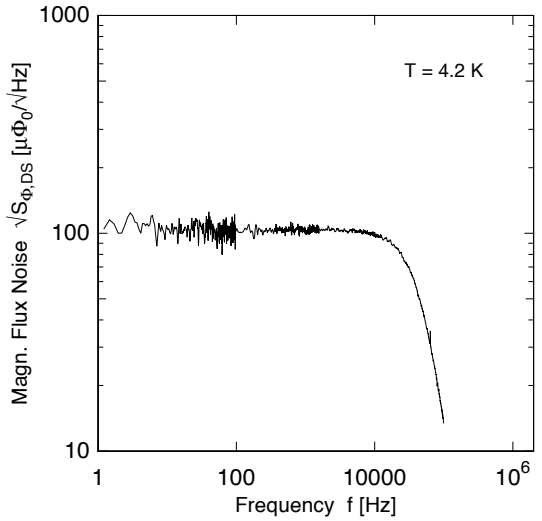

Figure 5.10 The magnetic flux noise spectrum of the detector SQUID at a temperature of 4.2 K. The plateau has a white noise level of $102\,\mu\Phi_0/\sqrt{\text{Hz}}$. The cut-off frequency has a value of 30 kHz.

Figure 5.10 shows a noise spectrum of the magnetic flux in the detector SQUID at a temperature of 4.2 K. One can clearly recognize a plateau with a white noise level of $102\,\mu\Phi_0/\sqrt{\text{Hz}}$ up to a frequency of about 10 kHz, followed by a low pass characteristic with a cut-off frequency of about 30 kHz. As we will see in the following discussion

[2] SR760 FFT Spectrum Analyzer, Stanford Research Systems

the high value of the white noise level as well as the low pass characteristic is due to the normal conducting aluminum bond wires that connect the meander shaped pick-up coil to the input coil of the detector SQUID.

The intrinsic noise of the detector SQUID is $1.34\,\mu\Phi_0/\sqrt{\text{Hz}}$ at a temperature of 4.2 K while the one of the amplifier SQUID was measured to be $0.6\,\mu\Phi_0/\sqrt{\text{Hz}}$. As pointed out in chapter 3.2.3 the flux-to-flux coefficient[3] is measured to be $G_\Phi = 0.6$. Therefore the amplifier SQUID noise contributes with $1.0\,\mu\Phi_0/\sqrt{\text{Hz}}$ to the noise of the detector SQUID. As mentioned in chapter 3.2.2 the noise of the room temperature FLL-electronics is $0.33\,\text{nV}/\sqrt{\text{Hz}}$ in a frequency range up to 10 MHz. With a voltage-to-flux coefficient of $V_\Phi = 990\,\mu\text{V}/\Phi_0$ the electronics contributes with $0.33\,\mu\Phi_0/\sqrt{\text{Hz}}$ to the apparent noise of the detector SQUID.

Another noise contribution is given by the current noise of the gain resistor R_g which can be calculated by using the fluctuation dissipation theorem, $S_\text{I} = 4k_\text{B}T/R_\text{g}$. This current noise couples into the amplifier SQUID via the mutual inductance $M_\text{is,AS}$ and subsequently into the detector SQUID via G_Φ. With $R_\text{g} = 0.27\,\Omega$ and $M^{-1}_\text{is,AS} = 17.5\,\mu\text{A}/\Phi_0$ we obtain a noise contribution of $2.79\,\mu\Phi_0/\sqrt{\text{Hz}}$.

The magnetic Johnson noise can be calculated by using equation (2.28) given in chapter 2.4.2. The contribution of the sensor is calculated assuming bulk Au:Er and the corresponding magnetic flux noise inside the meanders is $81\,\mu\Phi_0/\sqrt{\text{Hz}}$. In order to estimate the contribution of the gold absorber, we assume a RRR of 500 and obtain a value of $380\,\mu\Phi_0/\sqrt{\text{Hz}}$ inside the meanders. To calculate the magnetic Johnson noise of sensor and absorber in the detector SQUID, we have to multiply both values with the coupling factor 0.012 between the meander shaped pick-up coil and the detector SQUID. The resulting noise contributions are $0.96\,\mu\Phi_0/\sqrt{\text{Hz}}$ for the sensor and $4.4\,\mu\Phi_0/\sqrt{\text{Hz}}$ for the absorber.

As the detector chip is glued on top of a brass holder, we also consider this contribution to the magnetic Johnson noise. As mentioned in chapter 3.3.2, the arrangement of the meander shaped pick-up coil is such that the influence of the magnetic Johnson noise is minimized. Still there are areas of the meander that are not within this gradiometric arrangement and therefore contribute to the magnetic Johnson noise. These areas are estimated to have about 5 % of the meander area. We assume this area to be within a loop of a certain radius R. The distance between the pick-up coil and the brass holder is roughly $350\,\mu$m and its thickness is 1.5 mm. According to [FLE03] we calculate a value of $2.34\,\mu\Phi_0/\sqrt{\text{Hz}}$. Using the coupling constant between SQUID and meander this converts to a noise contribution of $0.03\,\mu\Phi_0/\sqrt{\text{Hz}}$ in the detector SQUID.

The noise of the normal conducting aluminum bond wires, that connect the meanders with the detector SQUID, should be high compared to other contributions as their resistance is small at a temperature of 4.2 K. The electrical conductivity of bulk aluminum at room temperature has a value of $3.77 \times 10^6\,(\Omega\text{m})^{-1}$ [KIT99]. For the aluminum bond wires with a total length of 2.6 mm and a diameter of 25μm this

[3]The positive slope of the detector SQUID was found to have a larger noise. Therefore the working point of the two stage setup was set to the negative slope with the corresponding flux-to-flux coefficient.

corresponds to a resistance of 0.14 Ω. As they are connected to the input coil of the detector SQUID, we have to take the mutual inductance $M_{\mathrm{is,DS}}$ into account, which is given by $(M_{\mathrm{is,DS}})^{-1} = 2.1\,\mu\mathrm{A}/\Phi_0$. Assumming a RRR of 20, wich was measured for these wires, we obtain a bond wire noise contribution of $87\,\mu\Phi_0/\sqrt{\mathrm{Hz}}$. This contribution is orders of magnitude larger than all the other contributions discussed above. Therefore the apparent detector SQUID noise is mainly determined by the current noise of the aluminum bond wires. Using this value we can calculate the cut-off frequency of the low pass characteristic of the noise, that is determined by the resistance of the bond wires and an inductance consisting of bond wire inductance, meander inductance and inductance of the input coil of the detector SQUID. The calculated cut-off frequency is 25 kHz.

Both calculated values, i.e. the bond wire noise contribution and the cut-off frequency, are within the same order of magnitude as the measured values. The deviation depends on the actual shape of the bond wires.

At lower temperatures the contribution of the bond wires becomes negligible, as aluminum becomes superconducting below 1.2 K. Other noise contributions become dominating. This case will be discussed in the following section.

5.5.2 Detector Noise at Low Temperatures

The following text discusses the noise of the experimental setup at 25 mK. First of all we discuss the noise of the amplifier SQUID in a single-stage configuration and subsequently the measurement of the two-stage setup.

Figure 5.11 (left) shows the result of a measurement that was done with the amplifier SQUID in a single-stage setup at a temperature of $T = 25$ mK. The white noise level is measured to be $0.388\,\mu\Phi_0/\sqrt{\mathrm{Hz}}$. To extract the intrinsic SQUID noise from this value, we have to substract the noise contribution of the FLL-electronics and the current noise generated by the gain resistor R_{g} which is connected to the input coil of the amplifier SQUID. Using the voltage-to-flux transfer coefficient $V_{\Phi,\mathrm{AS}} = 1540\mu\mathrm{V}/\Phi_0$ we obtain a FLL-electronics contribution of $\sqrt{S_{\Phi,\mathrm{el}}} = 0.214\,\mu\Phi_0/\sqrt{\mathrm{Hz}}$. The contribution of the gain resistor is obtained by multiplying its current noise with the mututal inductance $M_{\mathrm{is,AS}}$ of the amplifier SQUID. The result is $0.13\,\mu\Phi_0/\sqrt{\mathrm{Hz}}$. Incoherent substraction of the noise contribution of the FLL-electronics and the gain resistor from the measured noise, we obtain an intrinsic amplifier SQUID noise of $\sqrt{S_{\Phi,\mathrm{AS}}} = 0.297\,\mu\Phi_0/\sqrt{\mathrm{Hz}}$. We compare this value with the intrinsic amplifier SQUID noise at 4.2 K by scaling down this value to lower temperatures. Equation (3.1) states that the current noise of the shunt resistors decreases with $\sqrt{T}$. For a constantly biased SQUID one can assume that the temperature of the shunt resistors has a value of about 300 mK because of the poor electron-phonon coupling at low temperatures. Therefore we obtain a calculated intrinsic amplifier SQUID noise of $\sqrt{0.3/4.2} \times 0.6\,\mu\Phi_0/\sqrt{\mathrm{Hz}} = 0.16\,\mu\Phi_0/\sqrt{\mathrm{Hz}}$. This value is a factor of 1.9 smaller than the one we extracted from the measurement.

Figure 5.11 (right) shows the apparent magnetic flux noise in the detector SQUID measured in a two-stage configuration at 25 mK. At frequencies above 10 kHz one

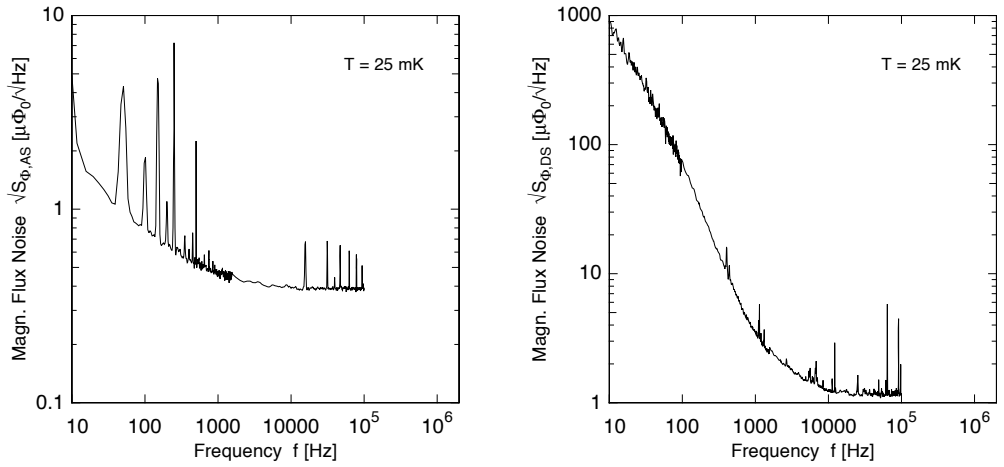

Figure 5.11 **Left:** This figure shows the noise spectrum result of the utilized amplifier SQUID in a single-stage setup at a temperature of $T = 25\,\mathrm{mK}$. The white noise level is measured to be $0.388\,\mu\Phi_0/\sqrt{\mathrm{Hz}}$. **Right:** Two-stage configuration at $T = 25\,\mathrm{mK}$. The plateau at frequencies above 10 kHz has a value of $1.17\,\mu\Phi_0/\sqrt{\mathrm{Hz}}$.

recognizes a plateau of the value $1.17\,\mu\Phi_0/\sqrt{\mathrm{Hz}}$. At frequencies below 10 kHz the measured flux noise increases towards low frequencies proportional to the inverse of the frequency, $1/f$. This is due to temperature fluctuations in the sensor and absorber which stem from the incident particles. We use the results of the measured amplifier SQUID noise to calculate its contribution to the apparent detector SQUID noise. Using the flux-to-flux conversion factor of $G_\Phi = 0.6$ we obtain a contribution of $0.65\,\mu\Phi_0/\sqrt{\mathrm{Hz}}$ for the white noise level.

The magnetic Johnson noise of sensor and absorber is calculated as pointed out in the discussion at 4.2 K and we obtain a sensor noise of $0.07\,\mu\Phi_0/\sqrt{\mathrm{Hz}}$ and an absorber noise of $0.34\,\mu\Phi_0/\sqrt{\mathrm{Hz}}$. The noise of the experimental brass holder is even smaller than in the discussion at 4.2 K and therefore, again, negligible.

The contribution of the thermodynamical energy fluctuations $S_{\mathrm{E_Z}}(f)$ can be estimated by using equation (2.23). However, since the signal rise times are in the order of $\tau_0 \approx 0.5\,\mathrm{ms}$, these energy fluctuations are negligible at frequencies $f > 1\,\mathrm{kHz}$.

To calculate the intrinsic SQUID noise, we scale down the value given in the noise discussion at 4.2 K down to an assumed shunt resistors temperature of 300 mK by using equation (3.1). Thus we obtain an intrinsic detector SQUID noise of $\sqrt{S_{\Phi,\mathrm{DS}}} = 0.36\,\mu\Phi_0/\sqrt{\mathrm{Hz}}$. For comparison we calculate the intrinsic SQUID noise from the high frequency noise level in figure 5.11 (right). For this we incoherently substract the noise contributions calculated above from the measured value of $1.17\,\mu\Phi_0/\sqrt{\mathrm{Hz}}$. The result is an intrinsic SQUID noise of $0.92\,\mu\Phi_0/\sqrt{\mathrm{Hz}}$. This value is 2.6 times larger than expected. A deviation of this size was already observed in earlier experiments [POR07], [KEM07] with different SQUIDs. Up to now this phenomenum is not understood. A possible explanation could be found in intrinsic resonances at the Josephson frequency and higher harmonics of it.

6. Summary and Outlook

In the present work the development of a metallic magnetic microcalorimeter for the high resolution β-spectroscopy is discussed. MMCs are well suited for this purpose as they show an energy independent detection efficiency, a linear detector response and a high energy resolution. The performance of the developed detector was tested with the β-emitter ^{63}Ni that exhibits a 100 % allowed β-decay with an endpoint energy of 67 keV. This β-isotope has a theoretically well understood spectral shape which allows for the convenient evaluation of measurements.

The detector consists of a superconducting meander shaped pick-up coil with a paramagnetic sensor on top that is in good thermal contact to a gold absorber. The sensor material is an alloy of gold and a concentration of 775 ppm of the rare earth metal erbium. A persistent current inside the pick-up coil generates a magnetic field which magnetizes the sensor. An incident particle deposites its energy into the absorber and heats up the sensor which results in a magnetization change which causes shielding currents inside the pick-up coil due to flux conservation. These additional currents convert into a magnetic flux change via an input coil of the first stage of a two-stage SQUID setup that amplifies this signal and converts it into a voltage change via FLL-electronics. Parameters like the geometry of the meander shaped pick-up coil or the thickness of the sensor were optimized for a high signal-to-noise ratio.

A major improvement to former MMCs is that much higher persistent currents can be injected into the pick-up coil, and therefore higher magnetic fields are available, which improves the sensitivity of the detector up to a certain, optimal point. Maximum current densities of $9.3 \times 10^{10}\,\mathrm{A/m^2}$ were achieved.

A good thermal contact between sensor and absorber is important to convert the temperature change of the absorber into a magnetization change of the sensor within a short time. In this work the electroplating of gold absorbers for MMCs was developed which offers the possibility of depositing high purity gold with a large rate. A high RRR, which is important for a fast thermalization, and a big thickness, compared to other microfabrication techniques like sputtering or electron beam evaporation, can be achieved. The electroplating of gold absorbers involved the usage of the negative photoresist SU-8 which is adequate for the production of thick films. Even though this photoresist has the desired properties, its removal after the electroplating is still a problem. Recent investigations have shown that plasma etching shows the most promising results.

A series of electroplating tests with the utilized sulfite-based electrolyte were maintained. The usage of different electroplating currents or different kinds of seed layers did not cause different RRR values. The application of a pulsed current shows a more promising result because of its higher RRR and should be investigated in the future.

In order to obtain a high quantum efficiency for the spectroscopy of β-emitters

with an endpoint energy up to 1 MeV a 4π-absorber was used. With the help of Monte Carlo simulations, a quantum efficiency of 85 % was calculated for the absorber described in this thesis. In the case of ^{63}Ni, a quantum efficiency of 99.996 % was found. The enclosing of a source into a 4π-absorber, by the means of electroplating, was developed. After electroplating the first half, the source is deposited in a liquid form which leaves active $NiCl_2$-crystals after evaporation. By the help of a metal shadow mask the crystals are covered with a thin sputtered film and subsequently the second half is electroplated.

Due to the SU-8 removal problems, the ^{63}Ni-source was encased into an alternatively fabricated 4π-absorber. It was deposited between two gold disks which were diffusion-welded and glued to the sensor. The resulting $NiCl_2$-crystals were estimated to have a total activity of 25 Bq.

Within the experiments several persistent currents were injected into the pick-up coil. The persistent current values were verified by magnetization measurements and the comparison to theoretical curves which were calculated by assuming an interaction parameter of $\alpha = 3$ between the RKKY-interaction and the dipole-dipole-interaction. The measured curves are consistent with the theoretical ones at temperatures above 60 mK. Below, they have a bigger slope which might be due to morphological defects in the sputtered sensor.

For the energy calibration of the detector the 122 keV-line of an external ^{57}Co-source was used. The measured spectra show two different pulse shapes. One type has a rather slow rise and decay time and the other one a fast rise and two decay times. The data analysis showed that the fast pulses are associated with sensor hits.

The measured β-spectrum of ^{63}Ni shows the general shape of the theoretical curve in the energy range between 20 keV and the endpoint energy. Below 20 keV down to the threshold energy of 1.5 keV the intensity is higher than expected with a maximum deviation of 20 %. The enhancement of the spectrum in this range can be motivated by the so-called exchange effect, but quantitative agreement cannot be found. The dominating effect is the large number of pileup events which accompany the rather high source activity which distorts the spectrum in particular at low energies. In order to evaluate measurements more properly, the source activity as well as the signal decay time should be decreased in future experiments.

The Kurie plot of the spectrum shows an endpoint energy of (67.0 ± 1.2) keV which is consistent with the endpoint energy of (66.946 ± 0.020) keV that was determined in [HET87]. Fitting a gaussian to the baseline of the discussed spectrum, we deduced an energy resolution of $\Delta E = 1.2$ keV.

Future MMCs with electroplated absorbers will have short rise times because of the tight contact between sensor and absorber, and short decay times because of good couplings to the thermal bath. Therefore it will be possible to measure β-sources with higher activities and better statistics in a shorter time. The enhanced electroplating technique as a standard process for the absorber fabrication will enable every day β-spectrum measurements by using metallic magnetic calorimeters with an energy resolution, energy independent detection efficiency and linearity which is far from today's possibilities.

Bibliography

[ANG98] L. C. Angrave, N. E. Booth, R. J. Gaitskell, G. L. Salmon, M. R. Harston, Measurement of the Atomic Exchange Effect in Nuclear β Decay, Phys. Rev. Lett. 80, 1610 - 1613, 1998

[ARA66] S. Arajs und G.R. Dunmyre, A search for low-temperature anomalies in the electrical resistivity of dilute gold-erbium alloys, J. Less Com. Met., 10, 220, 1966

[ASH07] Neil W. Ashcroft, N. David Mermin, Festkörperphysik, 3. Auflage, Oldenbourg Wissenschaftsverlag, 2007

[BAN93] S. R. Bandler et al., Metallic Magnetic Bolometers for Particle Detection, J. Low Temp. Phys., 93(3/4), 709-714, 1993

[BER04] Cyanidfreie galvanische Goldelektrolyte, S. Berger, Jahrbuch Oberflächentechnik 2004

[BEH69] H. Behrens and J. Jänecke, Numerical Tables for Beta-Decay and Electron Capture, Landolt-Börnstein: Numerical Data and Functional Relationships in Science and Technology, New Series, Vol. 4, Group I, edited by H. Schopper, Springer, New York, 1969

[BÜH63] W. Bühring, Beta decay theory using exact electron radial wave functions, Nucl. Phys., 40, 472-488, 1963

[BUR04] A. Burck, Entwicklung großflächiger magnetischer Kalorimeter zur energieaufgelösten Detektion von Röntgenquanten und hochenergetischen Teilchen, Diplomarbeit, Kirchhoff-Institut für Physik, Universität Heidelberg, 2004

[BYA56] W. J. Byatt, Analytical Representation of Hartree Potentials and Electron Scattering, Phys. Rev. 104, 1298 - 1300, 1956

[CAS98] P. Cassette, Comparison of activity measurement of ^{63}Ni and ^{55}Fe in the framework of the EUROMET 297 project. Appl. Radiat. Isot. 49 9-11, p. 1403, 1998

[CLA96] J. Clarke in H. Weinstock (ed.), SQUID sensors: Fundamentals, Fabrication and Applications, 1-62, Kluwer Academic Publishers, the Netherlands, 1996

[COL96] R. Collé, B.E. Zimmerman, 63Ni Half-Life: a New Experimental Determination and Critical Review, Applied Radiation and Isotopes, Volume 47, Number 7, July 1996 , pp. 677-691(15), Elsevier

[DAM07] N. Dambrowsky, J. Schulz, Goldgalvanik in der Mikrosystemtechnik Herausforderungen durch neue Anwendungen, Institut für Mikrostrukturtechnik, April 2007

[DAV73] D. Davidov, C. Rettori, A. Dixon, K. Baberschke, E. P. Chock, R. Orbach, Crystalline-Field Effects in the Electron-Spin Resonance of Rare Earths in the Noble Metals, Phys. Rev. B 8, 3563 - 3568, 1973

[DRU04] D. Drung und M. Mück, SQUID Electronics, in J. Clarke und A. I. Braginski (Ed.), The SQUID Handbook: Vol I Fundamentals and Technology, WILEY-VCH, 2004

[ENS00] C. Enss, A. Fleischmann, K. Horst, J. Schönefeld, J. Sollner, J.S. Adams, Y.H. Huang, Y.H. Kim und G.M. Seidel, Metallic Magnetic Calorimeters for Particle Detection, J. Low Temp. Phys., 121(3/4), 137-176, 2000

[ENS05] Christian Enss, Siegfried Hunklinger: Low temperature physics, Springer-Verlag 2005

[FEE50] Eugene Feenberg, George Trigg, The Interpretation of Comparative Half-Lives in the Fermi Theory of Beta-Decay, Rev. Mod. Phys. 22, 399 - 406, 1950

[FLE98] Andreas Fleischmann, Hochauflösendes magnetisches Kalorimeter zur Detektion von einzelnen Röntgenquanten, Diplomarbeit, Kirchhoff-Institut für Physik, Universität Heidelberg, 1998

[FLE03] Andreas Fleischmann, Magnetische Mikrokalorimeter: Hochauflösende Röntgenspektroskopie mit energiedispersiven Detektoren, Dissertation, Kirchhoff- Institut für Physik, Universität Heidelberg, 2003

[FLE05] A. Fleischmann, C. Enss und G. Seidel in C. Enss (Ed.), Cryogenic Particle Detection, Topics Appl. Phys., 99, 151-216, Springer-Verlag Berlin Heidelberg, 2005

[GAI96] R.J. Gaitskell, L. C. Angrave, N. E. Booth, A. D. Hahn, G. L. Salmon, A. M. Swift, A measurement of the beta spectrum of 63Ni using a new type of calorimetric cryogenic detector, Nuclear Instruments and Methods in Physics Research Section A, V. 370, p. 250-252, 1996

[GOR01] Tobias Görlach, Untersuchung paramagnetischer Legierungen für magnetische Tieftemperatur-Kalorimeter, Diplomarbeit, Kirchhoff-Institut für Physik, Universität Heidelberg, 2001

[HAH92] W. Hahn, M. Loewenhaupt, B. Frick, Crystal field excitations in dilute rare earth noble metal alloys, Physica B, 180 & 181, 176-178, 1992

[HAR68] J. T. Harding, J. E. Zimmerman, Quantum interference magnetometry and thermal noise from a conducting environment, Phys. Lett. A 27, 670, 1968

[HAR92] M. R. Harston, N. C. Pyper, Exchange effects in β decays of many-electron atoms, Phys. Rev. A 45, 6282 - 6295, 1992

[HET87] D. W. Hetherington, R. L. Graham, M. A. Lone, J. S. Geiger, and and G. E. Lee-Whiting, Upper limits on the mixing of heavy neutrinos in the beta decay of ^{63}Ni, Atomic Energy of Canada Limited Research Company, Chalk River Nuclear Laboratories, Chalk River, Ontario, Canada K0J 1J0, Phys. Rev. C, 1987

[JEN00] Carsten Jensen, Controversy and Consensus: Nuclear Beta Decay 1911-1934, Birkhäuser Verlag

[KAS56] T. Kasuya, A Theory of Metallic Ferro- and Antiferromagnetism on Zener's Model, Progr. Theor. Phys., 16(1), 45, 1956

[KEM07] Sebastian Kempf, Entwicklung eines vollständig mikrostrukturierten metallisch magnetischen Kalorimeters, Diplomarbeit, Kirchhoff- Institut für Physik, Universität Heidelberg, 2007

[WHI05] KIC LAYOUT EDITOR, version kic-2.4a, free public domain software, distributed by Whiteley Research Inc., www.wrcad.com

[KIL05] High-density arrays of x-ray microcalorimeters for Constellation-X, Kilbourne, C. A.; Bandler, S. R.; Chervenak, J. A.; Figueroa-Feliciano, E.; Finkbeiner, F. M.; Iyomoto, N.; Kelley, R. L.; Porter, F. S.; Saab, T.; Sadleir, J., American Astronomical Society Meeting 207, # 12.07; Bulletin of the American Astronomical Society, Vol. 37, p.1171, 2005

[KIT99] C. Kittel, Einführung in die Festkörperphysik, 12.Auflage, R. Oldenbourg Verlag, München, 1996

[KRA87] Kenneth S. Krane, Introductory Nuclear Physics, John Wiley & Sons, 1987

[KUR36] Franz N. D. Kurie, J. R. Richardson, and H. C. Paxton, The Radiations Emitted from Artificially Produced Radioactive Substances. I. The Upper Limits and Shapes of the β-Ray Spectra from Several Elements, Radiation Laboratory, Department of Physics, University of California, 1936

[LBN02] LBNL Isotopes Project Nuclear Data Dissemination Home Page. Retrieved March 11, 2002, from http://ie.lbl.gov/toi.html.

[LIN07] Markus Linck, Entwicklung eines metalischen magnetischen Kalorimeters für die hochauflösende Röntgenspektroskopie, Dissertation, Kirchhoff-Institut für Physik, Universität Heidelberg, 2007

[LOW93] M. M. Lowry, D. Deptuck, I. C. Girit, Beta spectrum studies with cryogenic micro-calorimeters, Journal of Low Temperature Physics, vol. 93, 239-244, 1993

[MAD02] Marc J. Madou, Fundamentals of Microfabrication: The Science of Miniaturization, CRC, second edition, 2002

[MAY84] T. Mayer-Kuckuk, Kernphysik, B. G. Teubner, Stuttgart 1984

[MEN01] Wolfgang Menz, Jürgen Mohr, Oliver Paul, Microsystem Technology, Wiley-VCH, 2nd rev. ed., 2001

[NAT08] S. Natarajan, D. A. Chang-Yen, B. K. Gale, Large-area, high-aspect-ratio SU-8 molds for the fabrication of PDMS microfluidic devices, J. Micromech. Microeng. 18 (2008) 045021

[NEA40] G. J. Neary, Proc. Roy. Soc. (London) A175, 71, 1940

[PAB08] Andreas Pabinger, *title unknown*, diploma thesis, Kirchhoff-Institut für Physik, Universität Heidelberg, 2008, to be published

[PIE08] Christian Pies, Entwicklung eines metallischen Mikrokalorimeters für die hochauflösende $\gamma-$ Spektroskopie, Diplomarbeit, Kirchhoff-Institut für Physik, Universität Heidelberg, 2008, to be published

[POB96] F. Pobell, Matter and Methods at Low Temperatures, Springer-Verlag, Heidelberg, 1996

[POR07] J.-P. Porst, Towards MARE: Development of a Metallic Magnetic Calorimeter with Superconducting Rhenium Absorber, diploma thesis, Kirchhoff-Institut für Physik, Universität Heidelberg, 2007

[POR08] J.-P. Porst, private communication, 2008

[POV06] B. Povh, K. Rith, C. Scholz, F Zetsche, Teilchen und Kerne, Springer-Verlag, 7. Aufl., 2006

[REI56] F. Reines and C. L. Cowan, The Neutrino, Nature 178, 446, 1956

[ROT07] H. Rotzinger, Entwicklung magnetischer Kalorimeter für die hochauflösende Spektroskopie des β-Emitters ^{36}Cl, Dissertation, Kirchhoff-Institut für Physik, Universität Heidelberg, 2007

[ROT08] H. Rotzinger, private communication, 2008

[RUD54] M. A. Ruderman, C. Kittel, Indirect Exchange Coupling of Nuclear Magnetic Moments by Conduction Electrons, Phys. Rev., 96(1), 99-102, 1954

[SAL06] Francesc Salvat, José M. Fernández-Varea, Josep Sempau, PENELOPE-2006: A Code System for Monte Carlo Simulation of Electron and Photon Transport Workshop Proceedings Barcelona, Spain 4-7 July 2006, Facultat de Física (ECM), Universitat de Barcelona, Spain

[SCH00] Jan Schoenefeld, Entwicklung eines mikrostrukturierten magnetischen Tieftempertatur-Kalorimeters zum hochauflösenden Nachweis von einzelnen Röntgenquanten, Dissertation, Kirchhoff-Institut für Physik, Universität Heidelberg, 2000

[SJÖ75] M.E. Sjöstrand und G. Seidel, Hyperfine resonance properties of Er3+ in Au, Phys. Rev. B, 11(9), 3292-3297, 1975

[STE98] Philippe di Stefano, Recherche de matière sombre non-baryonique au moyen d'un bolomètre à ionisation dans le cadre de l'expérience EDELWEISS, Université de Paris-Sud, U.F.R. Scientifique d'Orsay, 1998

[STR03] T. Straume, G. Rugel, A. A. Marchetti, W. Rühm, G. Korschinek, J. E. McAninch, K. Carroll, S. Egbert, T. Faestermann, K. Knie, R. Martinelli, A. Wallner, C. Wallner, Measuring fast neutrons in Hiroshima at distances relevant to atomic-bomb survivors, Nature, vol. 424, 539-542, 2003

[TAY95] Barry N. Taylor, Guide for the Use of the International System of Units (SI), NIST Special Publication 811, 1995 Edition, National Institute of Standards and Technology

[TES77] C.D. Tesche und J. Clarke, dc SQUID: Noise and Optimization, J. Low Temp. Phys., 29(3-4), 301, 1977

[VEN85] P. Venkataramaiah, K. Gopala, A. Basavaraju, S. S. Suryanarayana and H. Sanjeeviah, A simple relation for the Fermi function, J. Phys. G: Nucl. Phys. 11 359-364, 1985

[WIL69] G. Williams und L.L. Hirst, Crystal-Field Effects of Solid Solutions of Rare Earths in Noble Metals, Phys. Rev., 185(2), 407-415, 1969

[WNA08] Radioisotopes in Medicine, Nuclear Issues Briefing Paper 55, January 2008, Uranium Information Center Ltd, World Nuclear Association, http://world-nuclear.org/

[YOS57] K. Yosida, Magnetic Properties of Cu-Mn Alloys, Phys. Rev., 106(5), 893-898, 1957

Acknowledgments

Finally I want to thank everybody who supported me in executing this work. My gratitude goes to:

Professor Dr. Christian Enss for accepting me in his group. I am grateful for the versatile work I could do and for the large spectrum of physical aspects that were involved. The great motivation inside the group and the international contacts and collaborations provide an ideal basis to work on.

Andreas Fleischmann for the multiple suggestions and valuable ideas during the whole year of this work. His enthusiasm could always motivate me and the discussions with him lead my thoughts in the right direction.

Loredana Fleischmann for her motivation, her great ideas and suggestions. Her relaxed behavior taught me to work in a more deliberate way. I am thankful for the huge amount of time that Andreas and Loredana Fleischmann dedicated to the completion of my thesis.

Matias Rodrigues for his ideas and suggestions to the data analysis and the Monte Carlo simulation.

Thomas Wolf for the introduction into the clean room work, photo lithography, dc-magnetron sputtering and for the multiple discussions and valuable ideas for the detector design and the electroplating, and for the conversations besides physics.

Sebastian Kempf for the advices in programming, the help with the experiments inside the dilution refrigerator, and for the valuable ideas and discussions throughout the thesis. I am thankful for having profited from his physical intuition. Furthermore, he could always calm me down during busy times and focus my view onto essential problems.

Andreas Burck for his help in the beginning of my thesis, for the common time inside the lab and for giving me technical and physical understanding of the dilution refrigerator.

Hannes Rotzinger for the aid with the mask design software KIC and his fast email replies when I was in trouble, for the calculation of the Fermi function of ^{63}Ni, and finally for the multiple beers in Paris during the LTD and the interesting conversations.

Christian Domesle for his help with the cryostat while listening to finest Modern Talking music.

Richard Weldle for the valuable discussions during writing this thesis and for teaching me the fundamentals of table soccer. Writing our theses at the same time made life less hard.

Christian Pies for being my electroplating and SU-8 fellow sufferer who always had good ideas for solving technical problems.

J.-P. Porst for his support with my SQUID problems and his help with LATEX.

Sönke Schäfer for his help during the measurements inside the pulse tube cooler.

Christian Höhn for being a skillful DJ in the ADR lab while I made collimator holes.

Andreas Reiser for his "radioactive" advices and for still talking to me after a sleepless night caused by my snoring during the annual DPG meeting in Regensburg.

Lena Maerten for the funny time during the cryostat runs.

Andi Pabinger for the common time inside the clean room and for teaching me bavarian insults.

The Dynamics of Complex Systems group, by name Masoomeh Baszrafshan, Gudrun Fickenscher, Angela Halfar, Marius Hempel, Sandra Jenewein, Gernot Kasper, Michel Kinzer, Florian Klotz, Astrid Netsch, Mihai Petrovici, Daniel Rothfuß, Celine Rüdiger and Manfred von Schickfus for the great time we had together, for innumerable coffee and table soccer hours.

Robert Weis for solving my computer problems.

Hildegard Putlitz for administration help and for the nice chats in between.

The machine shop of the institute, especially Siegfried Spiegel and Werner Lamade, for the valuable discussions and for the production of high quality devices.

Ralf Achenbach for the help with the fussy bond machines.

The scientists of the Laboratoire National de Métrologie et d'Essais in Saclay, France: Elvire Leblanc and Martin Loidl for their physical ideas and suggestions, for the introduction to French food and for their hospitality when I was in Saclay. They motivated me a lot by their scientific curiosity.
Thierry Branger for positioning the ^{63}Ni into the gold absorber.
Phillipe Cassette for explaining the liquid scintillation method.

Holger von Both, Susanne Rübel and Diana Tritschler from WIELAND Dental + Technik GmbH & Co. KG for the technical support and for the ideas for the used sulfite-based electrolyte.

Dr.-Ing Christian Koch from MicroChemicals GmbH for his support in finding appropriate photoresists for lithography and microfabrication.

Ortrun und Hartmut Cramer for their corrections of the first versions of this thesis and for polishing my English.

My friends and fellow students Matthias Frank, Friedor Jeske, Maria Martin, Renee Klawitter, Christoph Langer, Peter Vivell, Joelle Buxmann, Wolfgang Kerzendorf, Thomas Lompe, Miriam Plachta and, once more, Christian Domesle for having a great time during all the years of studying.

My parents for their support throughout my studies and their encouragement.

Corinna, for all the help I cannot be grateful enough for and especially for all the support during the last weeks and months in which I was barely at home and, most notably, for her love.